National Institute of Standards and Technology
U.S. Department of Commerce

Material Measurement Laboratory
Applied Chemicals and Materials Division
Fatigue and Fracture Mechanics Group

325 Broadway
Boulder, CO 80305

Phase II - Final Report

Project Title:	Start Fiscal Year: 10/1/2015
	End Fiscal Year: 9/30/2018
	NIST Project Leader: Timothy "Dash" Weeks
Characterization of Modern High-Toughness Steels for Fracture Propagation and Arrest Assessment – Phase II	Contact: 303-497-5302, timdash@nist.gov
	Prepared for: DOT/PHMSA
	Contract: DTPH56-13-X-000013
	DOT/PHMSA Sponsor: James Merritt

Notice

This project was funded by the Department of Transportation, Pipeline and Hazardous Materials Safety Administration under the Pipeline Safety Research and Development Program. The views and conclusions contained in this document are those of the authors and should not be interpreted as representing the official policies, either expressed or implied, of the Pipeline and Hazardous Materials Safety Administration, or the U.S. Government.

This work is the contribution of an agency of the U.S. government, and is not subject to copyright.

Commercial equipment, instruments or materials are identified only to adequately specify certain procedures. In no case does such identification imply a recommendation or endorsement by the National Institute of Standards and Technology, nor does it imply that the products identified are necessarily the best available for the purpose.

Acknowledgement

This report was prepared for the U.S. Department of Transportation, Pipeline and Hazardous Materials Safety Administration (US DOT PHMSA). Many individuals have provided valuable contributions throughout this multi-year effort. The project team is particularly grateful for the guidance and encouragement of Mr. James Merritt of DOT PHMSA. Mr. Merritt served as the technical manager on behalf of US DOT PHMSA.

The insightful and constructive inputs to the project from the Technical Advisory Committee are also gratefully acknowledged.

Notice 1

Acknowledgement 1

1 Introduction 2

1.1 Background 3

1.2 Problem Statement 3

1.3 Research Approach 4

1.4 Gap Analysis 5

2 Project Overview 6

2.1 Major Objectives 6

2.2 Research Phases 6

2.3 Milestones and Deliverables 7

2.4 Research Team 7

2.4.1 Technical Advisory Committee 8

2.4.2 Stakeholder Engagement and Collaboration 8

3 Material Properties 8

3.1 Material Selection and Procurement 9

3.2 Experimental Design 9

3.2.1 As-Received Plate Sectioning 10

3.2.2 Experimental Details 18

3.2.3 Pre-straining Wide-plate Material 21

3.3 Material Testing and Results 30

3.3.1 Physical Metallurgy 31

3.3.2 Mechanical Metallurgy 42

4 Constitutive Material Modelling 80

4.1 Current State of the Art 81

4.2 Gap Analysis 81

4.3 Project Progress 82

5 Structural Modelling 89

5.1 Current State of the Art 90

5.2 Gap Analysis 90

5.3 Project Progress 90

6 Conclusions 90

7 Phase III – Future Work 92

8 Bibliography 93

DRAFT

DRAFT

1 Introduction

The development of high-toughness linepipe materials is reducing the relevance of current material characterization methods and their application to design. Current fracture mechanics models, plastic collapse schemes and test methods are inadequate to determine the crack arresting capacity of a steel alloy/linepipe component undergoing unstable high-rate ductile failure. Furthermore, relatively inexpensive tests that are quick to perform are simply not available to accurately assess the fracture behavior of today's high-strength high-toughness linepipe steels.

NIST proposed to identify the stress/strain/crack velocity conditions for unstable high-rate ductile crack propagation found in a full-scale pipeline burst test and duplicate those conditions in a medium scale test. NIST proposed modeling to validate conditions and assumptions used in reducing the scale of the tests. NIST proposed to develop a medium-scale test which can elucidate material property data necessary to qualify high-strength high-toughness steels based on the correlation to large-scale tests. NIST proposed to parametrically determine the material properties governing fracture propagation or arrest-ability. This will assist researchers to determine a relevant and effective small-scale test (or tests) that provides enough information for material selection, design, reliability, as well as integrity and risk assessment.

This project takes a phased approach with complementary research in successive phases beginning with a road map to systematically fill gaps in knowledge and understanding of the problem of unstable high-rate ductile running failures in pipelines.

This report is structured to highlight the problem statement with respect to current state of the art understanding, define knowledge gaps and present the plan and progress toward meeting the objective. The following sections specifically cover the effort to develop and inform a constitutive material model necessary for the structural model of the medium-scale test. The material testing required to inform the constitutive material model are presented. Conclusions of this phase of the project are also presented in addition to the proposed work in Phase III of the project.

DRAFT

1.1 Background

Unstable high-rate ductile running failure in gas-transmission pipelines has economic, social as well as health and safety impacts that require designers and operators to preclude the event with a high degree of certainty. Here, ductile running failure is the dynamic axial crack propagation along the pipeline pressurized with natural gas or other hazardous fluids whose decompression is time delayed and produces a pressure wave in the fluid that precedes the running failure. The conditions that influence full-scale response are phenomenologically complex. The fuel medium, operating pressure, pipeline design, material selection, installation variables (backfill, supports, etc.) and environment all have an influence on the full-scale response. Intentional design against these events has relied on full-scale demonstration experiments and have been coupled with fundamental and semi-empirical models.

1.2 Problem Statement

The advancement of modern steels and their use in pipeline designs have confounded the available models which is further exacerbated by high-strength high-toughness steels. Early semi-empirical models such as the Battelle Two-Curve Model (BTCM), the Battelle simplified model (calibrated to Grade 448 (API 5L-X65)) and more recent correction factor variants are problematic for high-strength high-toughness steels. These limitations are primarily associated with evaluating fracture resistance by use of the Charpy V-Notch (CVN) test. More recent developments using crack tip opening angle (CTOA) as a measure of propagating fracture resistance have spawned several test designs and geometries. Regardless of how fracture resistance is measured or characterized, it is not uniquely controlling the condition of propagation or arrest of high-strength high-toughness steels, suggesting that other properties contribute to the arrest-ability of modern high-strength high-toughness steels.

Pursuing this logic, it is presumed that all influences other than material properties must be well controlled in the design of a medium-scale experimental program, and that the experimental conditions must mimic the full-scale condition. The ductile running failure is preceded by a process zone whereby the material undergoes plastic deformation. Determining arrest-ability based on as-received properties presents the first-order problem for this project. As-received material has a strain history that is significantly different than that of the material in the plastic process zone, therefore, the crack propagates through material with different mechanical properties. Further, the tensile-traction controlled failure is a function of the tensile properties which are in turn a function of the strain history and stress-state of the material at the point of failure. The second-order problem for the project is to determine what material properties govern the formation (size and shape) of the plastic process zone. Formation of the plastic process zone effectively removes energy from the pressure wave preceding the running

DRAFT

failure. One hypothesis is that the resistance to through-thickness thinning controls the extent of plastic deformation in the process zone. This flow-controlled behavior is a function of the thickness (constraint), microstructure and crystallographic orientation or grain texture gradients in the through-thickness direction.

1.3 Research Approach

Structural integrity is assured by the prevention of unstable crack extension. By way of traditional fracture mechanics, this is achieved through the design of structural components such that the stresses will not exceed the limits of the material, imposed by flaw size and material properties. Unfortunately, material properties such as strength and toughness are typically determined on materials and in environments (temperature, stress and strain rates) that have limited applicability to in-service conditions or imposed mechanics during a failure event. The current approaches to study unstable ductile failure are not similar enough to in-service full-scale events or conditions to provide a reliable and economically feasible means of preventing unstable ductile crack propagation.

The full-scale burst test is arguably the most useful, and in some cases, the essential test to evaluate and manage the resistance to ductile failure propagation in gas pipelines. This test can provide critical data necessary for design validation. However, the variables are great in number and uncertainty is high, making it a problematic test for comprehensive predictive models. Another significant drawback of full-scale testing is the high cost and time required, making the usefulness of the test limited to specific design variables where a large test matrix is prohibitively expensive. Several laboratory-scale tests have been in use for decades to qualify materials, and attempts have been made to correlate full-scale performance with laboratory-scale tests.

The prevailing favorite is the notched bar impact test, the most common being the Charpy V-Notch (CVN) test. This test is useful to determine the ductile-to-brittle transition temperature of the steel and the relative fracture energy differences between brittle fracture and ductile failure. This test is quick and simple and has successfully been applied to a range of steel grades but is less relevant for modern high-strength high-toughness steels. The test is adequate to determine the ductile-to-brittle transition temperature but has difficulty with providing valid results in tough, ductile steel where the absorbed energy is dissipated by mechanisms other than creating new fracture surfaces (*i.e.*, large scale plasticity and friction). High-strength high-toughness steels may additionally require high capacity impact machines. Ongoing research with this test method has produced several correction factors that can be used to predict arrest or propagation in the full-scale condition, but the method remains inadequate to describe and mimic the failure mechanics in the full-scale.

DRAFT

Other methods attempt to determine a fracture parameter that can then be compared to full-scale tests and structural models. While there are several such laboratory-scale tests that can determine a fracture parameter (*e.g.*, crack tip opening displacement (CTOD), crack tip opening angle (CTOA) and *J*-integral) there are experimental variables that limit their application. These experimental variables are generally related to specimen geometry or environment (*e.g.*, constraint, temperature and strain rate).

A novel approach presented herein is to mimic the material conditions of the plastic process zone prior to metallurgical and constitutive evaluation. That is, the strain history is known and accounted for and the appropriate material conditions are then known and considered appropriately in the structural model. The effects of adiabatic heating on the material are only significant in that the steel is well above the ductile-to-brittle transition temperature but will also never be high enough to induce a softening effect. Furthermore, this environmental condition is not mimicked or controlled, and it is assumed that room temperature (~21 °C) testing is adequately far from the transition temperature to assume fully ductile failure.

The critical components of the medium-scale test are that the structural, material and environmental conditions are well known, controlled and are characterized well through measurements.

1.4 Gap Analysis

There are several knowledge gaps apparent when considering a program that can predict propagation or arrest of a ductile running failure. Firstly, to date the mechanical testing used in failure assessment diagrams (FAD) is performed on as-received pipe material. These tests are performed on specimens taken from actual pipes so the change in properties due to pipe forming is accounted for. However, the plastic process zone that precedes a ductile running failure has additional strain history that is not accounted for. So, the first knowledge gap can be known by answering the following question. What are the mechanical properties of the steel in all three principal directions inside the plastic process zone? This can be known by testing material adjacent to the fracture edge of a full-scale burst test that resulted in ductile running failure. One problem with this approach is that the strain history of this post-test material is not the same as the strain history of that material immediately prior to the ductile failure. Another problem with this approach is that the strain history of the surrounding material is not known.

Secondly, the different mechanical tests will interrogate potentially different material and in different constraint conditions that are not adequate surrogates of the full-scale test. Notched bar impact specimens for

example do not encompass the full-thickness average material response. Drop weight tear tests can interrogate full-thickness specimens, but the specimens are typically flattened (introducing strains that are not the same in the full-scale condition of ductile failure). Crack tip constraint and stable ductile failure velocity are also difficult to replicate in laboratory-scale tests.

2 Project Overview

2.1 Major Objectives

The primary objective is to develop a medium-scale test, which can elucidate material property data necessary to qualify high-strength high-toughness materials based on the correlation to large-scale tests. This objective, when successful will allow researchers to parametrically determine the material properties governing fracture propagation or arrest-ability, and subsequently determine a small-scale test or tests that provide enough information for material selection, design, reliability, and integrity and risk assessment. An ideal medium-scale test should ensure that unstable ductile tearing at a constant (equilibrium) crack velocity is achieved during the test.

The next objective is to develop an open source model, based on state-of-the-art finite element methods, to parametrically evaluate the crack propagation characteristics of a linepipe section, and to correlate to the results of full-scale tests (provided by open literature, DOT, and/or industry). The model is anticipated to be capable of discriminating energy absorbed by fracture, which could then be compared to the energy produced in small scale tests to deduce the energy of deformation and/or friction. The model will be validated with full scale test results in existing datasets. Once successfully developed and validated, the model would be made available in the public domain for use by industry, academia, and government agencies.

2.2 Research Phases

This project takes a phased approach with complementary research in successive phases beginning with a road map to systematically fill gaps in knowledge and understanding of the problem of unstable high-rate ductile running failures in pipelines. The second phase will determine the most appropriate and controlled way to simulate the process zone of a high-rate ductile failure. The second phase will conduct metallurgical evaluations on the simulated process zone steel to elucidate structure-property relationships with varying strain history. The second phase will also inform a three-dimensional (3D) transversely isotropic constitutive material model useful in subsequent structural modelling of the medium scale test. The third phase will complete the technical design of a medium-scale high-rate test and conduct the testing to inform and validate the structural model.

DRAFT

2.3 Milestones and Deliverables

The first milestone for this project was to develop a technical advisory committee (TAC) that represents multiple relevant industrial interests and expertise. The deliverable for this milestone was to have a functioning TAC with regular meetings to discuss relevant project issues. With the guidance of the TAC, the next task was to identify the type of data generated (*i.e.*, properties measured) and requirements for specimens, test equipment, fixtures, and instrumentation for all available tests. Each of those parameters was then compared to the conditions realized by in-service pipelines. Literature and industry surveys were conducted to define knowledge gaps and develop a conceptual test design that prioritizes key parameters that best match in-service conditions. The next milestone was the development of the conceptual test design. Here, the parameter priorities and the mechanics of the testing will be used to define test equipment, design fixtures and establish performance requirements. Industrial experts and key members of standards development organizations (SDO) were consulted regarding the conceptual test design, method development and analysis. Working backwards from the conceptual medium-scale test, key knowledge gaps were defined, and a subsequent research plan was developed.

Access to relevant materials was a significant obstacle for the project, and a great deal of time and effort were expended to find and secure the material necessary to perform the tests. In concert with the TAC and other international researchers also working on unstable high-rate ductile failure, the materials obtained included API 5L X80 (spiral pipe skelp) and API 5L X70 (UOE pipe plate).

Phase II represented herein involved developing the methods to appropriately generate the strain history in the material to simulate the process zone associated with a high-rate running failure. That is, relevant as-received steel was well characterized and pre-strained in such a manner to obtain small-scale specimens with varying strain histories. The first milestone associated with this phase included the design and fabrication of a wide-plate specimen used for pre-straining. The second milestone was to pre-strain the relevant wide-plate, design a test matrix and develop the sectioning plan for the wide-plate. The next milestone was to conduct all the metallurgical evaluations and small-scale testing to inform the constitutive material model.

2.4 Research Team

The research project was led by Timothy Weeks, the Pipeline Safety Project Leader in the Fatigue and Fracture Mechanics Group of the Applied Chemicals and Materials Division at the Material Measurement Laboratory of NIST. In addition to leading the project, Mr. Weeks was responsible for mechanical metallurgy and medium-scale test development. Project team members from the same group include Dr. Enrico Lucon who was

DRAFT

responsible for Charpy impact testing, Dr's. Nik Hrabe and May Martin were responsible for physical metallurgy and Mr. Ross Rentz was responsible for specimen preparation, test setups and conducting mechanical tests. Dr. Robert Amaro who was formerly at NIST in the same organization, led an academic research team at the University of Alabama under a grant from NIST to the university. Dr. Amaro was responsible for constitutive model development, data analysis and structural model development.

2.4.1 Technical Advisory Committee

A technical advisory committee (TAC) was formed to assist the development of the work scope, execution of the work plan, and the review of the work outputs. Members of the technical advisory committee are David Johnson of Paragon Industries, Su Xu of CanmetMATERIALS, Brian Leis of BN Leis Consultant, Brian Rothwell on behalf of Pipeline Research Council International, Kip Findley of the Colorado School of Mines, Matthew Merwin of US Steel and David Taylor a technical consultant to TransCanada.

The members of the TAC were carefully selected to represent key interests in the pipeline industry, steel industry, standards development organizations, international collaborators and academia.

2.4.2 Stakeholder Engagement and Collaboration

Participation in key conferences and meetings allowed face to face communication with members of the TAC, other industry and government representatives as well as international collaborators. Initially the goal was to present the project objectives to as many representatives as possible for general awareness and to solicit specific support. The material source needs were presented heavily, since a source was not identified definitively through the TAC.

3 Material Properties

This section defines the material testing to determine mechanical properties of the steel in three principal directions and with increasing pre-strain levels. Procurement of relevant steel plate material was an obstacle to making significant experimental progress. Nonetheless, suitable material was obtained, and the experimental design presented here considered the limited material available. This section also defines the process for generating the simulated process zone by pre-straining a large wide-plate.

3.1 Material Selection and Procurement

In conjunction with the TAC it was decided that API 5L X80 would be targeted as representing a modern high-strength high-toughness grade with significant interest and therefore relevance from the pipeline industry. Based on the conceptual medium-scale test, it was decided that only plate material be sought for the test matrix.

The conceptual medium-scale test design drove the material source needs and it was quickly obvious to the TAC and to the project team that obtaining API 5L X80 plate material would be difficult. One source of X80 steel was found but the source could not provide plate in the size required for the medium-scale test. Instead strips of skelp were delivered to NIST for testing. The material will be useful to inform and validate the material models and structure-property relationships but will not be used to conduct medium-scale tests.

As stated earlier, access to relevant materials was a significant obstacle for the project, and a great deal of time and effort were expended to find and secure the material necessary to perform the tests. In concert with the TAC and other international researchers also working on high-rate ductile failure, the materials obtained included API 5L X80 (spiral pipe skelp) and API 5L X70 (UOE pipe plate). Due to the extensive experimental design presented here, the research focused on the X70 steel only. This steel still represents a high-strength high-toughness steel relevant to the pipeline industry.

For clarification, the steel obtained was flat plate, taken out of production prior to pipe shape forming. It is recognized that as-received properties of plate material will differ slightly from as-received properties of pipe material. This difference is the result of forming and thermo-mechanical processing. Notably, the differences in mechanical properties correlated to the pipe geometry (clock position) and even along the length of a linepipe section (~10 m) are well documented. By testing flat plate, several variables can be better controlled and subsequently the material can be better characterized and documented.

3.2 Experimental Design

This section describes the experimental matrix designed to maximize the use of limited material while also ensuring that key material properties are interrogated. The experiments and processes will specifically determine what influences there are on the material properties respective of strain history, test configuration and scale.

DRAFT

Modelling and validating models for three dimensional transversely isotropic material properties requires that the material properties in the through-thickness direction of the plate be known. Furthermore, it is important that the material properties are also known with increasing levels of strain.

While developing the overall experimental design for the project the following key questions were used to guide experimental design decisions:

- What intrinsic material properties are necessary for modelling?
- What changes in material properties are the most relevant to determine when correlating changes in strain history or environmental conditions?
- What small scale tests are the most valuable or useful to determine the necessary material properties?
- How can through-thickness material properties be measured?
- What alternative specimen geometries or test methods are there?
- Are the alternatives standardized and what is the relationship between alternative test results and the results from standardized tests?
- What strain ranges are the most valuable or useful to characterize the conditions of the process zone leading up to and at the condition of failure.
- What wide-plate specimen geometry will yield enough material to be sectioned into small scale specimens with a nearly uniform strain gradient over the typical length scale (*i.e.*, gage length) useful for small scale testing?
- What chemical or microstructural properties are relevant to the mechanical properties?
- What relationship exists between the microstructural and mechanical properties?
- Do the microstructural properties change with increasing levels of plastic strain?

3.2.1 As-Received Plate Sectioning

This section details the sectioning plan of an as-received plate for the purpose of small-scale testing in all three directions; longitudinal to the long edge of the plate, transverse to the long edge (rolling direction) and the through-thickness direction. Blanks were also cut on the diagonal (45 degrees to the rolling direction). The plate was approximately 32 in (813 mm) by 25 in (635 mm) with a thickness of 0.66 in (16.8 mm). The plate was 25 in (635 mm) in the rolling direction. The sectioning plan is shown in Figure 1. All sectioning was completed by water-jet cutting to eliminate the possibility of material changes associated with high temperatures from other cutting methods.

From the numbered blanks (see Figure 1) the following small-scale specimens were machined:

- round tensile
- mini-tensile (rectangular cross section)
- cylinders
- notched bar impact (Charpy V-Notch).

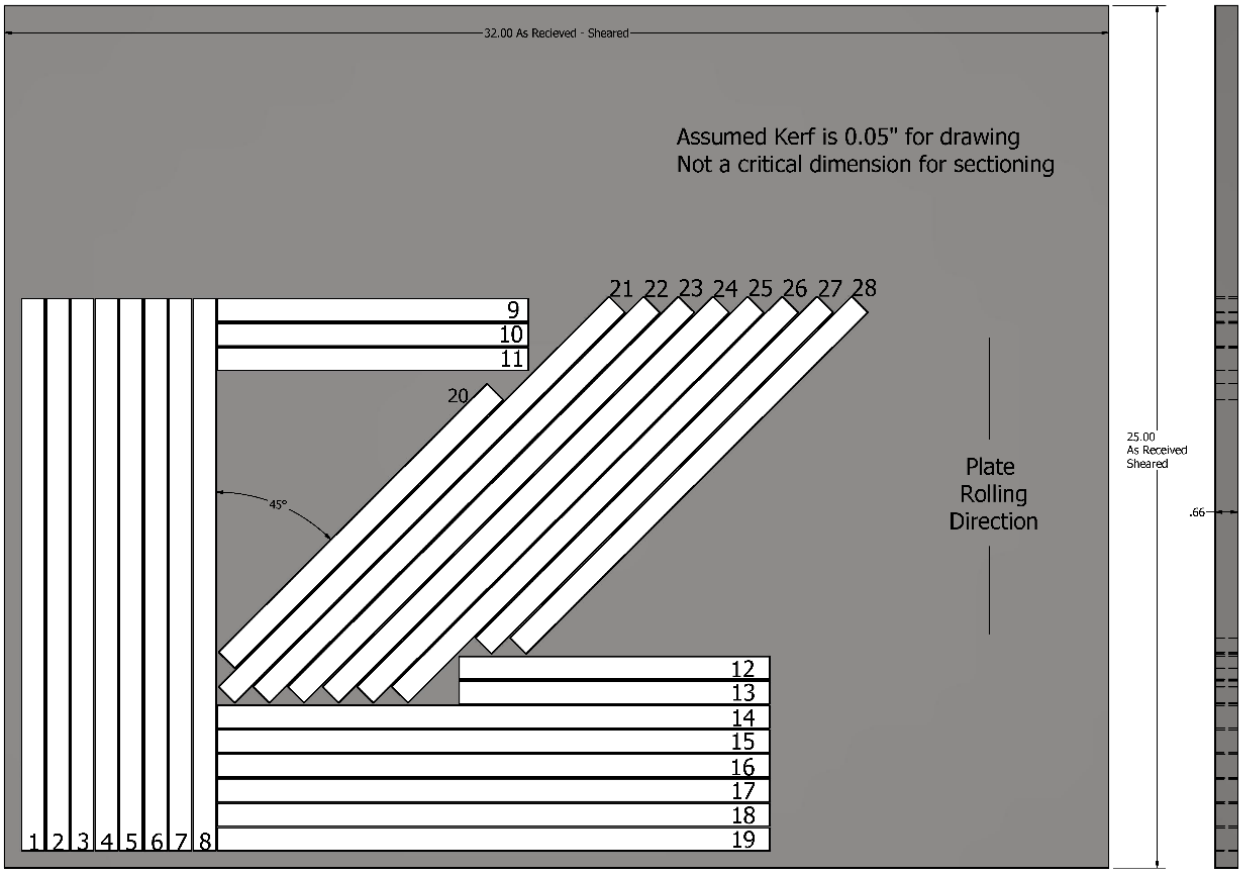

Figure 1. As-received plate sectioning plan for small scale testing.

Round tensile specimens were machined from the as-received numbered blanks according to the proportions defined in the American Society of Testing and Materials' (ASTM) Standard Test Methods for Tension Testing of Metallic Materials (E8/E8M). The machine drawing used to produce the round tensile specimens is shown in Figure 2. An additional round tensile geometry was also used on as-received steel. The alternate geometry shown in Figure 3, was also used for specimens sectioned from pre-strained plate, described in later sections.

Note that English units on machine drawings were used throughout the project simply because English units were used to model the parts and specimens. Unit conversion to System International (SI) units on every drawing

is not suggested for the purposes of manufacturing the same specimens. If specimens with strictly SI units are desired, it is suggested to use the appropriate sizes, proportions and tolerances according to the SI version of the standard where applicable.

Full-thickness flat-strap tensile tests are routine and standard practice. They were considered for this test program; however, the size of the specimens makes them impractical for our comparisons. Using them for as-received material is not a significant issue provided that the material is available. However, to pre-strain bulk material and obtain a consistent pre-strain value (small gradients) throughout the full reduced gauge-section is impractical with the amount of material available to the project.

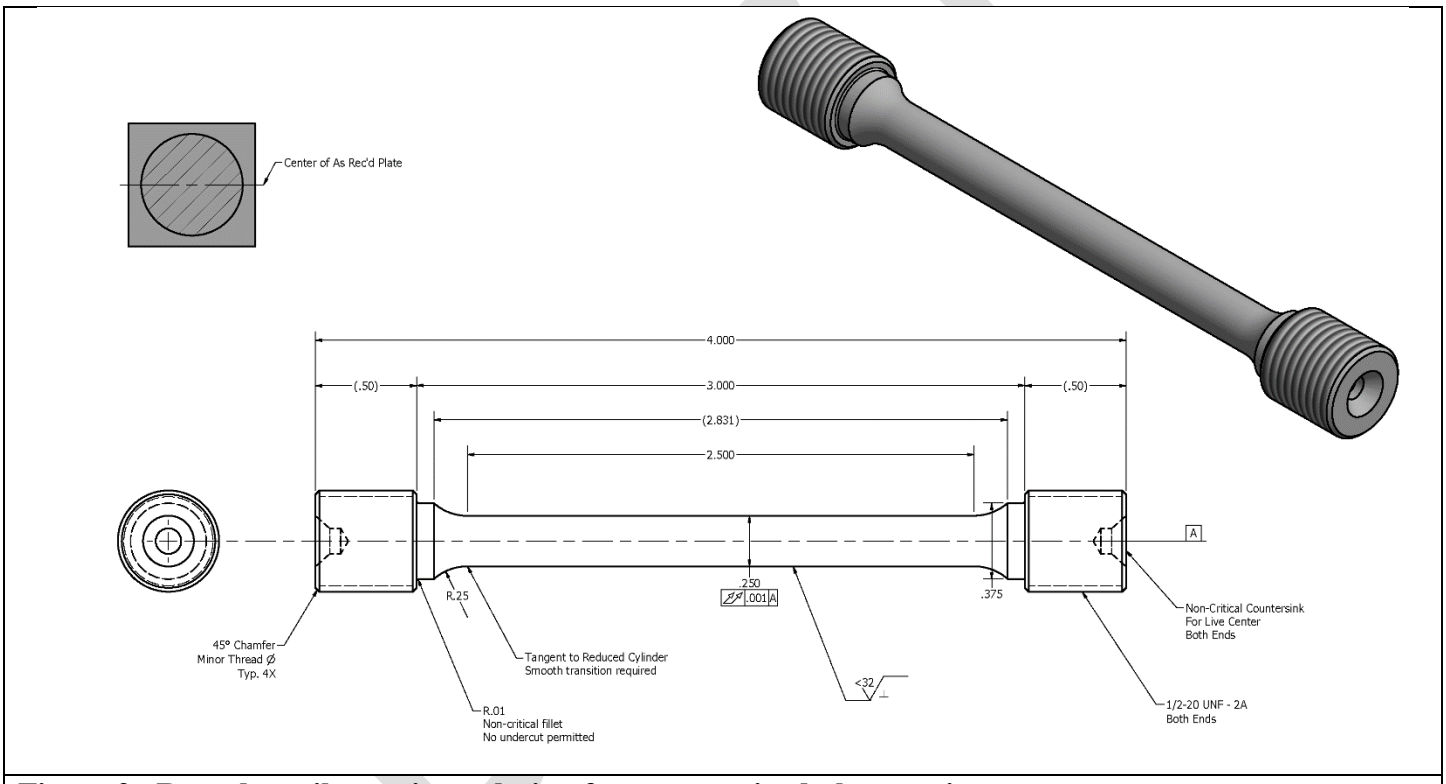

Figure 2. Round tensile specimen design from as-received plate sections.

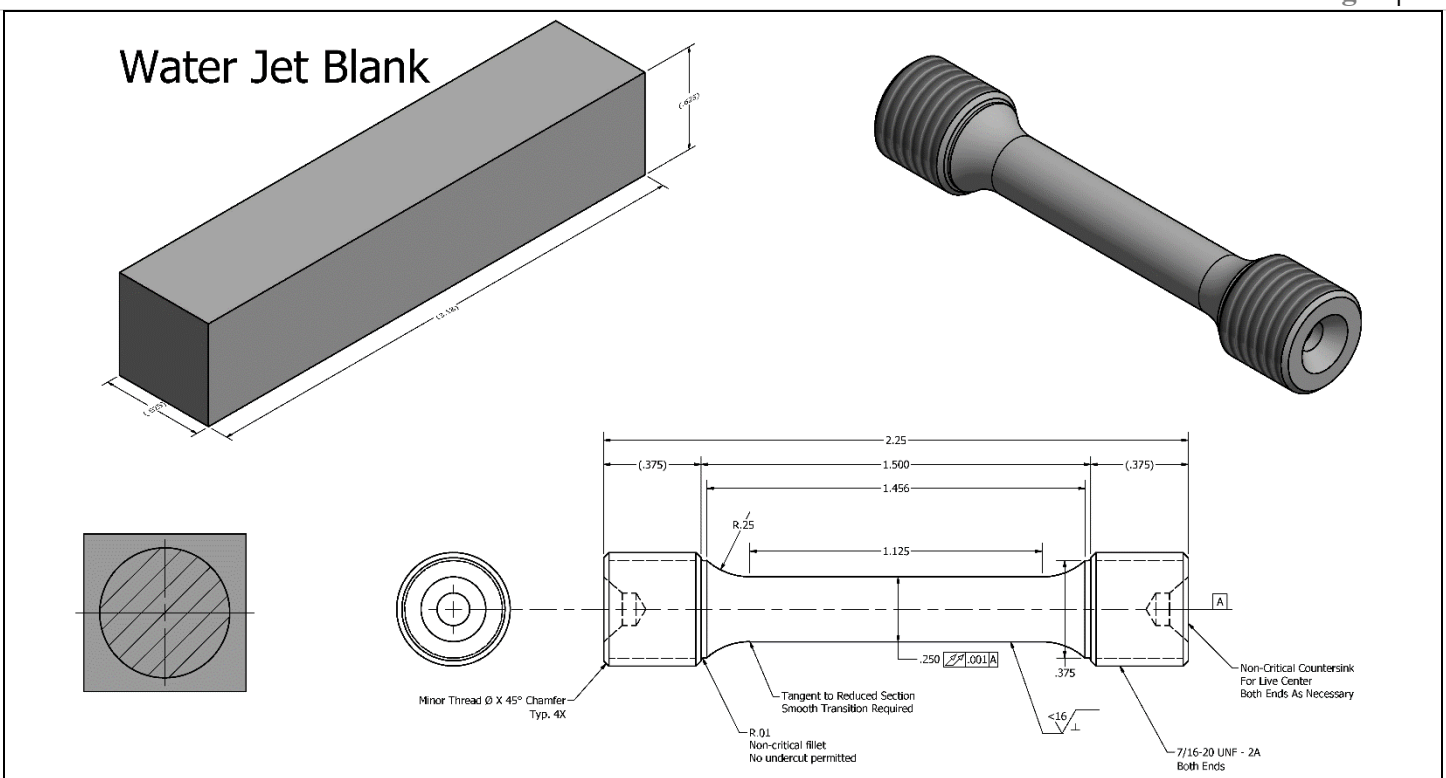

Figure 3. Alternate round tensile specimen design from as-received plate sections. This geometry is also specified for pre-strained round tensile specimens.

In order to determine the through-thickness tensile properties of the steel, several specimen geometries and sectioning plans were considered. The ASTM Standard Specification for Through-Thickness Tension Testing of Steel Plates for Special Applications (A770/A770M) is specifically applied to plate thicknesses greater than 1 in (25.4 mm) however the methodology could be applied to thinner plates. Further, other test methods using friction or fusion welded tabs were also considered and may be revisited in future research. For this phase of the project, the mini-tensile specimen used had a rectangular cross-section and a relatively small gauge-section. It is notable that the reduced gauge-section only allows the center portion of the plate (through the thickness) to be tested. The mini-tensile specimens were machined from the numbered blank using wire electro-discharge machining (EDM). The proportions of reduced gauge-section and gauge-section width matched those found in ASTM E8/E8M. The specimen and stack designs are shown in Figure 4. The grip ends were designed so that the specimens are loaded along the arc of the fillets, as opposed to compression/friction gripping the face of the specimen grip ends. The drawing in Figure 4 specifies a surface grinding operation, however after several development iterations and comparative data analysis, the EDM surface finish was determined to be adequate and did not influence the test results.

The grip design is shown in Figure 5. The grips are pin loaded in a clevis, making specimen installation very quick and simple. The specimen is centered in the grip with spacers on either side of the specimen in each grip. There is light clamping force on the spacers, but these spacers are not meant to transfer axial load to the specimen.

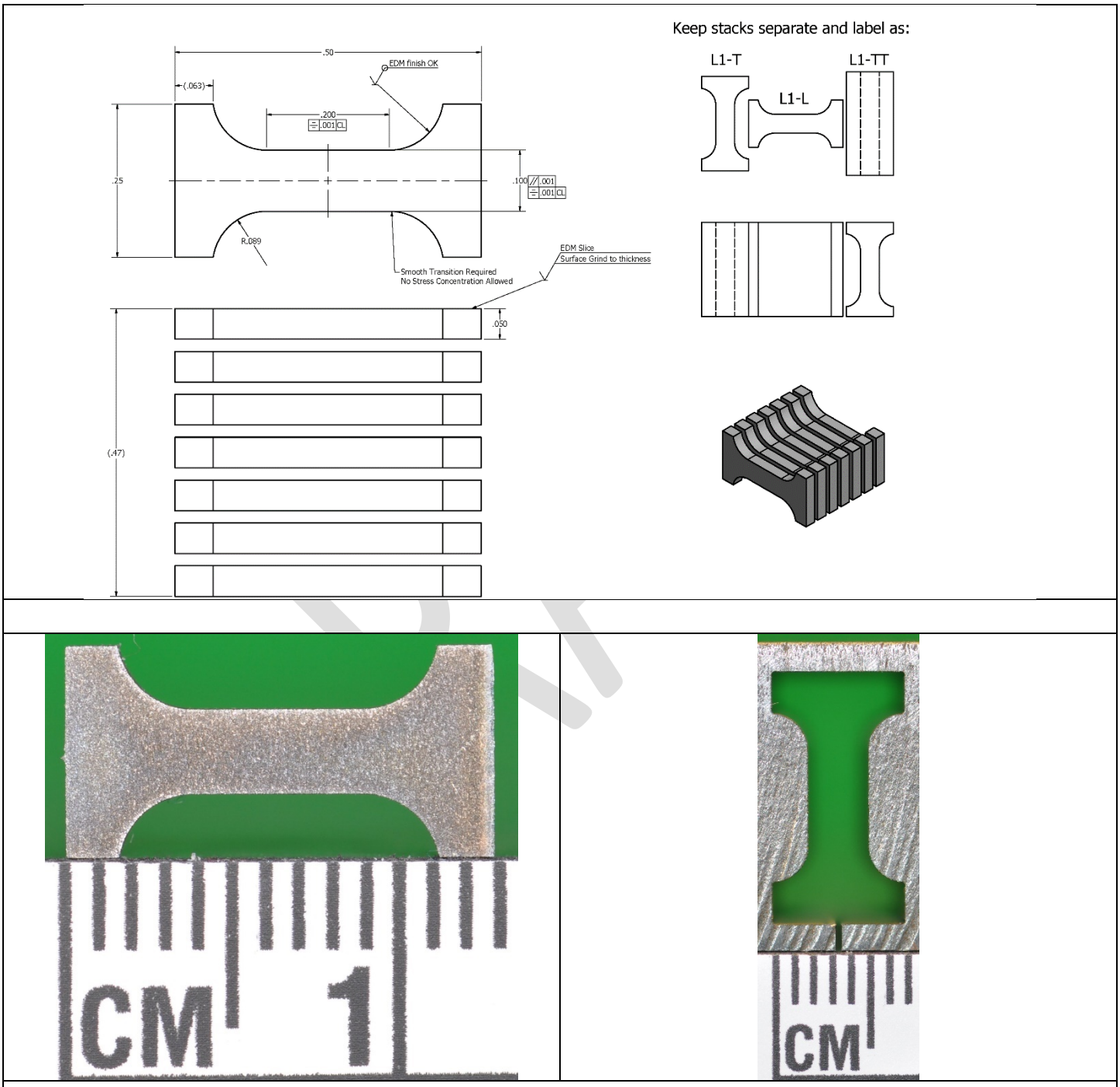

Figure 4. Mini-tensile specimen design (top), a photograph of a specimen showing the surface finish resulting from the EDM process (bottom left), and a photograph of the blank from which the through-thickness stack was taken.

The specimen thickness dimension was determined after several considerations. Firstly, the thickness controlled the maximum stress in the cross-section and that stress must be lower than the stress acting on the grip section to ensure that the grip section didn't deform significantly and therefore successfully transferred the load from the test machine to the specimen gauge-section. Secondly, it is expected that this specimen scale will require multiple specimens to get representative average tensile properties that correlate to a specimen with a larger test volume, respective of material inhomogeneity. Thirdly, volumetric or free surface effects on the stress-strain state during the test are different between the mini-tensile specimen and the standard round tensile specimen, more specimens from a stacked sectioning method may allow for the separation of inhomogeneity and stress-strain state effects on the results. This level of analysis and study are suggested future research areas in combination with potentially using other specimen designs discussed previously.

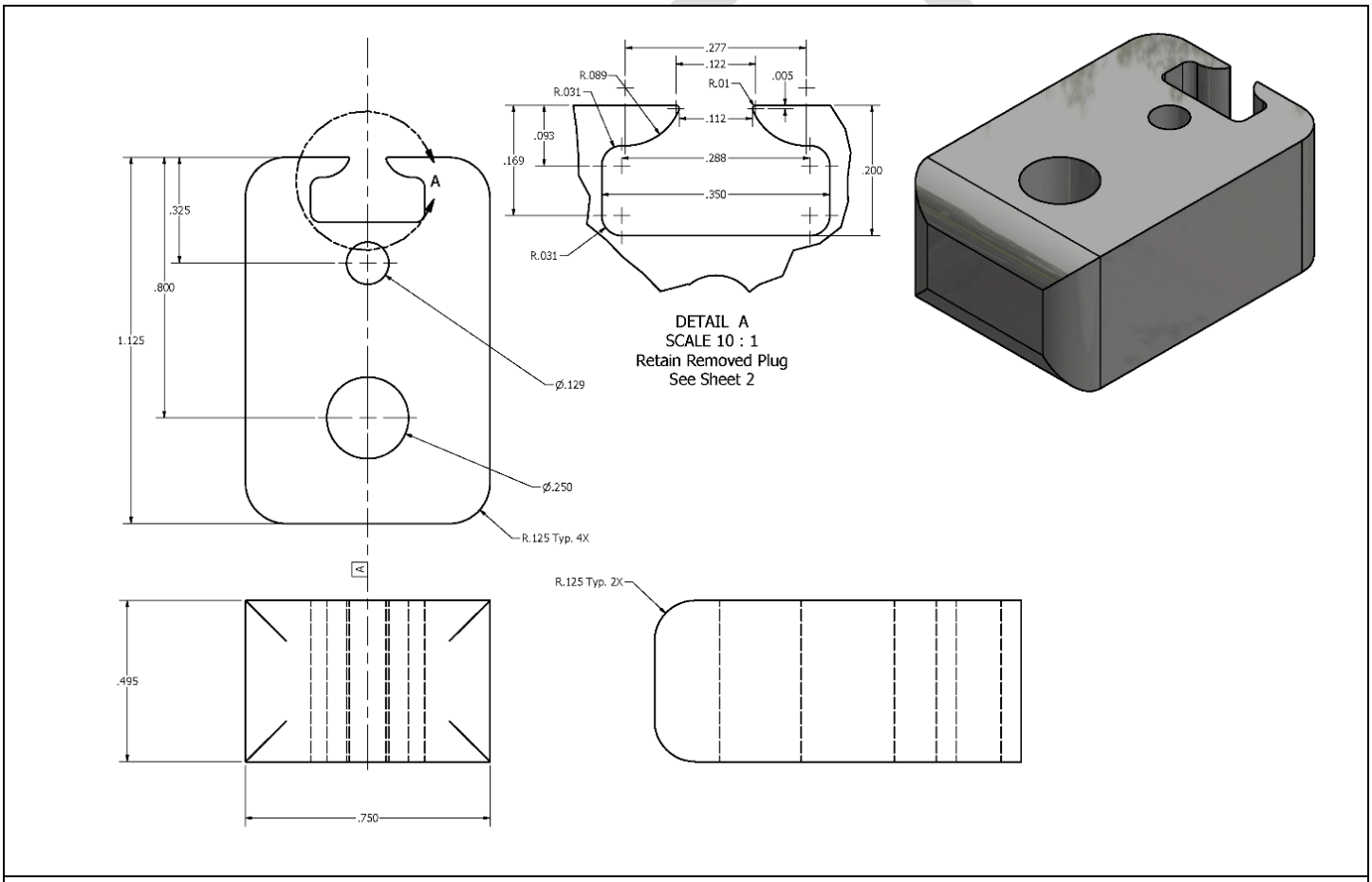

Figure 5. Mini-tensile specimen grip design.

Cylinders were also cut from each of the blanks. These cylinders were not used in this phase of the project and were only sectioned for additional future research. The cylinders were cut and ground to be tested in compression according to ASTM's Standard Test Methods of Compression Testing of Metallic Materials at Room Temperature (E9). Additional cylinders were cut for the purpose of experimenting with alternative through-thickness tensile specimen geometries. Future work using the cylinders will compare tensile properties with compressive properties as well as examining the volumetric effects on the tensile data as discussed earlier. Like the mini-tensile specimens, the cylinders were sectioned in all three orientations. The sectioning plan used to obtain cylinders adjacent to the mini-tensile specimens is shown in Figure 6.

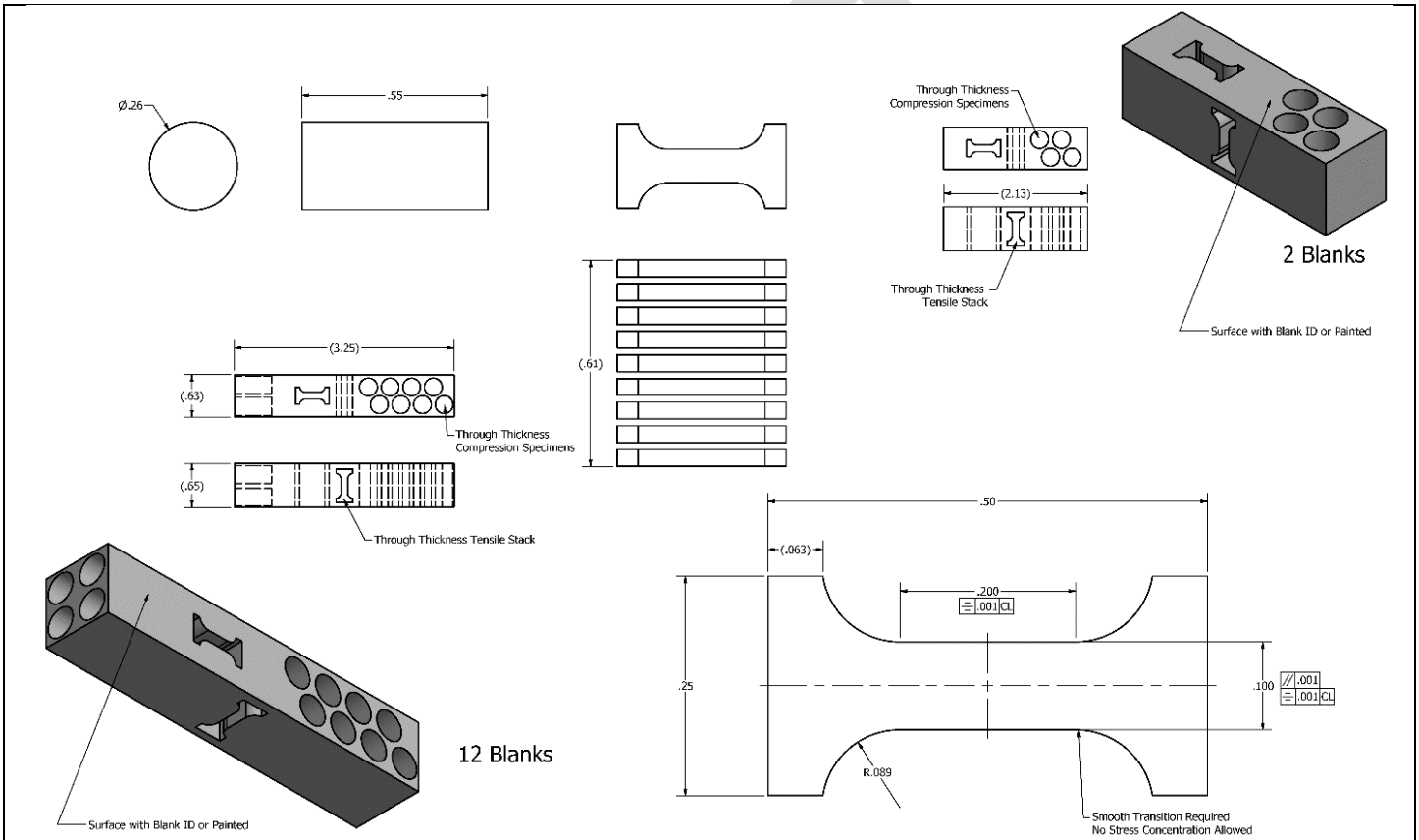

Figure 6. Typical mini-tensile specimen and cylinder sectioning design.

The Charpy V-Notch specimen is the final small-scale test specimen sectioned from as-received material. Specimens were sectioned from numbered blanks to characterize the ductile-to-brittle transition as well as examine the effects of orientation on absorbed energy. The sectioning plan is shown in Figure 7. The specimen design and testing procedure followed were according to ASTM's Standard Test Methods for Notched Bar Impact Testing of Metallic Materials (E23).

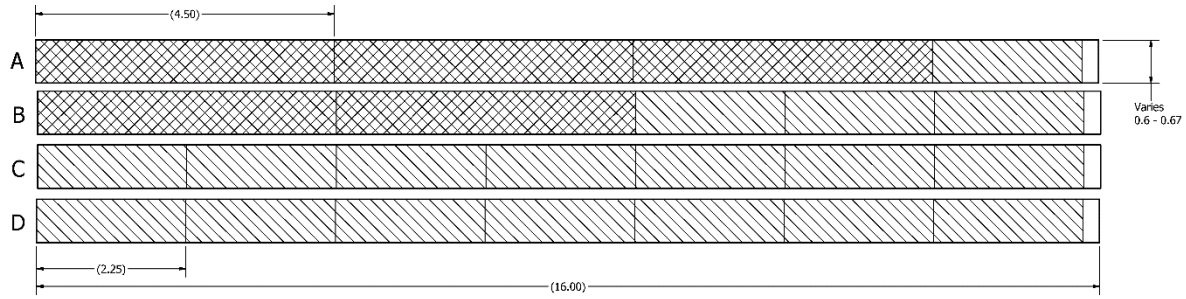

Charpy Specimens				
Material	Blank ID	Qty	Notch Direct	Reference B
X70	X70-3	1	L	A
X70	X70-4	3	L	B
X70	X70-5	7	L	C
X70	X70-6	7	TT	D
X70	X70-7	7	TT	D
X70	X70-15	1	L	A
X70	X70-16	3	L	B
X70	X70-17	7	L	C
X70	X70-26	1	L	A
X70	X70-27	3	L	B
X80	X80-3	1	L	A
X80	X80-4	3	L	B
X80	X80-5	7	L	C
X80	X80-6	7	TT	D
X80	X80-7	7	TT	D
X80	X80-15	1	L	A
X80	X80-16	3	L	B
X80	X80-17	7	L	C
X80	X80-26	1	L	A
X80	X80-27	3	L	B
Total		80		

See Sheet 2 for dimensioning

Tensile Specimens			
Material	Blank ID	Qty	Reference
X70	X70-3	3	A
X70	X70-4	2	B
X70	X70-15	3	A
X70	X70-16	2	B
X70	X70-26	3	A
X70	X70-27	2	B
X80	X80-3	3	A
X80	X80-4	2	B
X80	X80-15	3	A
X80	X80-16	2	B
X80	X80-26	3	A
X80	X80-27	2	B
Total		30	

See Sheet 3 for dimensioning

All Specimens Bagged According to Blank ID - Labeled at NIST

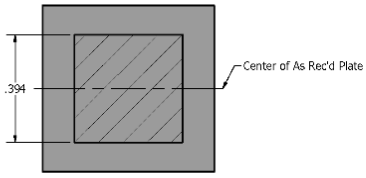

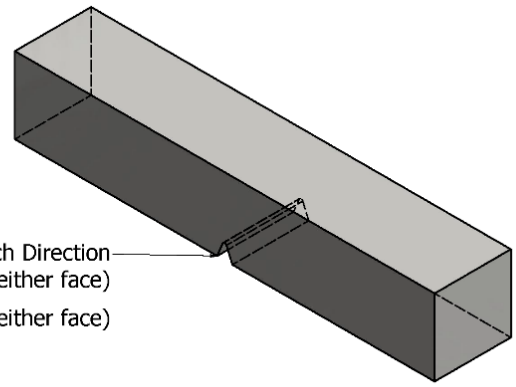

Notched Face Defined by Notch Direction
TT = Through Thickness of As Rec'd Plate (either face)
L = 90˚ to Through Thickness (either face)

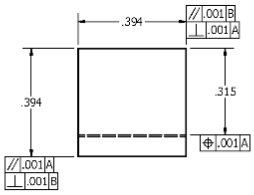

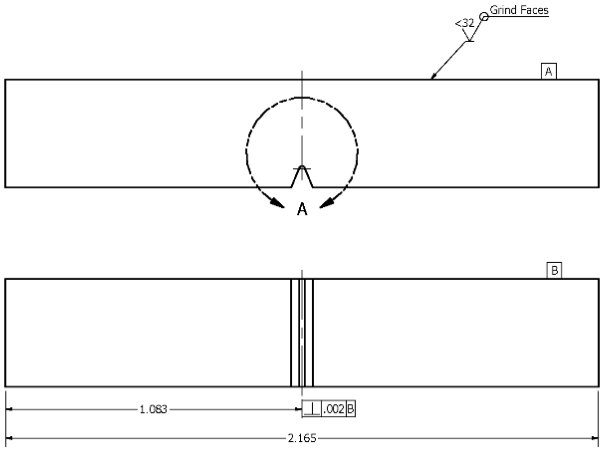

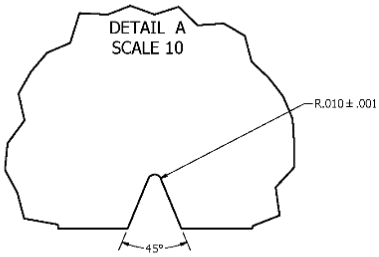

All Specimens Bagged According to Blank ID - Labeled at NIST

Figure 7. Sectioning plan (top) and machine drawings for Charpy V-Notch specimens (bottom).

3.2.2 Experimental Details

3.2.2.1 Procedures and Equipment

Where appropriate all specimen design and testing procedures for small-scale testing followed an ASTM Standard Test Method. All test equipment and measuring instruments were calibrated to a NIST traceable reference and were within allowable uncertainty limits for the instrument considered.

Round tensile tests were performed on a universal servo-hydraulic test machine under displacement control at the rate specified in ASTM E8/E8M for yield point determination. The universal test machine had a maximum force capacity of 100 kN. The threaded specimen adapters were inserted into universal joints on each end of the specimen to ensure axial loading of the gauge-section. The specimens were tested with a clip-on dual-beam extensometer to measure the axial engineering strain on the specimen during the test. The extensometer had a gauge-length of 2.0 in (50.8 mm). The extensometer remained attached to the specimens for the duration of the test up to failure. Several tests were performed on smaller gauge-length specimens, the geometry of the smaller specimens matched that used for pre-strained round tensile tests described later. The extensometer used for these tests had a gauge-length of 1.0 in (25.4 mm).

Mini-tensile tests were performed on a universal servo-hydraulic test machine under displacement control at the rate specified in ASTM E8/E8M for yield point determination. The universal test machine had a maximum force capacity of 5 kN. The specimen grips were pin loaded through clevises and the clevis on the upper end of the specimen was attached to a universal joint. The specimens were tested with a clip-on custom extensometer to measure the axial engineering strain on the specimen during the test. The custom extensometer had a gauge-length of 3 mm (0.12 mm). Non-contact strain measurement techniques were used during the development trials for this specimen geometry and gripping method. The clip-on extensometer was chosen for the strain instrumentation because it was faster and easier to use than the non-contact methods.

Charpy V-Notch tests were performed on a high-capacity impact machine with a potential energy capacity greater than 950 J and impact speed of 5.47 m/s, in accordance with ASTM E23-18. Although most tests were conducted at room temperature (21 °C ± 1 °C), some specimens were tested at low temperature, in the range between -25 °C and -196 °C. For the lowest test temperature (-196 °C), the specimens were immersed in liquid nitrogen. At -125 °C and -100 °C, specimens were soaked in a mixture of liquid nitrogen and ethyl-alcohol. Between -75 °C and -25 °C, a chilled bath of ethyl-alcohol was used. For all low temperature tests, specimens were thermally conditioned for at least 10 minutes before being transferred to the impact position and tested

within 3 seconds. For every test performed the absorbed energy (*KV*) was recorded from the machine encoder and lateral expansion (*LE*) was measured from the broken sample. For the X70-6 sample set, *KV* and *LE* values were fitted as a function of test temperature by means of the commonly used hyperbolic tangent model, yielding the ductile-to-brittle transition temperatures ($DBTT_{KV}$ and $DBTT_{LE}$) and Upper Shelf Energy (*USE*).

3.2.2.2 Test Matrices

The test matrices for the small-scale as-received material tests are presented in this section. It was typical to section and machine more specimens than were tested in this phase. The additional specimens allowed for duplicates in the case of anomalous or erroneous results and alternates in the case of experimenting with different conditions or instrumentation. The specimen identifiers found in each table in this section follow the following formatting, Material – Blank – Number, with occasional orientation labels that precede the specimen number. For example, X70-10-L1 in Table 3 is describing the first mini-tensile specimen tested from blank number 10 which is longitudinally oriented to the long edge of the as-received X70 plate (transverse to the rolling direction).

The as-received round tensile test matrix is found in Table 1. The strain history effects on the small-scale test results are most relevant in the longitudinal direction because pre-straining of the wide-plate, presented in section 3.2.3, occurs in the longitudinal direction of the as-received plate. The longitudinal direction specimens from the as-received material were tested as duplicates from several numbered blanks. These will elucidate potential inhomogeneities that are functionally dependent on the location within the plate. Specimens from blank 18 and 19 are duplicates and alternates.

Generating and subsequently testing material with known strain histories is an important aspect of this work. Two approaches are possible; first, a small-scale specimen can be pre-strained, fully unloaded and then tested to failure, or secondly, specimens can be machined from pre-strained bulk material and tested. To test the first approach several specimens were pre-strained, unloaded and then tested to failure. The design of this small experiment is shown in Table 2. The results from the tests in Table 2 will be compared to the results of bulk pre-strained round tensile specimens.

DRAFT

Table 1. As-received X70 Round Tensile Test Matrix		
Transverse (Aligned with Rolling Direction)	**Longitudinal** (Transverse to Rolling Direction)	**Diagonal to Rolling Direction**
X70-3-1	X70-13-1	X70-26-1
X70-3-2	X70-13-2	X70-26-2
X70-4-1	X70-15-2	X70-27-1
X70-4-2	X70-16-1	X70-27-2
	X70-16-2	
	X70-18-2*	
	X70-18-3	
	X70-18-4	
	X70-19-4	

* Reduced gauge-length round specimen

Table 2. As-received X70 In-Situ Pre-Strained Round Tensile Test Matrix	
Longitudinal	**Pre-Strain Conditions**
X70-18-1*	Loaded and unloaded five times (0.3 %, 0.5 %,0.7 %, 0.9 %, 1.1 %)
X70-19-1*	Loaded to 0.5 % and unloaded
X70-19-2*	Loaded to 2.0 % and unloaded
X70-19-3*	Loaded to 4.0 % and unloaded

* Reduced gauge-length round specimen

Round tensile specimens according to ASTM E8/E8M (Table 1) are the standard to which the mini-tensile test results will be compared. The round tensile specimens provide valuable data in the plane of the plate, that is, the longitudinal and transverse directions. However, the through-thickness direction properties are not available with standard round tensile tests. The mini-tensile specimen becomes valuable for through-thickness properties but the data from the mini-specimen regardless of orientation is geometry dependent.

Table 3. As-received X70 Mini-Tensile Test Matrix		
Longitudinal	**Transverse**	**Through-Thickness Direction**
X70-10-L1	X70-10-T1	X70-10-TT1
X70-10-L2	X70-10-T2	X70-10-TT2
X70-10-L3	X70-10-T3	X70-10-TT3

Charpy V-Notch testing had two objectives; first, determine the ductile-to-brittle transition characteristics of the as-received steel; and second, determine the difference in absorbed energy as a function of the crack path. All v-notch specimens were taken from blanks that are transverse to the rolling direction so that the crack planes

DRAFT

would be normal to the rolling direction. The test matrix for the ductile-to-brittle transition temperature is given in Table 4, and the test matrix to determine orientation effects on absorbed energy is given in Table 5.

Table 4. As-received X70 Charpy V-Notch Test Matrix – Ductile-to-brittle Transition

Specimen ID	Crack Plane (Direction)	Temperature (˚C)
X70-6-TT1	L-TT (TT)	21
X70-6-TT2	L-TT (TT)	-196
X70-6-TT3	L-TT (TT)	-25
X70-6-TT4	L-TT (TT)	-50
X70-6-TT5	L-TT (TT)	-75
X70-6-TT6	L-TT (TT)	-100
X70-6-TT7	L-TT (TT)	-125

Table 5. As-received X70 Charpy V-Notch Test Matrix – Orientation Effects

Specimen ID	Crack Plane (Direction)	Temperature (˚C)
X70-2-L1	L-TT (L)	20
X70-2-L2	L-TT (L)	20
X70-2-L3	L-TT (L)	20
X70-2-L4	L-TT (L)	20
X70-2-L5	L-TT (L)	-86
X70-2-L6	L-TT (L)	-86
X70-2-L7	L-TT (L)	-86
X70-7-TT1	L-TT (TT)	22
X70-7-TT2	L-TT (TT)	22
X70-7-TT3	L-TT (TT)	22
X70-7-TT4	L-TT (TT)	22
X70-7-TT5	L-TT (TT)	-84
X70-7-TT6	L-TT (TT)	-84
X70-7-TT7	L-TT (TT)	-84

3.2.3 Pre-straining Wide-plate Material

Once again, generating and subsequently testing material with known strain histories is an important aspect of this work. This section details the design of the wide-plate used to pre-strain the steel for the purpose of sectioning small-scale specimens from it. Several design considerations drove the final wide-plate geometry. The available material and the force capacity of the machine used to pre-strain the plate were the primary considerations.

DRAFT

3.2.3.1 Wide-plate Specimen Design

The wide-plate specimen was sectioned from as-received plate using a water jet process. Additional small-scale material blanks were also cut from the plate for future work. The sectioning diagram is shown in Figure 8. The details of the wide-plate geometry are given in the machine drawing found in Figure 9. Finally, the specimen was welded to high strength low alloy (HSLA) steel grip ends. The steel selected was HSLA 100 to ensure adequate strength and weldability. The grip ends and welding details are given in Figure 10.

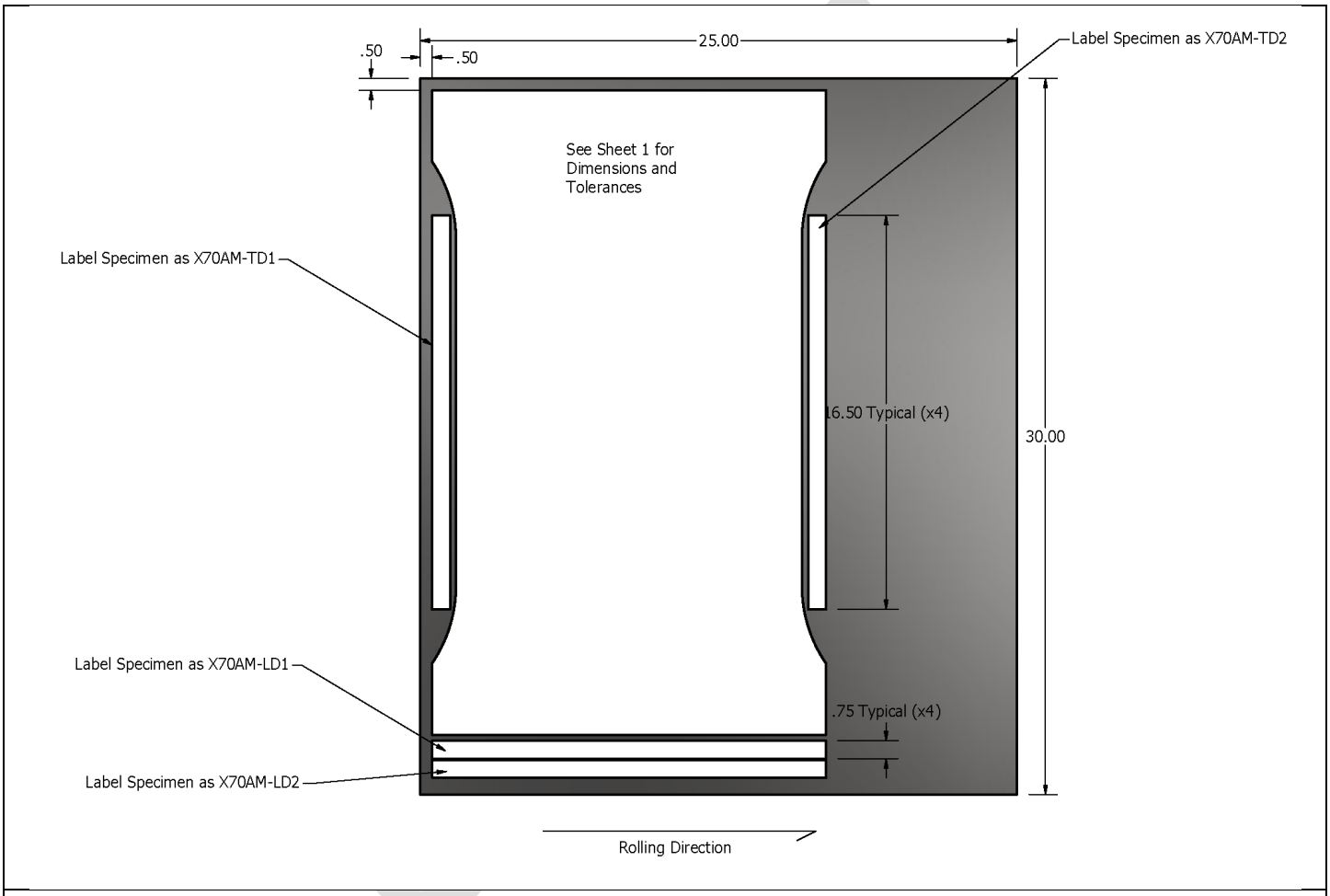

Figure 8. Wide-plate sectioning diagram.

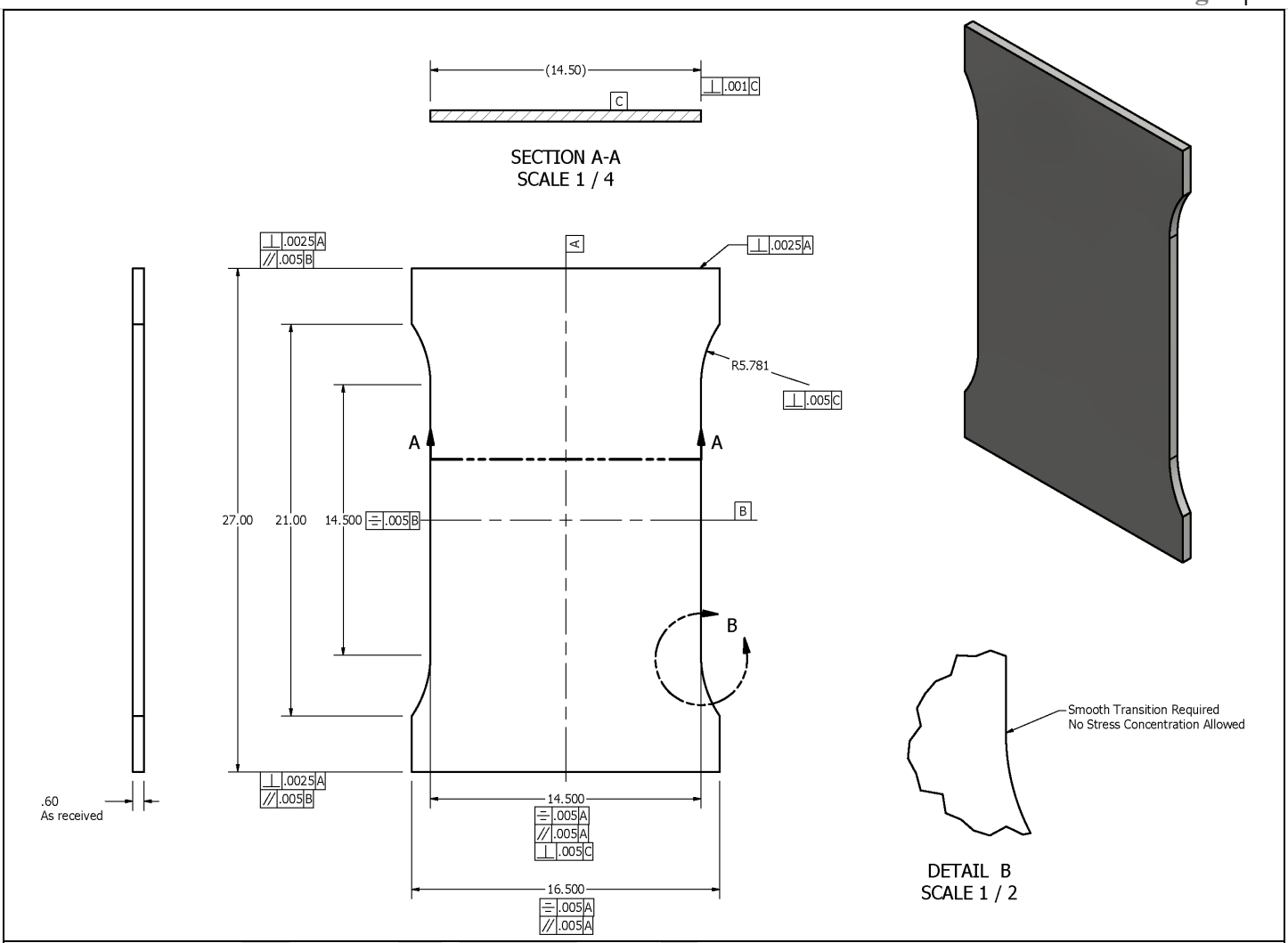

Figure 9. Wide-plate specimen design drawing.

The grips were machined in-house and the specimen assembly and welding were also conducted in-house at a NIST machine shop in Gaithersburg, MD. The test facilities were in Boulder, CO so the specimen assembly was shipped by common freight in a specially designed steel shipping crate. The crate was designed to prevent the specimen from experiencing any strain or damage to the surface. A photo of the specimen in the shipping crate is shown in Figure 11. The photograph shows a protective cover plate (orange) removed from the specimen. The photograph also shows the specimen prepared with a speckled paint pattern necessary for digital image correlation (DIC); details of the DIC system and procedures are given later.

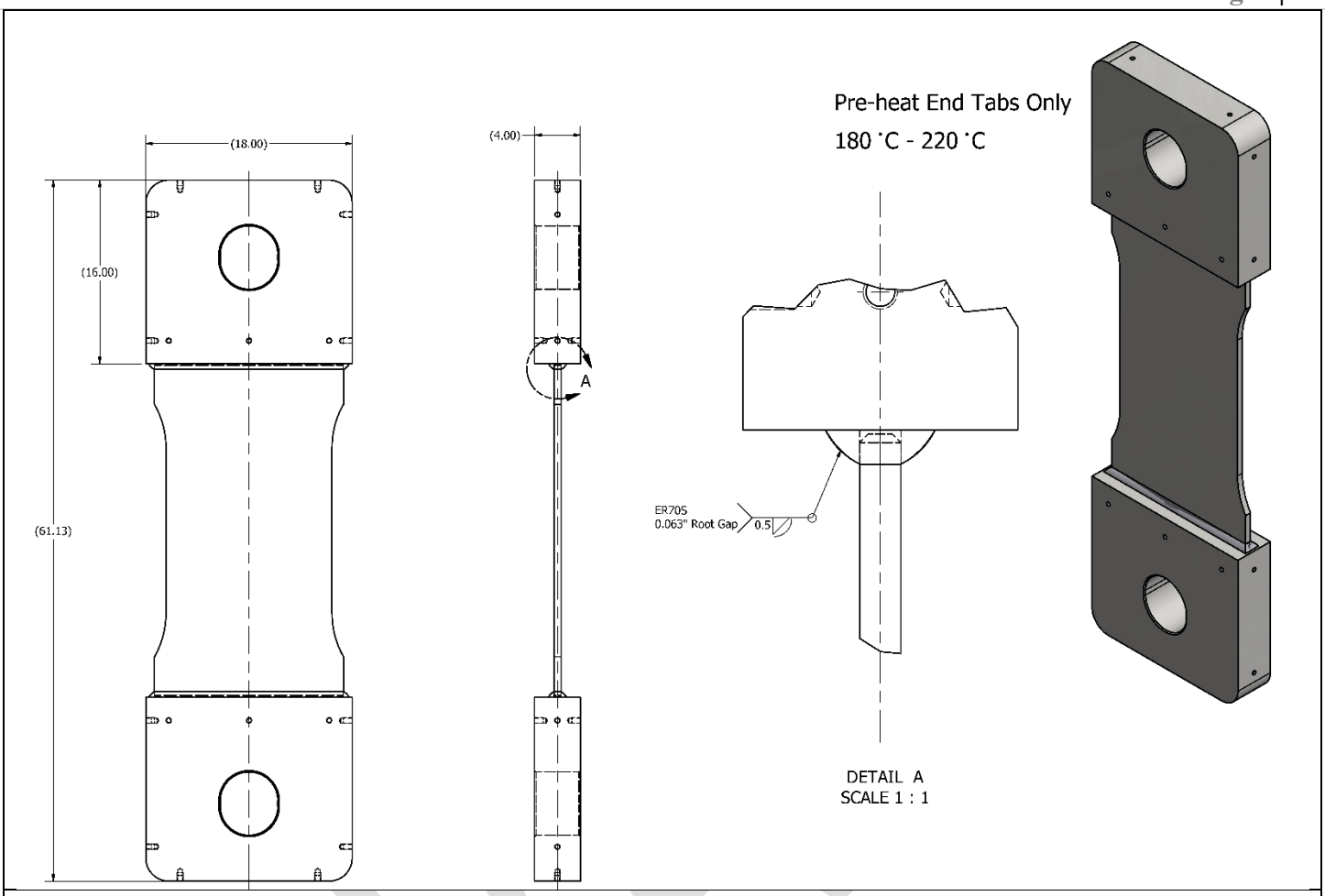

Figure 10. Wide-plate specimen assembly and welding design drawing.

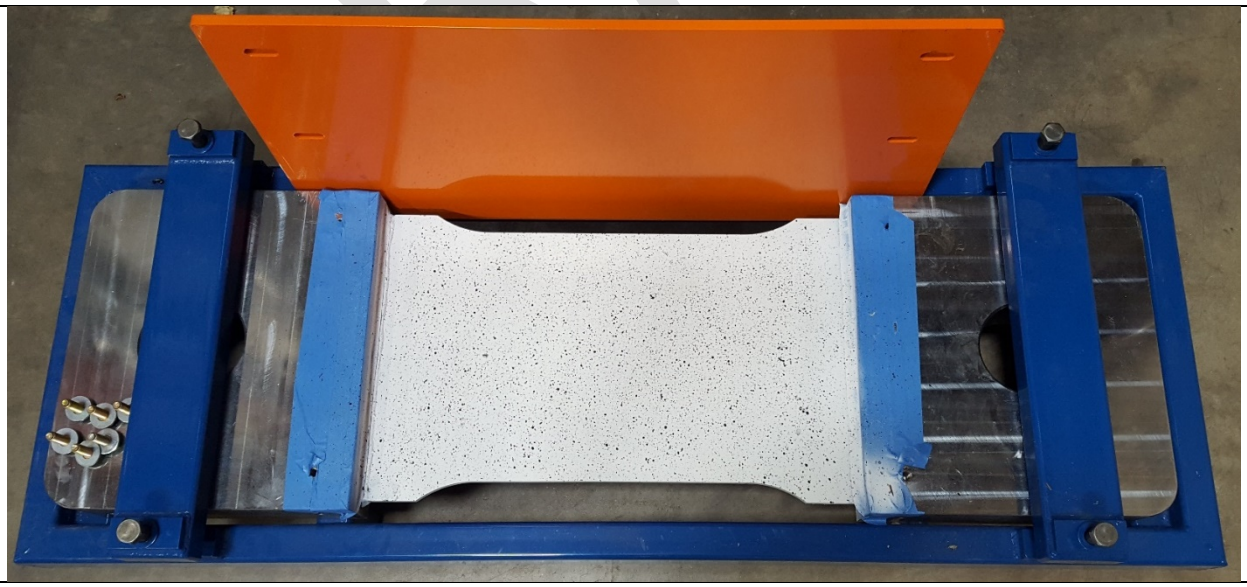

Figure 11. Photograph of the assembled wide-plate specimen in the shipping crate. The surface of the specimen was prepared with a speckle pattern for digital image correlation studies.

Before the specimen was tested, the strain distribution in the plate was estimated using finite element analysis (FEA). The maximum stress was estimated from as-received small-scale tensile specimens and the goal was to pre-strain the plate as close as possible to the maximum stress to maximize the range of pre-strains available for small-scale testing. The results of the FEA are shown graphically in Figure 12.

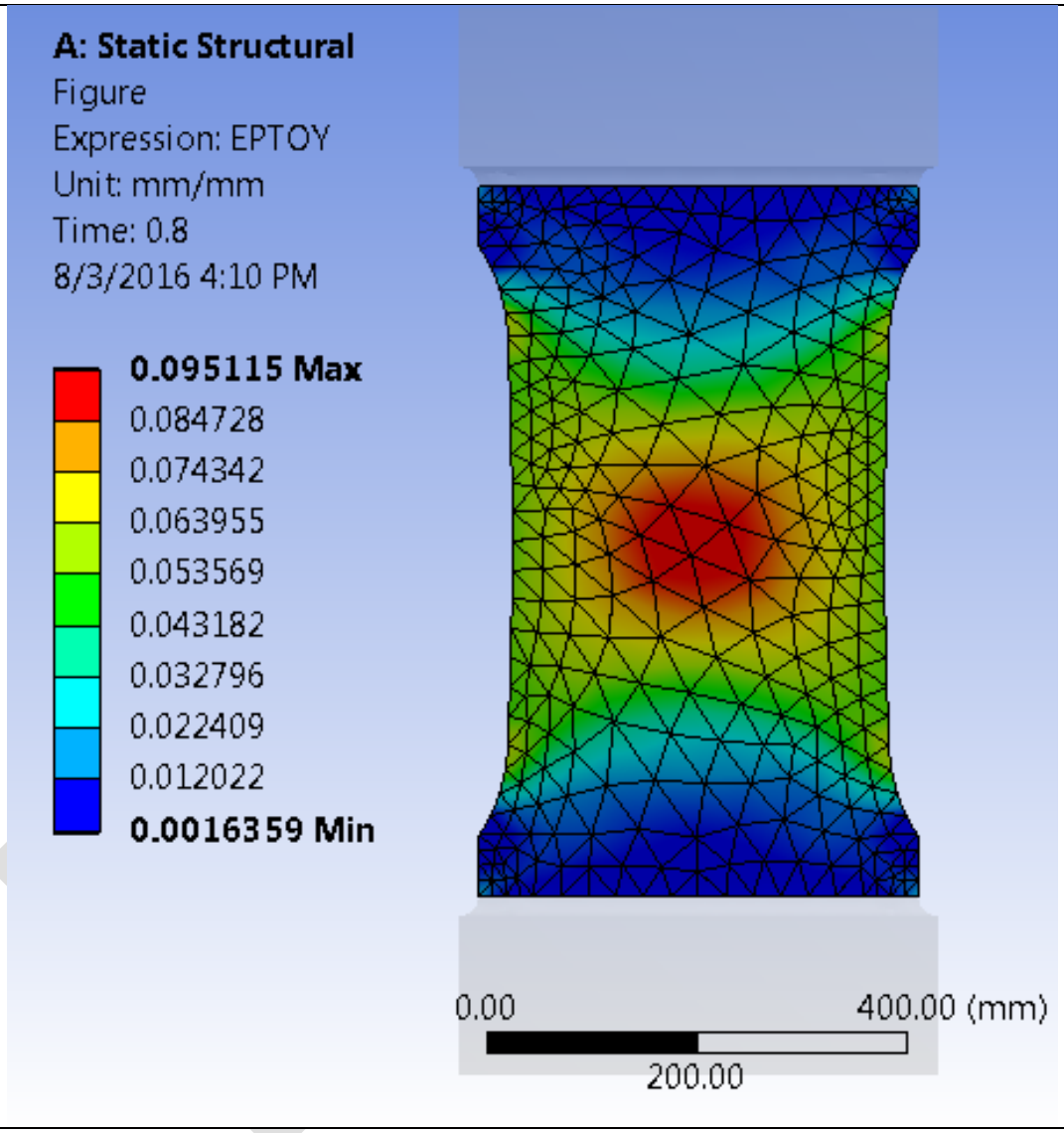

Figure 12. Static structural FEA results estimating the strain distribution in the wide-plate near the maximum stress.

3.2.3.2 Testing Procedures and Equipment

This section details the testing procedure used to pre-strain the wide-plate. All test equipment and measuring instruments were calibrated to a NIST traceable reference and were within allowable uncertainty limits for the instrument considered.

The wide-plate specimen was loaded in tension on a universal servo-hydraulic test machine having a maximum force capacity of 4.4 MN (1 Mlbf). The specimen was loaded at a rate of 0.05 mm/sec (0.002 in/sec) in displacement control to a load-line displacement limit of 50.8 mm (2 in). The displacement limit was determined by importing the small-scale tensile data into the FEA software and reviewing the FEA results. The load-line displacement limit represents the average elastic strain in the plate, knowing that the center of the plate will have greater local strain. The force vs. displacement record for the pre-strained wide-plate is shown in Figure 13.

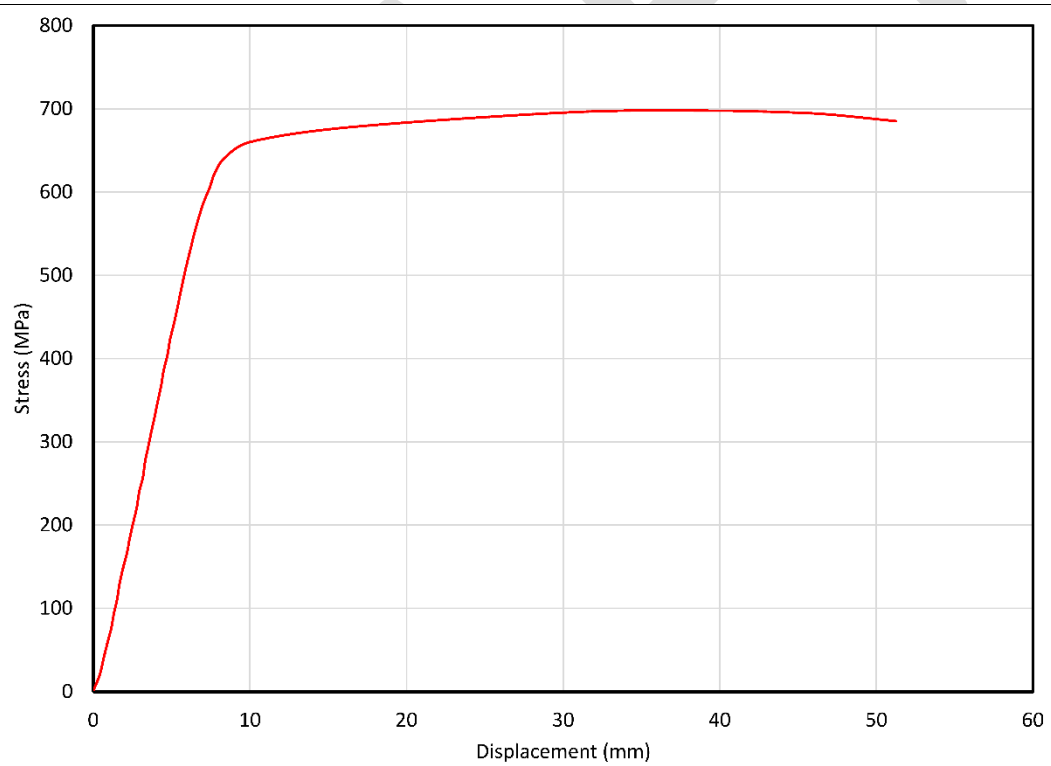

Figure 13. Stress vs. displacement data obtained from pre-straining an X70 wide-plate.

The strain was measured by a three-dimensional digital image correlation (DIC) system. The images were post-processed after pre-straining and were not included in a real-time feedback system associated with the test machine controller. Measurement signals from the test machine controller were acquired by the DIC system to

be synchronized and captured with each DIC image captured. The DIC system captured external data as well as photographs at a rate of 2 hz.

It is not obvious from the stress vs. displacement record in Figure 13 that the wide-plate specimen failed catastrophically. This was not intentional and it significantly complicated further work with the plate. It also significantly complicated the strain analysis. In order to capture the plastic pre-strain, the DIC data from an unloaded specimen is necessary. However, because the specimen failed, the correlation between images is lost and therefore the plastic pre-strain values were estimated from total strain values just prior to failure. It is technically possible to extract plastic strains from the final images but not without an impractical amount of time and effort to do so. The accuracy of the pre-strain values was not critical, whereas the relative changes in pre-strain values presented are appropriate to draw conclusions about the material characterization and structural responses that are predictable using this methodology.

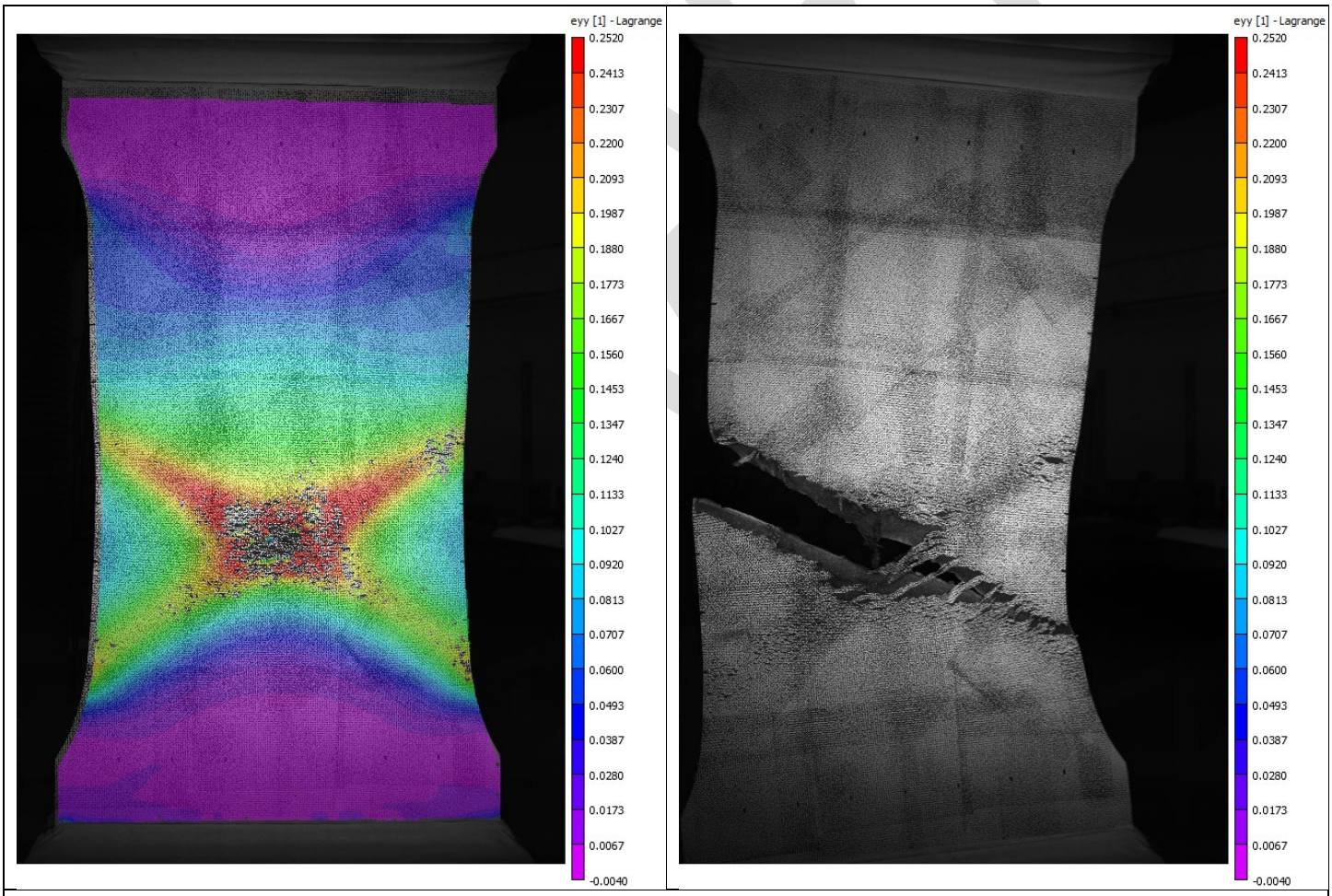

Figure 14. Strain gradients in the wide-plate immediately prior to failure (left) and the failed specimen (right).

3.2.3.3 Sectioning Plan

This section details the plan of the wide-plate pre-strained specimen for the purpose of small-scale testing in all three directions; longitudinal to the pre-straining direction of the plate, transverse to the pre-straining direction and the through-thickness direction. The sectioning plan is shown in Figure 15 along with a photograph of the sectioned wide-plate. All sectioning was completed by water-jet cutting to eliminate the possibility of material changes associated with high temperatures from other cutting methods.

From the numbered blanks (see Figure 15) the following small-scale specimens were machined:

- round tensile
- mini-tensile (rectangular cross section)
- cylinders
- notched bar impact (Charpy V-Notch).

DRAFT

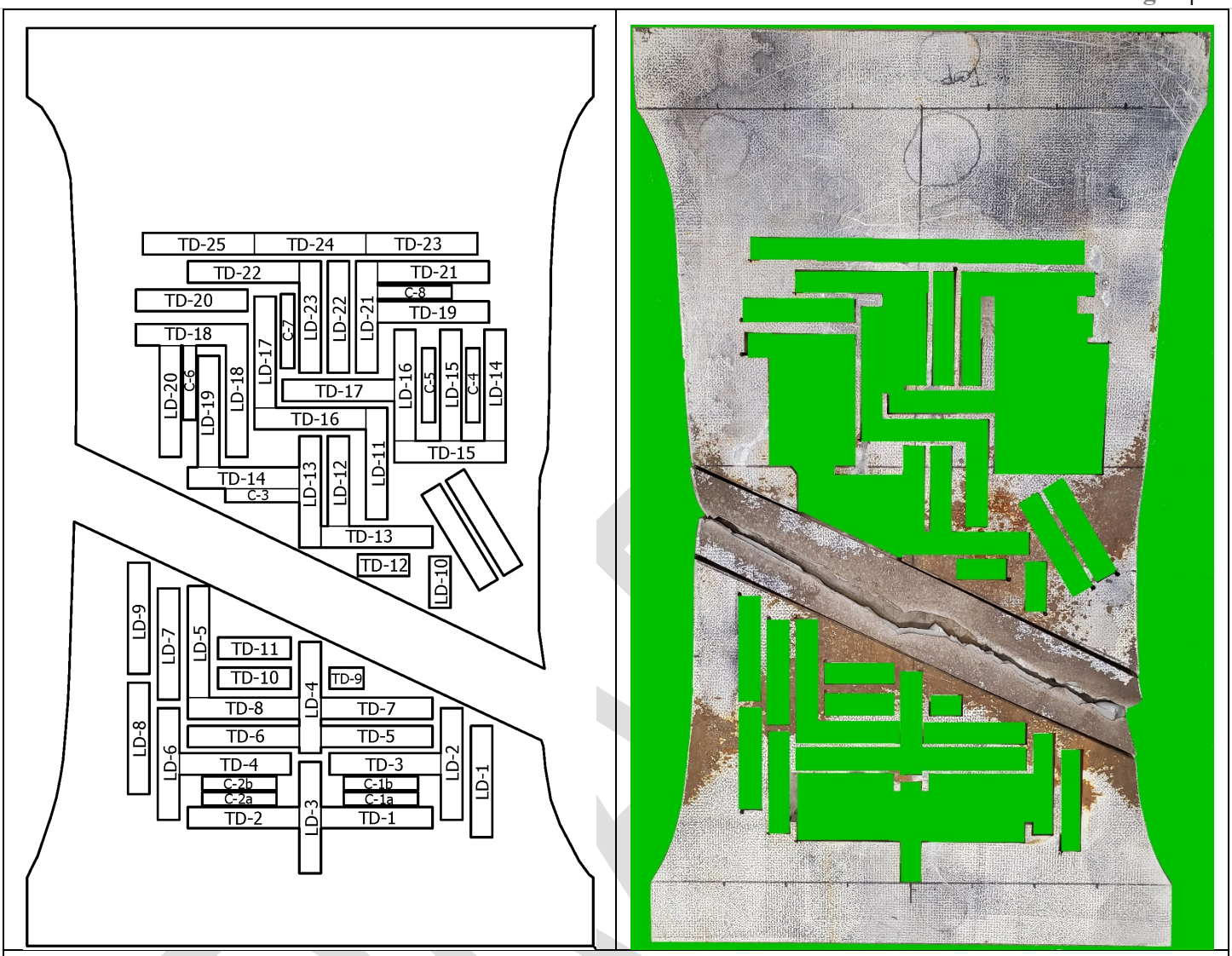

Figure 15. Diagram of the pre-strained wide-plate sectioning plan for small scale testing (left) and a photograph of the sectioned wide-plate (right).

Round tensile specimens were machined from the pre-strained numbered blanks according to the machine drawing shown in Figure 3. This alternate geometry is the only difference between pre-strained specimen geometries and those used to determine as-received properties.

The tensile test matrix of specimen blanks is presented in Table 6, which includes the specimen type, orientation and longitudinal pre-strain level. Fourteen specimens were machined from each of the mini-tensile blanks, seven from the stated orientation and seven from the through-thickness direction. Compression cylinders were also machined from blanks adjacent to mini-tensile specimens for future research.

Table 6. Tensile test matrix for pre-strained X70 plate.

Longitudinal Blanks		Transverse Blanks	
Blank ID/Type	**Pre-strain Level (%)**	**Blank ID/Type**	**Pre-strain Level (%)**
LD-01/Round Tensile	7.4	TD-02/Round Tensile	8.3
LD-02/Mini-Tensile	7.0	TD-03/Mini-Tensile	5.7
LD-03/Round Tensile	2.0	TD-04/Round Tensile	3.9
LD-04/Round Tensile	10.9	TD-05/Round Tensile	8.5
LD-05/Round Tensile	17.1	TD-06/Mini-Tensile	5.7
LD-06/Mini-Tensile	7.7	TD-07/Round Tensile	10.5
LD-07/Round Tensile	15.1	TD-08/Round Tensile	9.2
LD-08/Round Tensile	12.2	TD-10/Mini-Tensile	14.4
LD-09/Round Tensile	12.3	TD-11/Mini-Tensile	20.5
LD-11/Round Tensile	14.0	TD-13/Round Tensile	15.9
LD-13/Round Tensile	15.9	TD-14/Round Tensile	14.2
LD-14/Round Tensile	9.7	TD-15/Round Tensile	13.7
LD-15/Round Tensile	9.3	TD-16/Round Tensile	11.4
LD-16/Mini-Tensile	9.7	TD-17/Round Tensile	10.3
LD-17/Round Tensile	9.7	TD-18/Mini-Tensile	7.3
LD-18/Round Tensile	10.3	TD-19/Round Tensile	6.5
LD-19/Round Tensile	11.0	TD-20/Round Tensile	6.0
LD-20/Mini-Tensile	9.7	TD-21/Round Tensile	5.3
LD-21/Mini-Tensile	6.6	TD-22/Mini-Tensile	4.6
LD-22/Round Tensile	6.7	TD-23/Mini-Tensile	4.2
LD-23/Mini-Tensile	6.7	TD-24/Mini-Tensile	2.6
		TD-25/Round Tensile	3.9

The Charpy V-Notch specimens were sectioned from blanks designated in Figure 15. The crack plane and crack path varied, and each specimen was tested at room temperature (21 ℃). The Charpy V-Notch test matrix is given in Table 7, where the specimen ID, crack plane and crack direction are all described.

Table 7. Pre-strained X70 Charpy V-Notch Test Matrix – Orientation Effects

Specimen ID	Crack Plane	Crack Direction
C1a	L-TT	Through-Thickness
C1b	L-TT	Longitudinal
C2a	L-TT	Through-Thickness
C2b	L-TT	Longitudinal
C3	L-TT	Longitudinal
C4	T-TT	Through-Thickness
C5	T-TT	Transverse
C6	T-TT	Transvers
C7	T-TT	Through-Thickness
C8	T-TT	Through-Thickness

3.3 Material Testing and Results

3.3.1 Physical Metallurgy

3.3.1.1 Chemical Composition

The chemical composition of the as-received plate was determined by atom emission spectroscopy and compared against the specification for X70 PSL1 seamless pipe found in the 45th edition of the American Petroleum Institute (API) 5L specification.

Table 8. Chemical Analysis of as-received X70 plate

Element	Specified Maximum (%)	Actual (%)
B	0.001	<0.001
C	0.28	0.05
Cr	0.50	0.04
Cu	0.5	0.03
Mn	1.40	1.60*
Mo	0.15	0.01
Nb	--	0.057
Nb + V + Ti	0.15	0.07
Ni	0.5	0.04
P	0.03	0.009
S	0.03	0.006
Ti	--	0.012
V	--	0.003

* Note: For each reduction of 0.01 % below the specified maximum concentration for C an increase of 0.05 % above the specified maximum concentration for Mn is permissible, up to a maximum of 2.00 %.

3.3.1.2 Microstructure

Optical micrographs of as-received and pre-strained steel are presented in this section. Standard metallographic preparation and analysis was performed on the steel in several orientations. Metallography of samples etched with 2% nitric acid in methanol revealed a uniform meso-structure and microstructure. Segregation of secondary phases or higher carbon steel microstructures was not observed. The view designations are shown in Figure 16, followed by the individual micrographs. Specimen plane-A allows a view normal to the rolling direction with the longitudinal (plate) direction on the horizontal axis of the micrograph and the through-thickness direction shown on the vertical axis of the micrograph. Specimen plane-B allows a view orthogonal to the rolling direction with the rolling direction on the horizontal axis of the micrograph and the through-thickness direction shown on the vertical axis off the micrograph. Specimen plane-C and plane-D are on the surfaces of the plate and should result in similar images (see Figure 16(C) and (D)), these planes allow a view normal to the through thickness direction with the rolling direction on the vertical axis of the micrographs and the longitudinal

DRAFT

(plate) direction on the horizontal axis of the micrographs. Finally, the planar view of C & D (through-thickness) is examined at the mid-plane of the plate in plane-E.

The micrographs shown are expected, showing a uniformly distributed fine-grained (~5-9 μm) ferritic microstructure. The grains are elongated as expected in the rolling direction, which as shown are evident in planes B, C and D. Plane-E doesn't show an obvious grain elongation or directionality caused by rolling the plate. Significant directionality is not expected in plane-A and is confirmed by the micrograph.

DRAFT

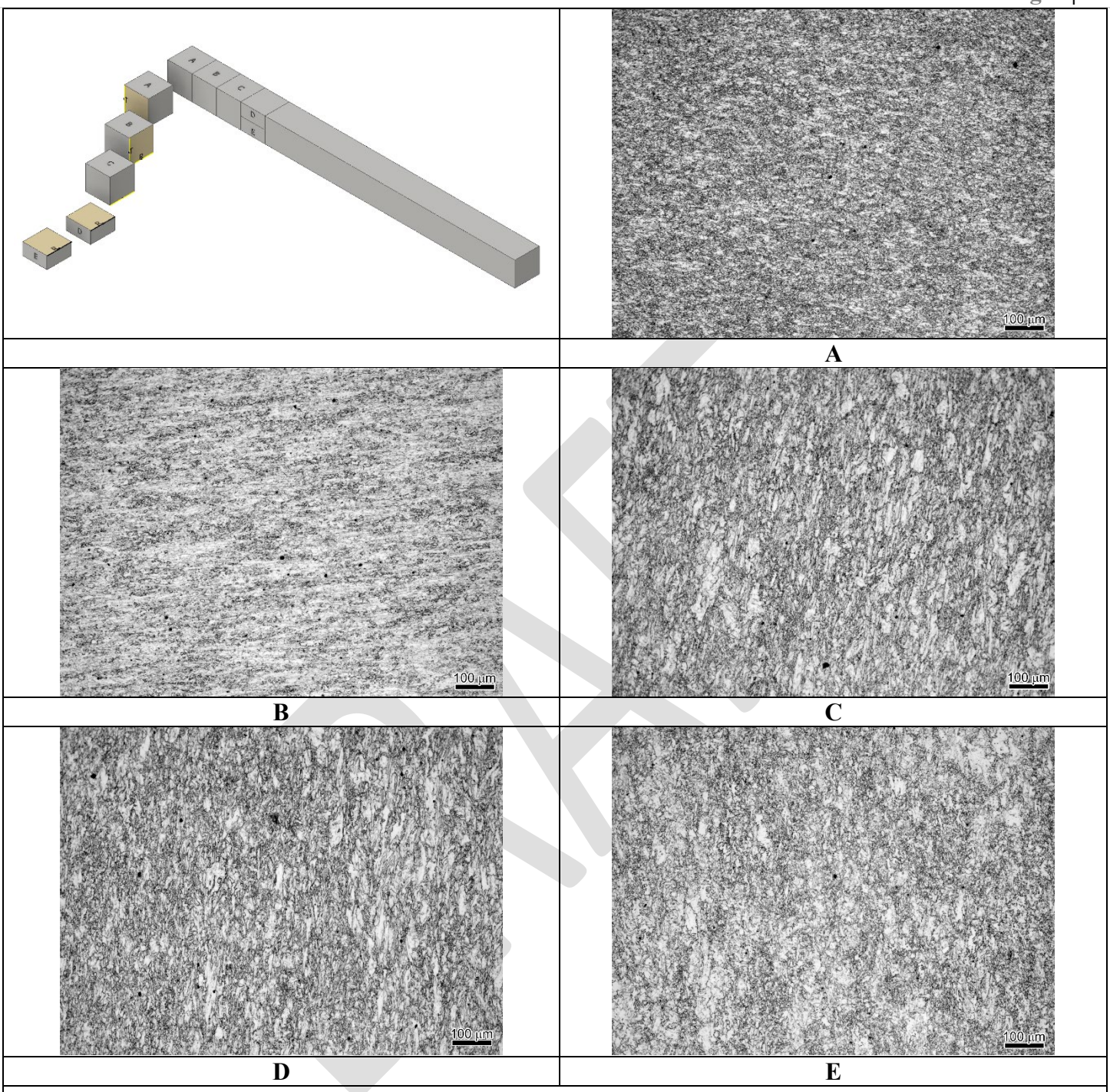

Figure 16. Diagram indicating metallographic views and orientation (upper left). Optical micrographs corresponding to specimen planes A-E for as-received X70.

The micrographs shown for pre-strained material (LD-12 – 14.9 %) are also unremarkable, showing a uniformly distributed fine-grained (~4-8 µm) ferritic microstructure. The grains are elongated as expected in the rolling direction, which as shown are evident in planes B, C and D. Plane-E doesn't show an obvious grain elongation or directionality caused by rolling the plate. Significant directionality is not expected in plane-A and

is confirmed by the micrograph. The pre-strain direction is normal to plane-B. The view designations are shown in Figure 17, followed by the individual micrographs.

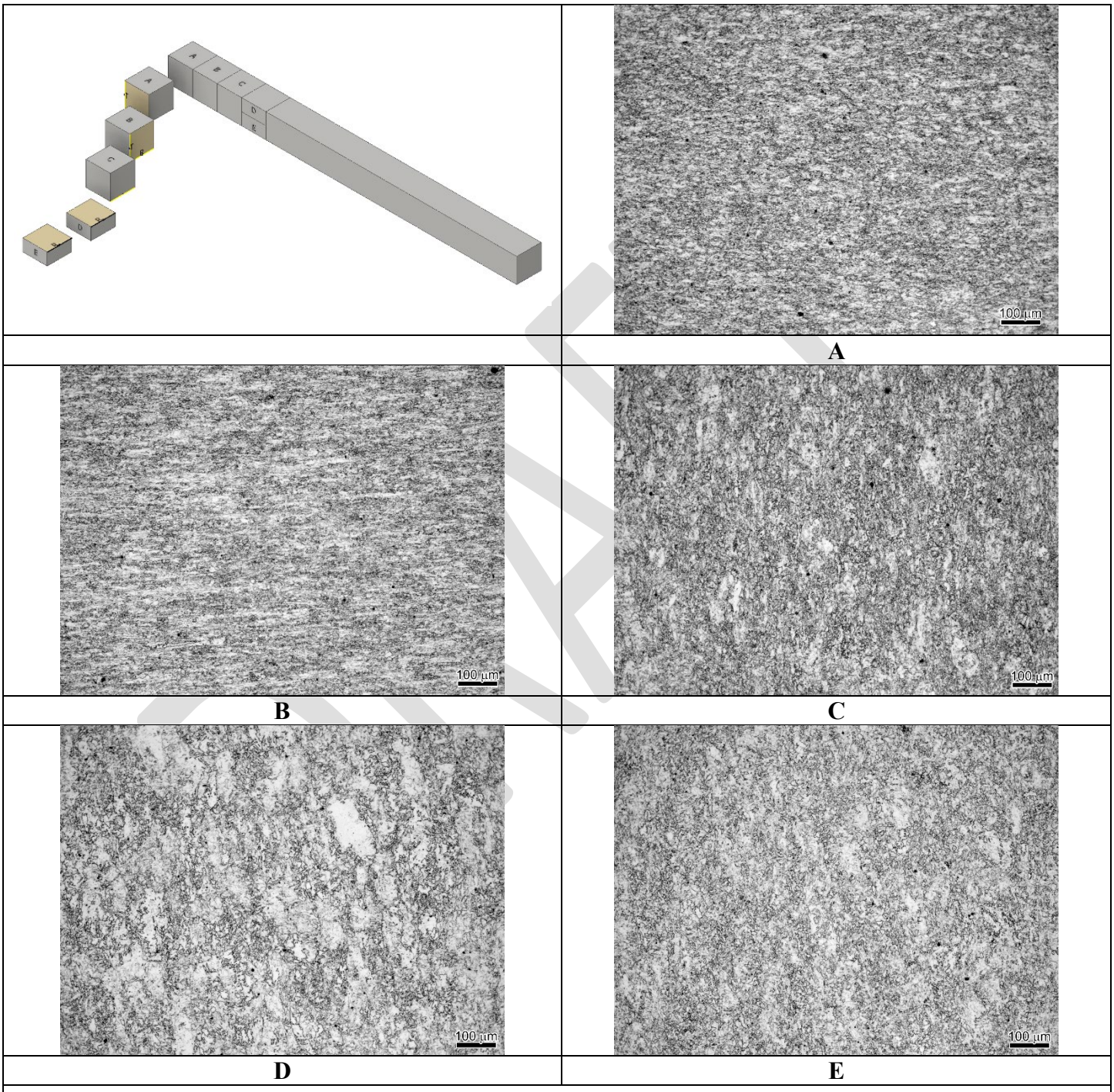

Figure 17. Diagram indicating metallographic views and orientation (upper left). Optical micrographs corresponding to specimen planes A-E for pre-strained X70.

3.3.1.3 Texture

To further characterize the as-received X70 sections, crystallographic texture was characterized by electron backscatter diffraction (EBSD) of polished samples in a scanning electron microscope (SEM) operated at 30 kV. Scans were 200x200 µm with 0.5 µm steps. The same planes as these presented in Figure 16 and Figure 17 were examined in the SEM.

The as-received X70 shows a clear rolled microstructure with distinct orientation texture in each direction. Plane-A shows a strong <111> out-of-plane texture with limited banding. In plane-B a clear banding can be seen where the strong <101> out-of-plane texture is layered with bands showing orientations rotating towards <111>. Clear elongation of the grains in the rolling/banding direction is also evident. In plane-C, banding is not seen, and the out-of-plane texture is primarily <001>, with smaller areas of <111>, or orientations in between the two poles. Through the thickness of the plate (comparing C, D, and E planes) shows similar textures though plane-E shows less <001>, and more grains oriented towards the <111> orientation.

EBSD results presented here include crystallographic orientation maps of as-received X70 (see Figure 18), pole plots (see Figure 20) and vector plots (see Figure 22). The average grain size in each view is recorded in Figure 18.

In the pre-strained material, there are some differences in the microstructure developed. One consequence of the pre-straining is that the grain size is smaller (for all planes except plane-D). While the grain size is variable across the different directions in the material and considering the EBSD software potentially counted multiple closely oriented neighboring grains as a single grain, there is still a difference in the average grain size from 6 µm in the pre-strained material compared to 6.8 µm in the as-received material. In plane-A, the banded microstructure still exists but the dominant out-of-plane orientation has rotated to <111>. In plane-B, the texture is softened, with the <101> out-of-plane orientation less dominant, and the grains are more equiaxed in nature. The C, D and E planes showed relatively little difference between the two material conditions.

EBSD results presented here include crystallographic orientation maps of pre-strained material (see Figure 19), pole plots (see Figure 21) and vector plots (see Figure 23). The average grain size in each view is recorded in Figure 19.

DRAFT

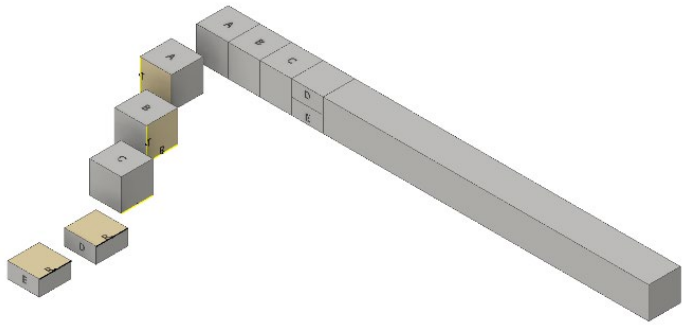

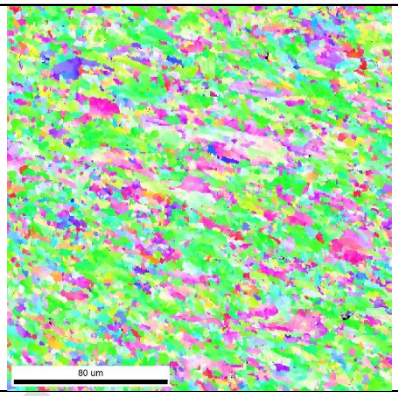

A
(Grain size = 5.23 µm)

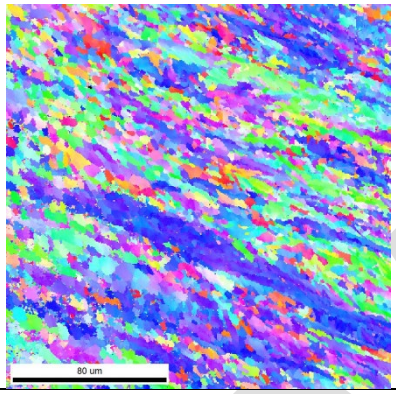

B
(Grain size = 8.84 µm)

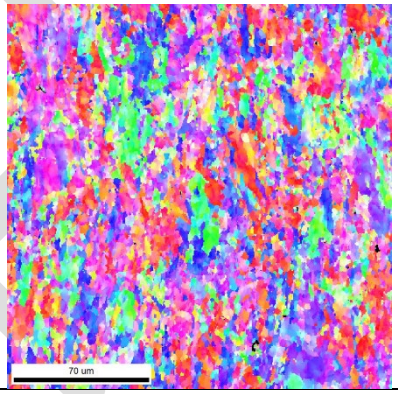

C
(Grain size = 6.05 µm)

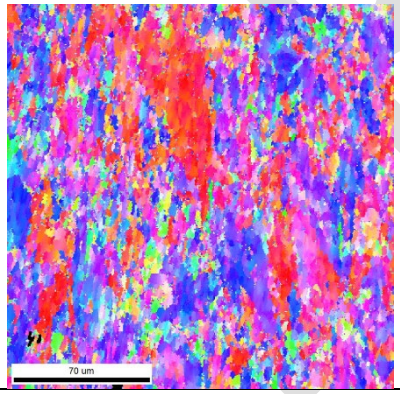

D
(Grain size = 6.85 µm)

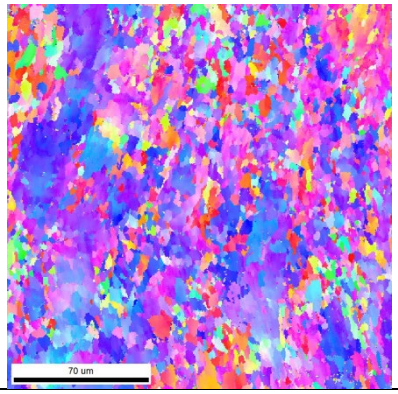

E
(Grain size = 6.91 µm)

Figure 18. Diagram indicating SEM views and orientation (upper left). EBSD crystallographic orientation maps corresponding to specimen planes A-E for as-received X70.

DRAFT

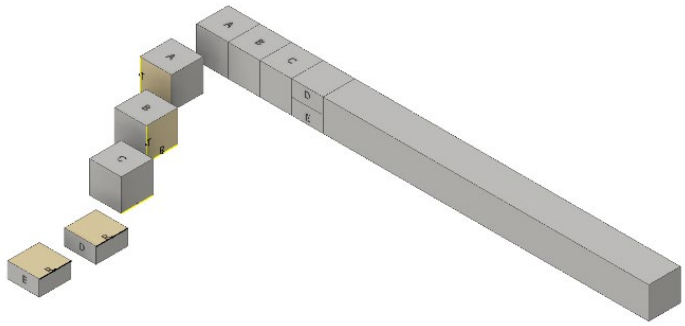

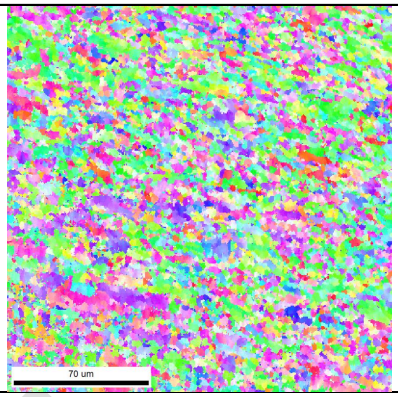

A
(Grain size = 4.07 µm)

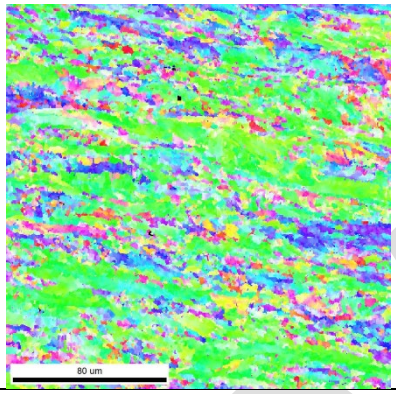

B
(Grain size = 5.94 µm)

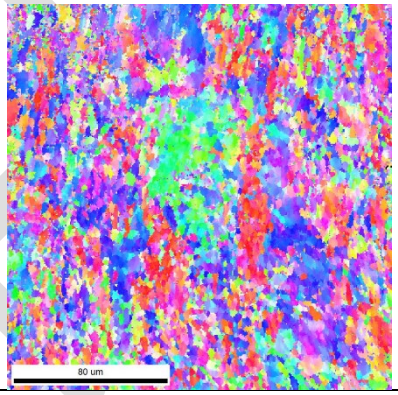

C
(Grain size = 5.36 µm)

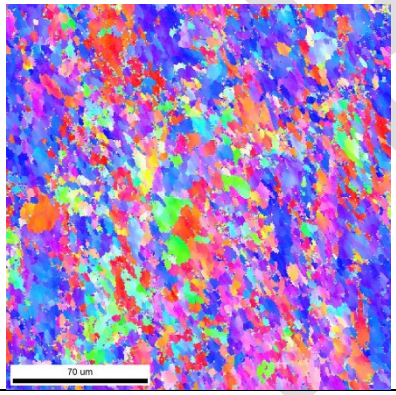

D
(Grain size = 7.90 µm)

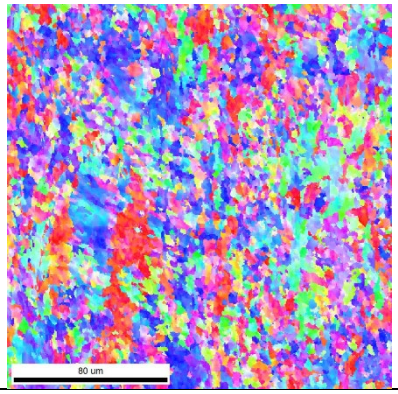

E
(Grain size = 6.57 µm)

Figure 19. Diagram indicating SEM views and orientation (upper left). EBSD crystallographic orientation maps corresponding to specimen planes A-E for pre-strained X70.

DRAFT

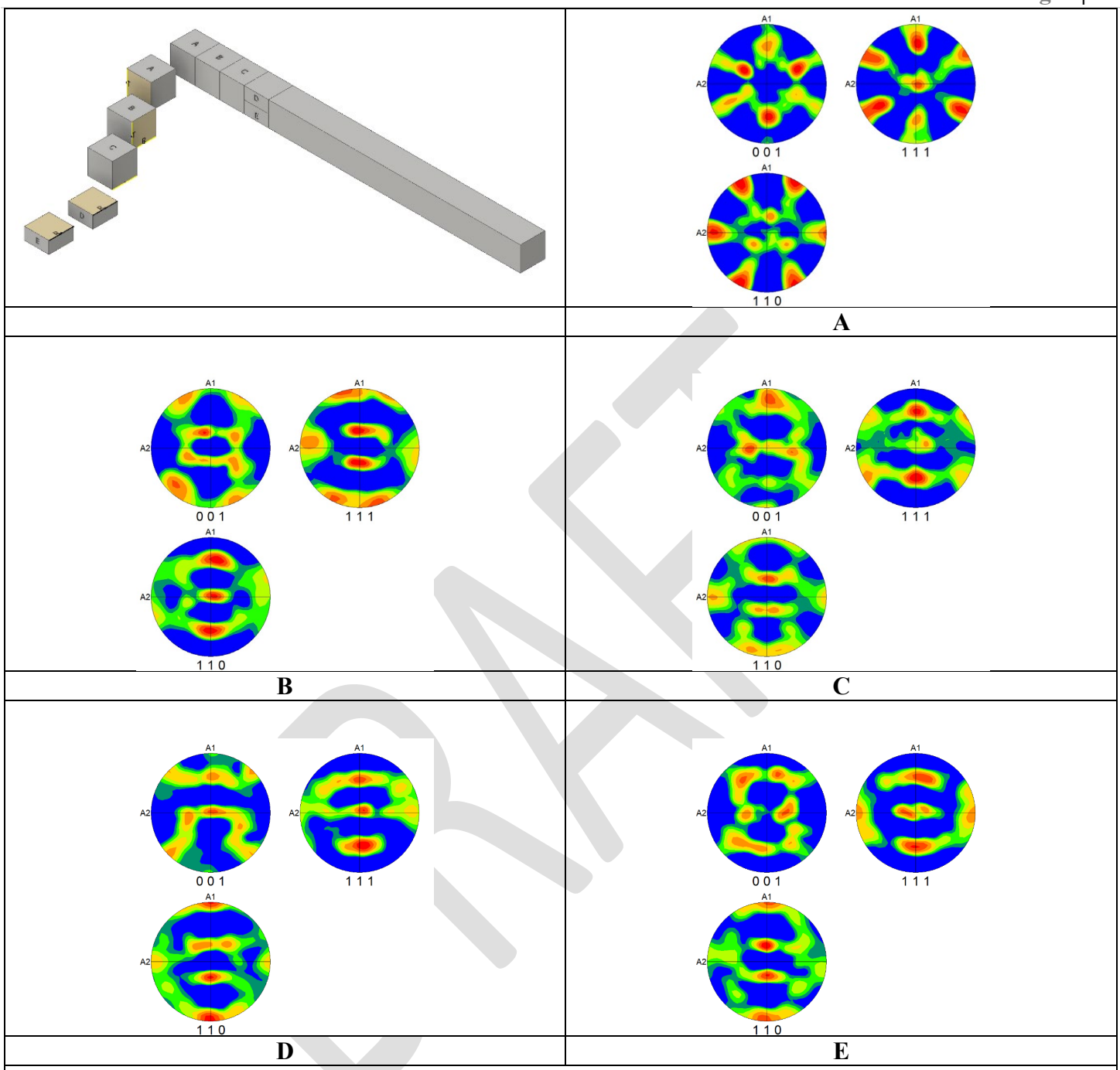

Figure 20. Diagram indicating SEM views and orientation (upper left). EBSD orientation pole plots corresponding to specimen planes A-E for as-received X70.

DRAFT

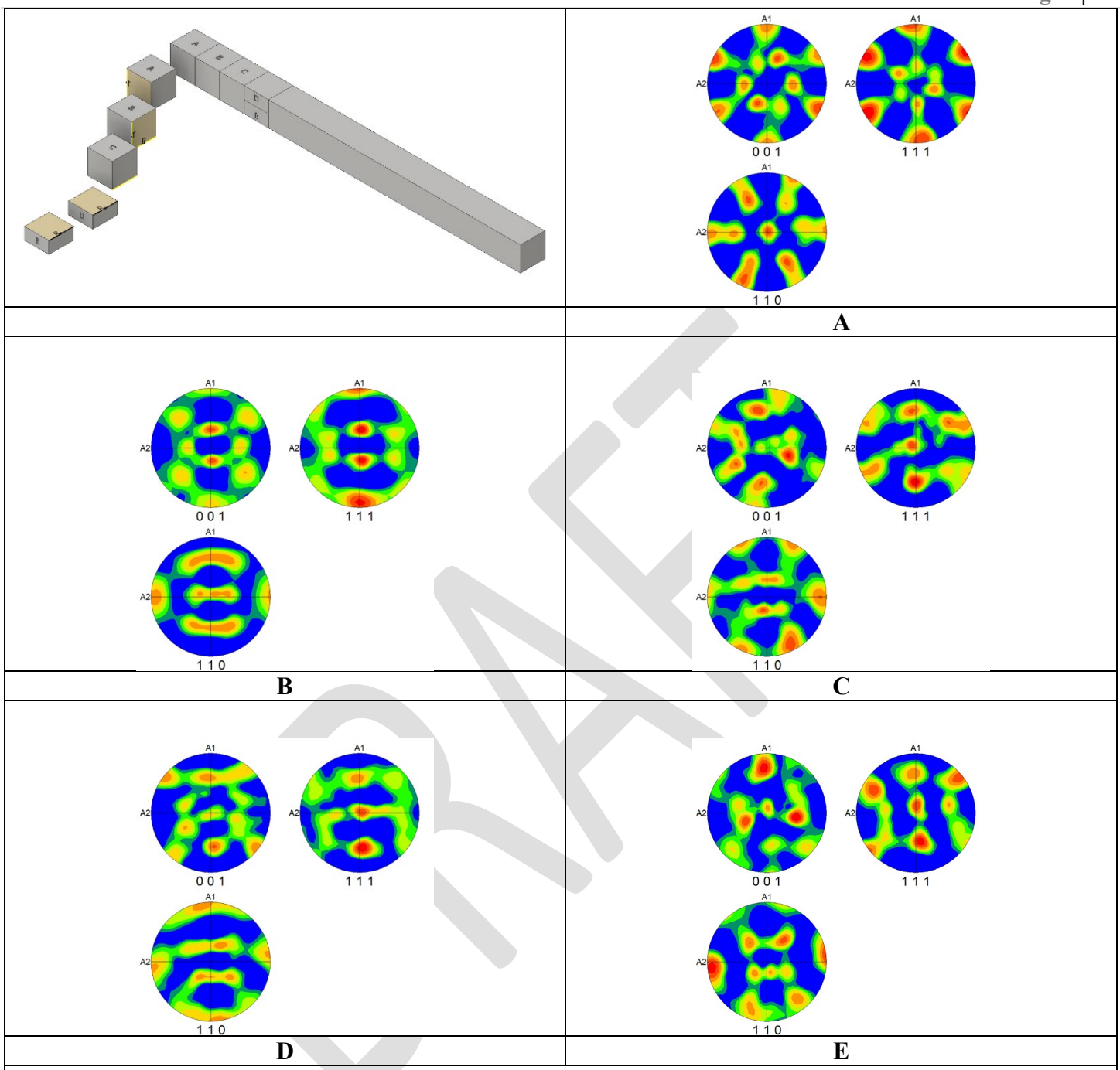

Figure 21. Diagram indicating SEM views and orientation (upper left). EBSD orientation pole plots corresponding to specimen planes A-E for pre-strained X70.

DRAFT

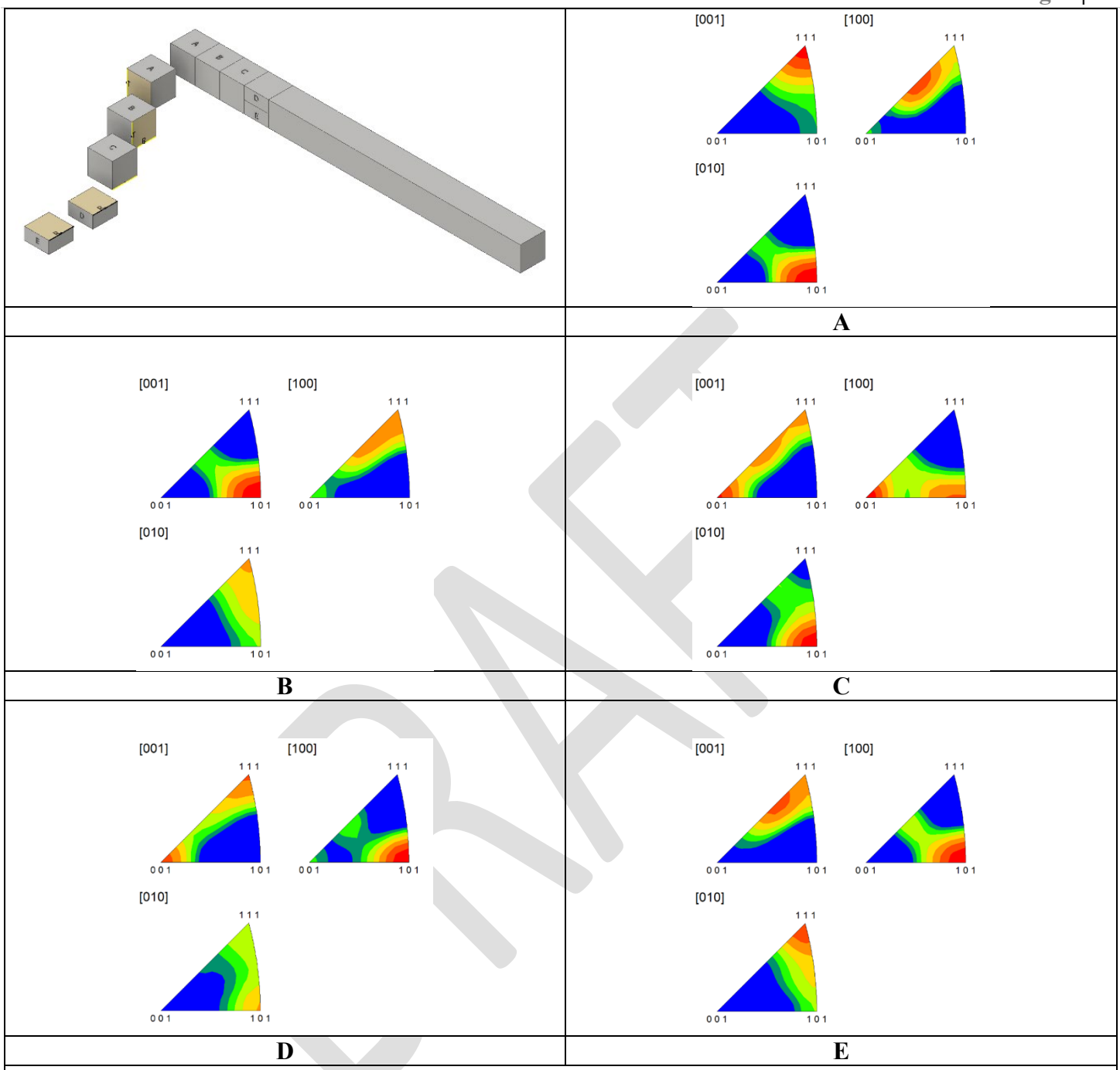

Figure 22. Diagram indicating SEM views and orientation (upper left). EBSD orientation vector plots corresponding to specimen planes A-E for as-received X70.

DRAFT

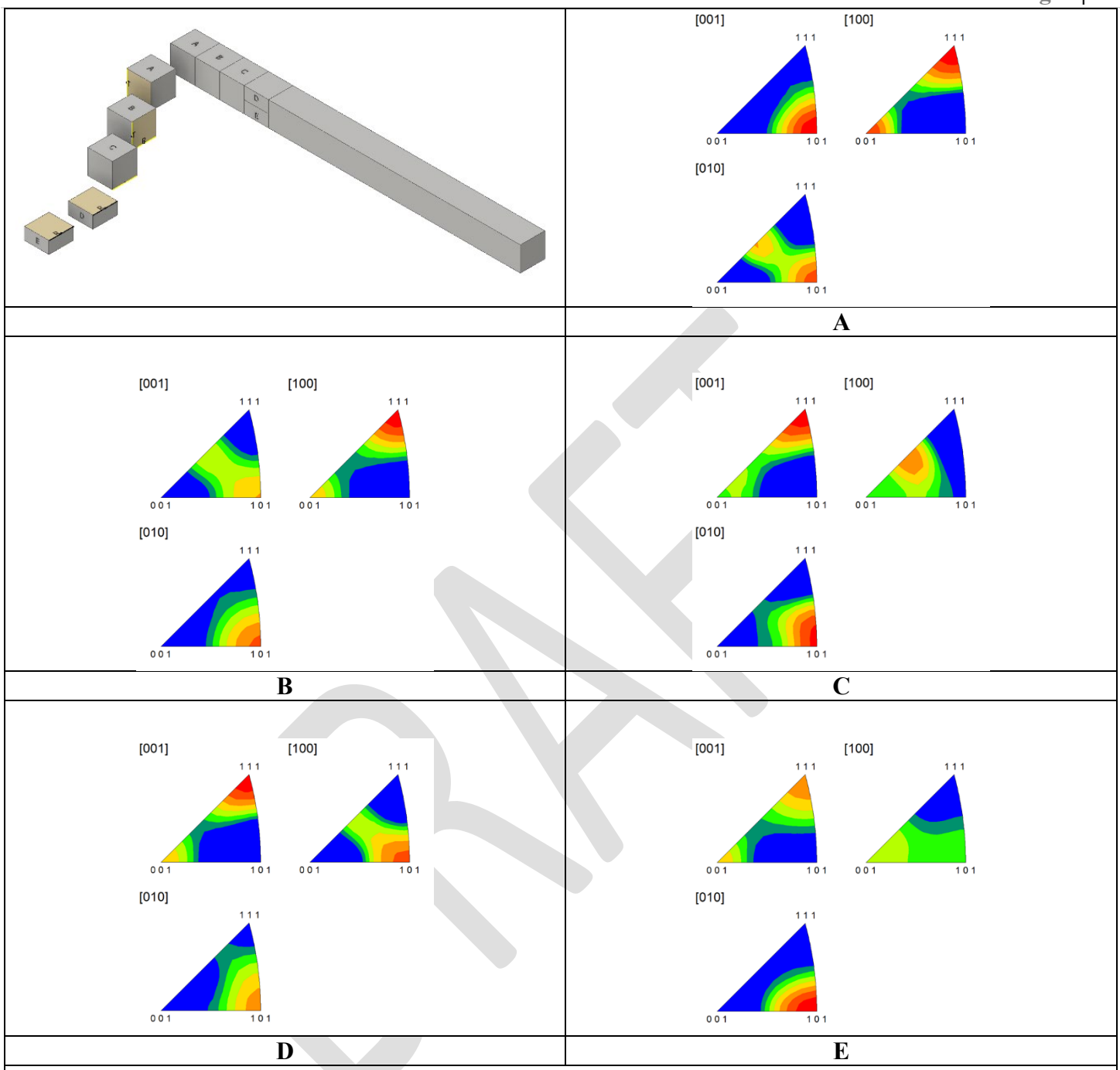

Figure 23. Diagram indicating SEM views and orientation (upper left). EBSD orientation vector plots corresponding to specimen planes A-E for pre-strained X70.

DRAFT

3.3.2 Mechanical Metallurgy

3.3.2.1 Tensile Testing – As-Received Material

This section presents the test results on as-received material from each of the tests in tabular and graphic formats. Average values and standard deviations are given where appropriate.

The tensile tests were analyzed to obtain the elastic modulus (E), yield stress defined at 0.5 % strain ($YS_{0.5\,\%}$), strain energy density at yield (U_{YS}), maximum stress (ultimate tensile strength (UTS)) (σ_{UTS}), strain at UTS ($\varepsilon_{\mathrm{UTS}}$), strain energy density at UTS (U_{UTS}), stress at failure (σ_f) , strain at failure (ε_f), and the strain energy density at failure (U_f). These data are separated into two tables for easier and more focused comparison. Table 9 presents the elastic modulus and stress values while Table 10 presents the strain and strain energy density data. The tables report the average values, standard deviations and coefficient of variations (CV) for each sample of specimens.

The elastic moduli were calculated for each specimen using ASTM's Standard Practice for Determination of the Slope in the Linear Region of a Test Record. This standard practice provides a procedure for numerically finding the most linear region in a given test record. The practice analyzes residuals and is often more robust than conventional least squares fitting techniques based on a correlation coefficient especially when the underlying physics indicate that the relationship between stress and strain is linear. There were some specimens where the residuals methodology produced a result very different than would be determined from a more pragmatic engineering analysis. For example, for some cases the range over which the slope was determined was too narrow or was not in the initial linear region where truly elastic behavior is expected. By either method, the best practical values of elastic moduli are presented. There is clear bias and scatter in the moduli data as shown in Table 9 for the various orientations. The bias may be a legitimate difference based on orientation, but other comparisons are difficult if not impossible. Modulus data from tensile testing especially with clip-on extensometers is notoriously problematic yet is generally valuable to provide a validity check on other data. A robust and valuable comparison in material behavior requires that measurement errors and uncertainties are reduced as much as possible. One way to accomplish this is to correct all the strain data to ensure that the initial material response is always the same; that is, fix the modulus within an appropriate range and shift the remaining strain data accordingly. All strain data and strain energy density data correspond to a modulus correction to 195 GPa. Elastic modulus has been considered a damage parameter by some researchers using a continuum damage mechanics approach to failure. The approach here is to set the modulus to be equal for each orientation and pre-strain condition to determine if other parameters are better suited to predicting material behavior based on a known strain history or conversely being able to estimate the strain history from a steel sampling with many unknowns.

DRAFT

Table 9. As-received X70 Round Tensile Results – Comparative Stress Values				
Specimen ID	**Elastic Modulus (GPa)**	**Yield Stress at 0.5 % Strain (MPa)**	**Max Stress (UTS) (MPa)**	**Failure Stress (MPa)**
X70-3-1	163	562	651	329
X70-3-2	177	558	651	333
X70-4-1	189	561	652	332
X70-4-2	193	559	656	336
Average	**181**	**560**	**653**	**333**
Standard Deviation	**14**	**2**	**2**	**3**
CV (%)	**7.5**	**0.3**	**0.4**	**0.9**
X70-13-1	230	636	692	353
X70-13-2	222	642	703	371
X70-15-2	235	627	690	351
X70-16-1	228	633	689	350
X70-16-2	223	630	689	352
X70-18-2*	234	639	689	372
X70-18-3	232	636	691	357
X70-18-4	214	646	704	377
X70-19-4	230	641	704	368
Average	**228**	**637**	**695**	**361**
Standard Deviation	**7**	**6**	**7**	**11**
CV (%)	**3.0**	**0.9**	**1.0**	**2.9**
X70-26-1	176	612	627	301
X70-26-2	187	582	634	314
X70-27-2	187	584	641	319
Average	**183**	**593**	**634**	**311**
Standard Deviation	**5**	**14**	**6**	**8**
CV (%)	**2.9**	**2.3**	**0.9**	**2.4**
X70-18-1*	241	643	686	350
X70-19-1*	235	635	685	343
X70-19-2*	266	637	688	348
X70-19-3*	245	640	691	357
Average	**247**	**639**	**688**	**350**
Standard Deviation	**13**	**4**	**3**	**6**
CV (%)	**5.5**	**0.5**	**0.4**	**1.7**

* Reduced gauge-length round specimen

DRAFT

Table 10. As-received X70 Round Tensile Results – Comparative Strain and Strain Energy Density Values

Specimen ID	Strain at UTS (mm/mm)	Strain at Failure (mm/mm)	*U* at Yield (J/m^3)	*U* at UTS (J/m^3)	*U* at Failure (J/m^3)
X70-3-1	0.0995	0.1930	1.8	61.7	114.8
X70-3-2	0.1129	0.2227	1.8	70.3	133.2
X70-4-1	0.1016	0.1759	1.7	63.2	104.2
X70-4-2	0.0902	0.1862	1.7	55.9	111.0
Average	**0.1011**	**0.1945**	**1.8**	**62.8**	**115.8**
Standard Deviation	**0.0093**	**0.0201**	**0.1**	**5.9**	**12.4**
CV (%)	**9.2**	**10.3**	**3.4**	**9.4**	**10.7**
X70-13-1	0.0675	0.1722	2.0	44.7	108.0
X70-13-2	0.0698	0.1611	2.0	46.9	102.6
X70-15-2	0.0684	0.1860	2.0	45.0	116.7
X70-16-1	0.0768	0.1861	2.0	50.9	116.8
X70-16-2	0.0666	0.1695	2.0	43.8	105.7
X70-18-2*	0.0574	0.2326	2.0	36.6	128.4
X70-18-3	0.0600	0.1210	2.0	39.5	77.0
X70-18-4	0.0619	0.1340	2.0	41.5	85.0
X70-19-4	0.0702	0.1859	2.0	47.3	120.1
Average	**0.0665**	**0.1720**	**2.0**	**44.0**	**106.7**
Standard Deviation	**0.0059**	**0.0325**	**0.0**	**4.3**	**16.7**
CV (%)	**8.9**	**18.9**	**0.0**	**9.8**	**15.6**
X70-26-1	0.0633	0.1796	2.0	38.3	101.6
X70-26-2	0.0662	0.1799	1.9	39.9	103.0
X70-27-2	0.0804	0.1810	1.9	49.4	105.0
Average	**0.0700**	**0.1802**	**1.9**	**42.5**	**103.2**
Standard Deviation	**0.0075**	**0.0006**	**0.1**	**5.0**	**1.4**
CV (%)	**10.7**	**0.3**	**3.1**	**11.5**	**1.4**
X70-18-1*	0.0630	0.2402	1.9	39.8	130.4
X70-19-1*	0.0606	0.2503	2.0	38.3	135.3
X70-19-2*	0.0620	0.2311	2.0	39.4	126.3
X70-19-3*	0.0628	0.2330	2.0	40.0	128.1
Average	**0.0621**	**0.2387**	**2.0**	**39.4**	**130.0**
Standard Deviation	**0.0011**	**0.0087**	**0.1**	**0.8**	**3.9**
CV (%)	**1.8**	**3.6**	**2.5**	**1.9**	**3.0**

* Reduced gauge-length round specimen

The full stress-strain curves for each specimen are shown in the following figures; Figure 24 shows the results of tensile tests of round tensile specimens tested in the longitudinal direction (transvers to the rolling direction), Figure 25 shows the results of tensile tests of round tensile specimens tested in the transverse direction and Figure 26 shows the results of tensile tests of round tensile specimens tested diagonal (45 degrees) to the rolling

direction. In each of the plots shown, average curves are also presented. Lastly for comparison between the tested orientations, the full stress-strain curves for each specimen and averages are shown in Figure 27.

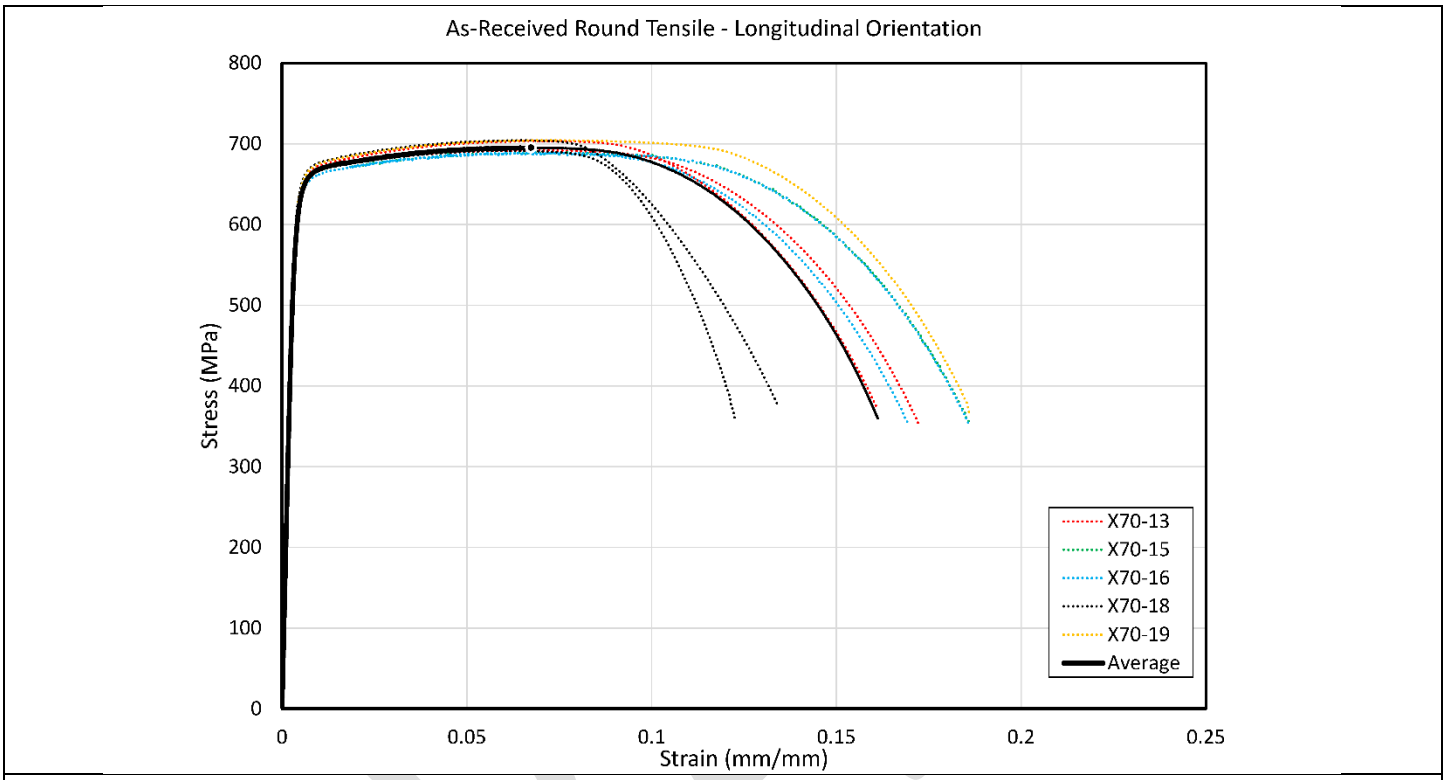

Figure 24. Full stress vs. strain curves from as-received X70 round tensile specimens tested in the longitudinal direction.

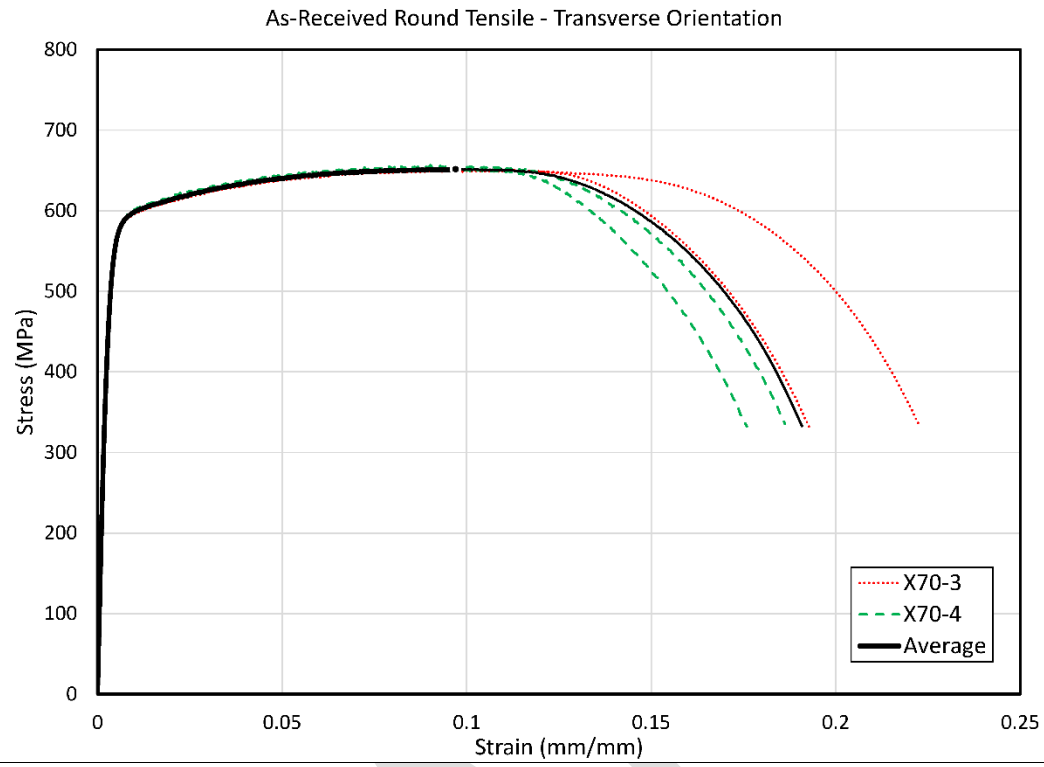

Figure 25. Full stress vs. strain curves from as-received X70 round tensile specimens tested in the transverse direction.

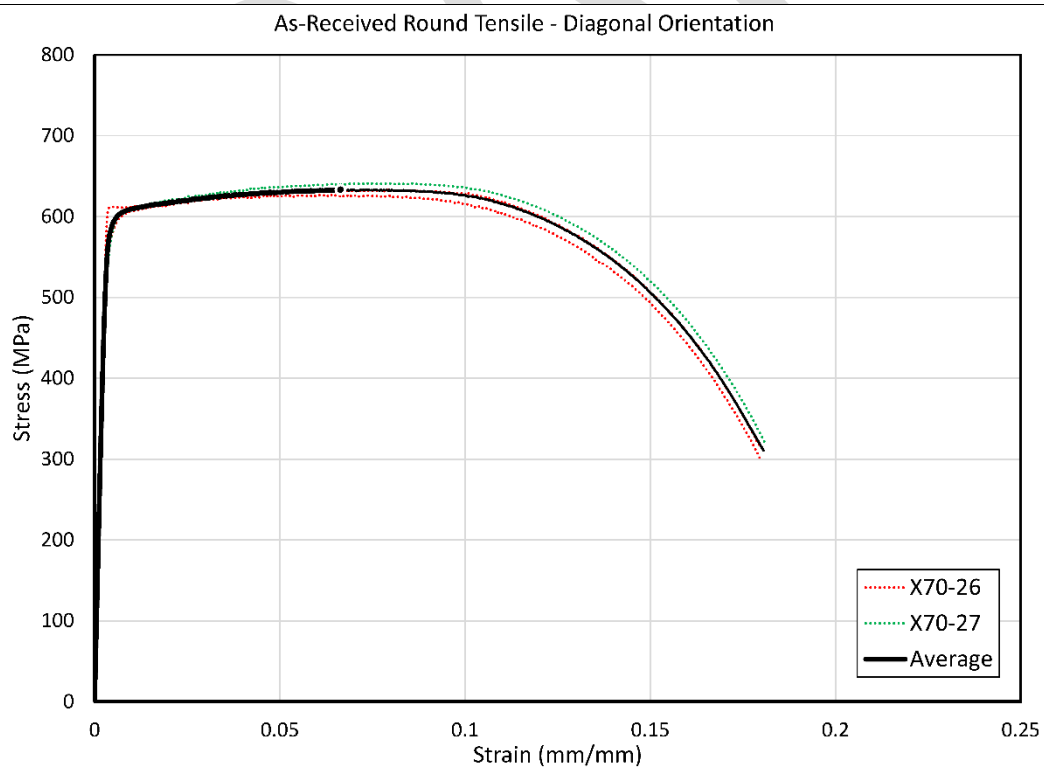

Figure 26. Full stress vs. strain curves from as-received X70 round tensile specimens tested diagonal to the rolling direction.

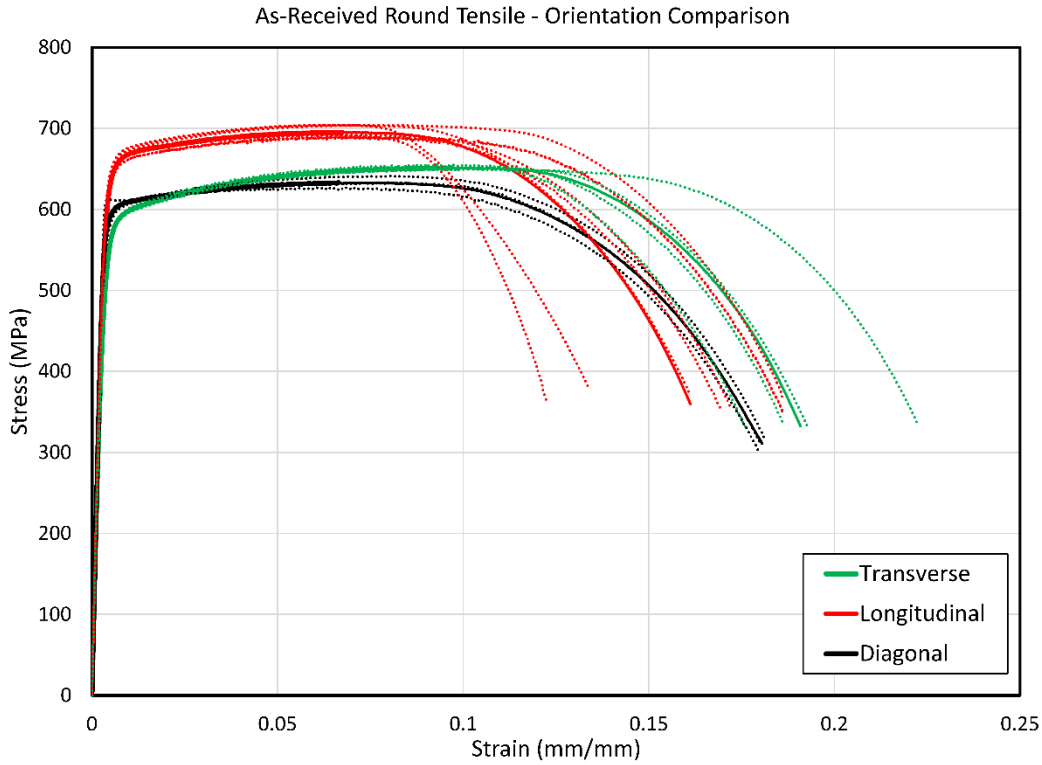

Figure 27. Full stress vs. strain curves from as-received X70 round tensile specimens tested in all orientations for comparison.

Referring to Table 1, specimen X70-18-2 is an alternate specimen which is a reduced gauge-length specimen. It is the same geometry as that used for pre-strained specimens, so it was important to compare the two geometries on as-received material and document the results. The results shown in Figure 28 were anticipated since it is well known that the gauge-length of a specimen influences the non-uniform elongation. The plot shown in Figure 28 also shows the single data points that correspond to the points of maximum stress for each specimen. It is clear that the maximum stresses (see Table 9) of each specimen are very similar, as are the strains at the maximum stresses (see Table 10). The alternate geometry further verified that the gauge-length of the specimen from pre-strained material is expected to have little effect on the shape of the data up to maximum stress, on the maximum stress and on the uniform elongation.

DRAFT

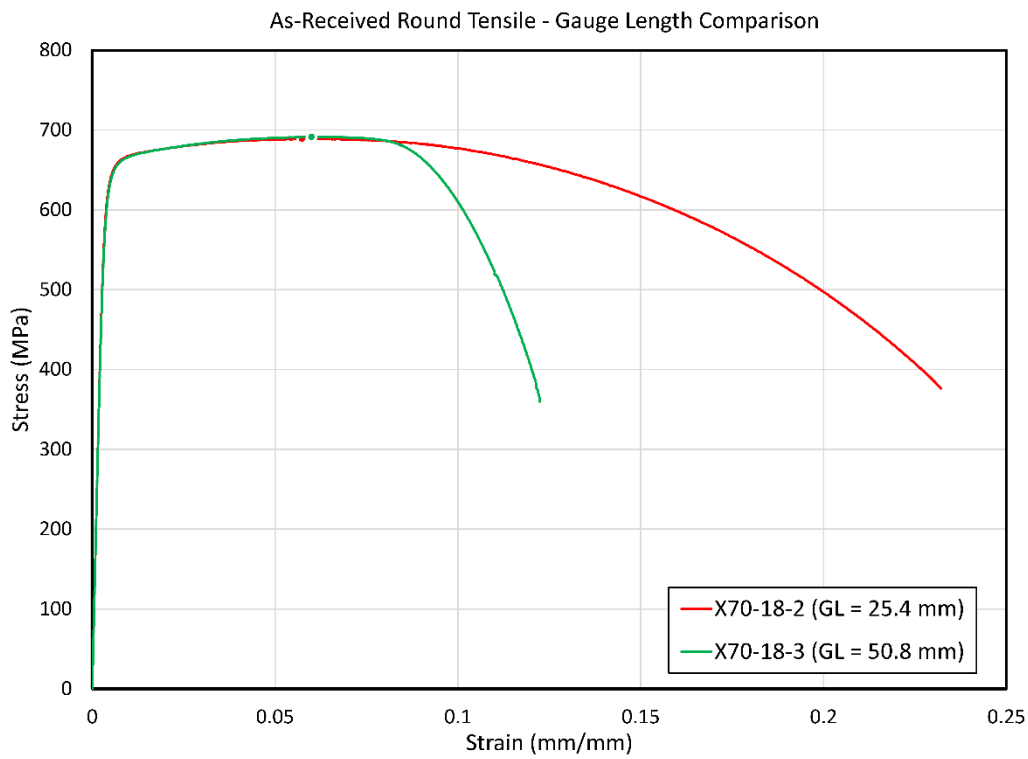

Figure 28. Full stress vs. strain curves from as-received X70 round tensile specimens tested with different gauge lengths. The points of maximum stress for each specimen are also shown.

Analyzing tensile data from in-situ pre-strained specimens is unique in that the initial loading and unloading curves are considered as-received material and should compare to other standard as-received tensile tests. The subsequent loading (and unloading) data are separable from the initial loading and unloading data and can therefore be analyzed and compared to the bulk pre-strained material presented in later sections of the report.

For illustration purposes, the full stress-strain curves for the X70-18-1 and X70-18-2 alternate geometry specimens are shown in Figure 29. This plot is useful to illustrate that in-situ pre-straining and especially unloading and re-loading several times has little effect on the maximum stress or uniform elongation, see specimen X70-18-1. Three additional specimens are also included in this plot. These additional specimens were unloaded and re-loaded only once with different pre-strain levels (see Table 2). From this plot, the material behavior (shape of the data, maximum stress and uniform elongation) is very similar to the as-received material response that is monotonically loaded, see specimen X70-18-2.

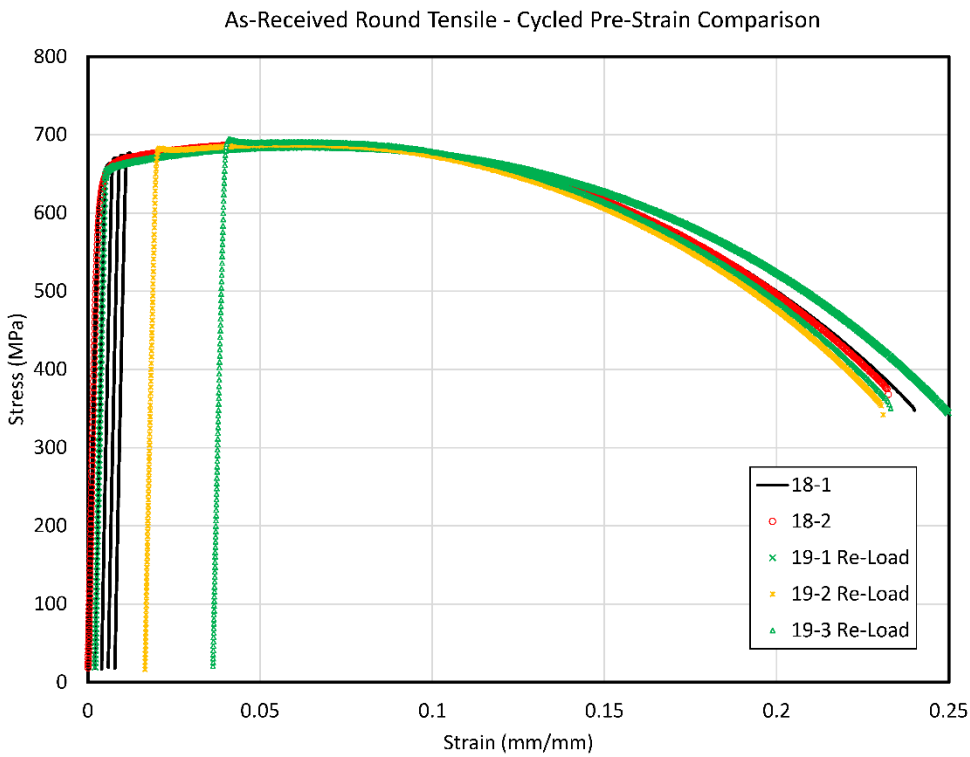

Figure 29. Full stress vs. strain curves from alternate as-received X70 round tensile specimens tested with in-situ pre-straining transverse to the rolling direction.

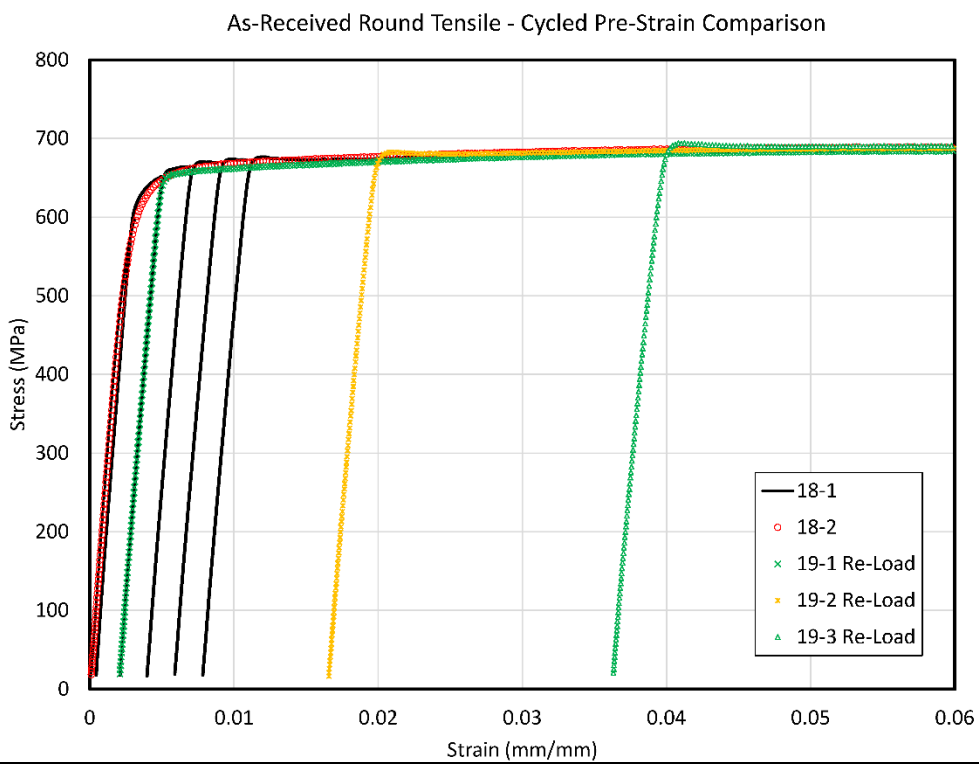

Figure 30. Partial stress vs. strain curves from alternate as-received X70 round tensile specimens tested with in-situ pre-straining transverse to the rolling direction.

As mentioned earlier, the elastic modulus has been associated with material damage but has not been published as more than a phenomenological relationship. However, for the purpose of considering a single, yet complex material undergoing significant strain leading to failure, the change in intrinsic material properties should not be ignored. Most of the published work in this area has focused on fatigue related damage and large-scale plasticity; *i.e.*, sheet metal forming. Modulus changes with increasing amounts of pre-strain is relatively simple to determine using a single specimen approach, but variability increases significantly with multiple specimens. More test data is necessary to reduce the uncertainty of the change with respect to pre-strain levels. Nevertheless, the changes in modulus have been examined with respect to the pre-strain level and are shown in Figure 32.

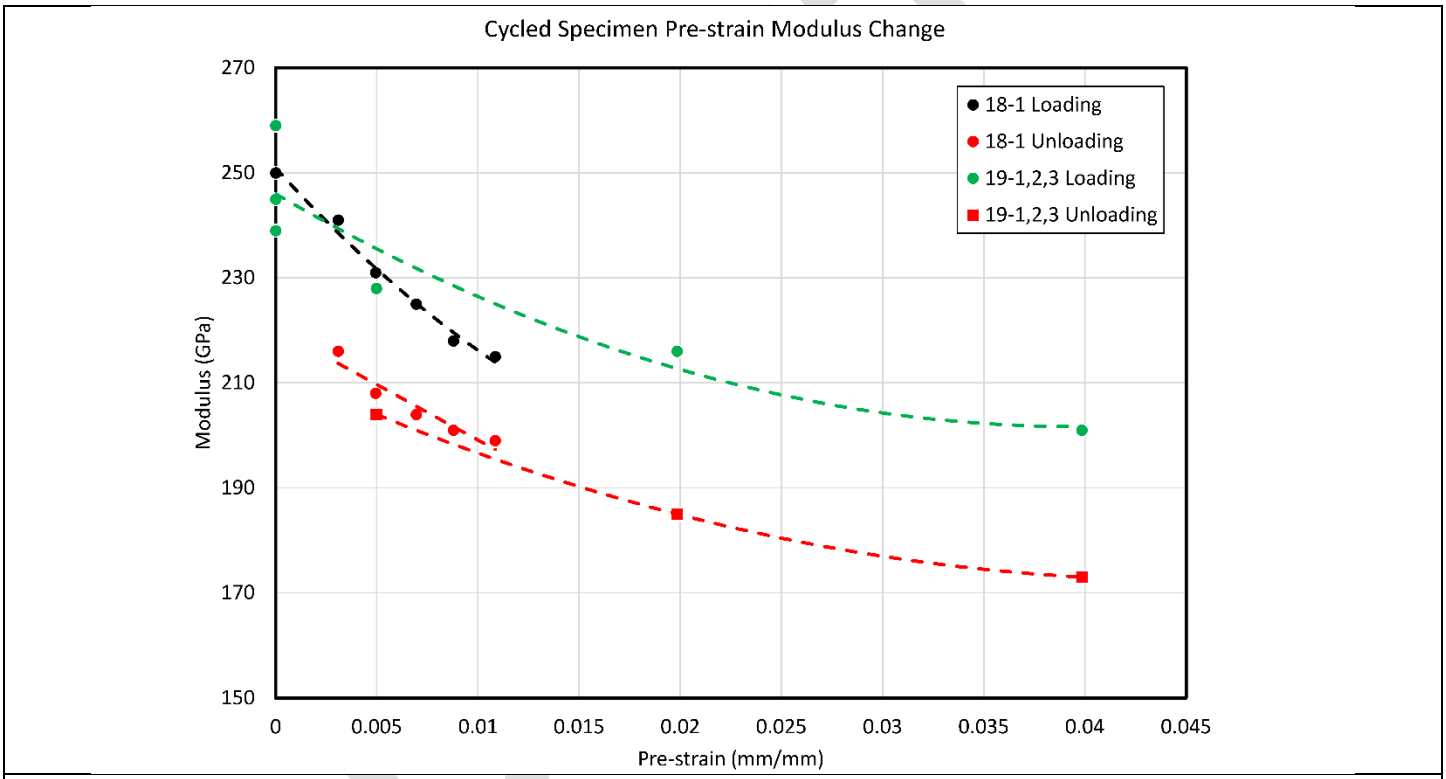

Figure 31. Elastic modulus changes with increasing pre-strain for the in-situ pre-straining method. The data shown include unloading stiffness and re-loading stiffness for the single-specimen method (18-1) and multiple specimen method with 19-1, 19-2 and 19-3. Fit curves are for illustration only.

In order to examine changes in modulus with pre-strain, the strain data were not corrected to 195 GPa like every other test specimen presented in Figure 25 through Figure 28. Since specimen X70-18-2 is presented in both the corrected (Figure 28) and uncorrected state (Figure 29 and Figure 30), it is interesting to examine the effect of the strain shift resulting from the modulus correction. In this case, the original modulus was determined to be 234 GPa. The yield stress is a strain-dependent value since here it is defined as the stress in the specimen

at 0.5 % strain. The yield stress reported in Table 9 is 639 MPa and compares to 648 MPa for the uncorrected data (~1 % difference). The remaining stress values are strain-independent. The data presented in Table 10 for X70-18-2 are then compared since changes are expected. For uncorrected data, the strain at UTS is 0.0566 mm/mm (~1 % difference), and the strain at failure is 0.2309 mm/mm (~1 % difference). The strain energy densities up to yield, maximum stress and to ruptures are as follows: 2.3 J/m^3, 37.3 J/m^3, and 141.36 J/m^3 respectively, resulting in differences of 15 %, 8 % and 9 % respectively. The larger relative differences in strain energy density will be most prominent in specimens with the largest bias in the modulus and should be considered separately from random scatter in the modulus data.

The test matrix for as-received X70 mini-tensile specimens is provided in Table 3. The mini-tensile tests were analyzed to obtain the elastic modulus (E), yield stress defined at 0.5 % strain ($YS_{0.5\,\%}$), strain energy density at yield (U_{YS}), maximum stress (ultimate tensile strength (UTS)) (σ_{UTS}), strain at UTS (ε_{UTS}), strain energy density at UTS (U_{UTS}), stress at failure (σ_f) , strain at failure (ε_f), and the strain energy density at failure (U_f). These data are separated into two tables for easier and more focused comparison. Table 11 presents the elastic modulus and stress values while Table 12 presents the strain and strain energy density data. The tables report the average values, standard deviations and coefficient of variations (CV) for each sample of specimens.

Table 11. As-received X70 Mini-Tensile Results – Comparative Stress Values

Specimen ID	Elastic Modulus (GPa)	Yield Stress at 0.5 % Strain (MPa)	Max Stress (UTS) (MPa)	Failure Stress (MPa)
X70-10-L1	232	599	650	378
X70-10-L2	190	594	660	414
X70-10-L3	154	597	651	365
Average	**192**	**597**	**654**	**386**
Standard Deviation	**39**	**3**	**6**	**25**
CV (%)	**25.6**	**0.4**	**0.8**	**7.0**
X70-10-T1	175	549	644	373
X70-10-T2	132	552	647	384
X70-10-T3	177	544	649	379
Average	**161**	**548**	**647**	**379**
Standard Deviation	**25**	**4**	**3**	**6**
CV (%)	**15.8**	**0.7**	**0.4**	**1.5**
X70-10-TT1	198	517	646	388
X70-10-TT2	141	509	638	396
X70-10-TT3	205	511	644	390
Average	**181**	**512**	**643**	**391**
Standard Deviation	**35**	**4**	**4**	**4**
CV (%)	**19.5**	**0.8**	**0.7**	**1.1**

The elastic moduli were once again calculated for each specimen using ASTM's Standard Practice for Determination of the Slope in the Linear Region of a Test Record. This standard practice provides a procedure for numerically finding the most linear region in a given test record. The practice analyzes residuals and is often more robust than conventional least squares fitting techniques based on a correlation coefficient especially when the underlying physics indicate that the relationship between stress and strain is linear. There were some specimens where this residuals methodology produced a result very different than would be determined from a more pragmatic engineering analysis. By either method, the best practical values of elastic moduli are presented. There is less evidence of bias based on orientation compared to the round tensile results. There is significantly more scatter in the moduli data as shown in Table 11 for the various orientations.

Table 12. As-received X70 Mini-Tensile Results – Comparative Strain and Strain Energy Density Values

Specimen ID	Strain at UTS (mm/mm)	Strain at Failure (mm/mm)	*U* at Yield (J/m^3)	*U* at UTS (J/m^3)	*U* at Failure (J/m^3)
X70-10-L1	0.1068	0.4455	1.9	66.9	258.2
X70-10-L2	0.1001	0.4155	1.8	63.1	245.9
X70-10-L3	0.1029	0.4876	1.9	64.6	282.4
Average	0.1033	0.4495	1.9	64.9	262.2
Standard Deviation	0.0034	0.0362	0.1	1.9	18.6
CV (%)	3.3	7.4	3.2	3.0	6.6
X70-10-T1	0.1145	0.4778	1.7	70.7	276.4
X70-10-T2	0.1131	0.4792	1.7	69.9	279.1
X70-10-T3	0.1076	0.4734	1.7	66.2	275.7
Average	0.1117	0.4768	1.7	68.9	277.1
Standard Deviation	0.0036	0.0030	0.0	2.4	1.8
CV (%)	3.3	0.6	0.0	3.5	0.6
X70-10-TT1	0.0904	0.4025	1.7	55.3	230.0
X70-10-TT2	0.0926	0.3949	1.7	55.9	223.7
X70-10-TT3	0.0849	0.4023	1.6	51.4	229.5
Average	0.0893	0.3999	1.7	54.2	227.7
Standard Deviation	0.0040	0.0043	0.1	2.4	3.5
CV (%)	4.4	1.1	3.5	4.5	1.5

DRAFT

The full stress-strain curves for each specimen are shown in the following figures; Figure 32 shows the results of tensile tests of mini-tensile specimens tested in the longitudinal direction (transvers to the rolling direction), Figure 33 shows the results of tensile tests of mini-tensile specimens tested in the transverse direction and Figure 34 shows the results of tensile tests of mini-tensile specimens tested in the through-thickness direction. In each of the plots shown, average curves are also presented. Lastly, for comparison between the tested orientations, the full stress-strain curves for each specimen and averages are shown in Figure 35.

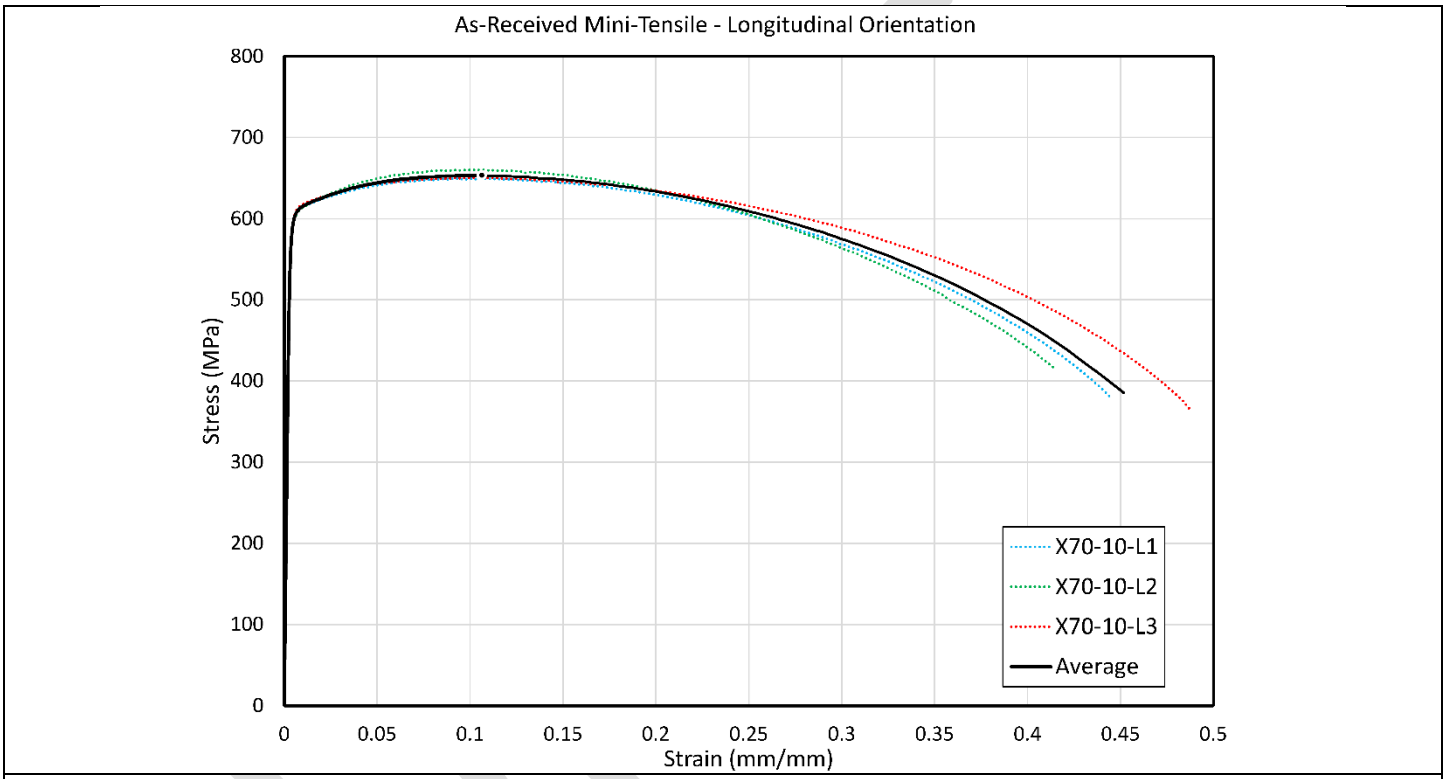

Figure 32. Full stress vs. strain curves from as-received X70 mini-tensile specimens tested in the longitudinal direction.

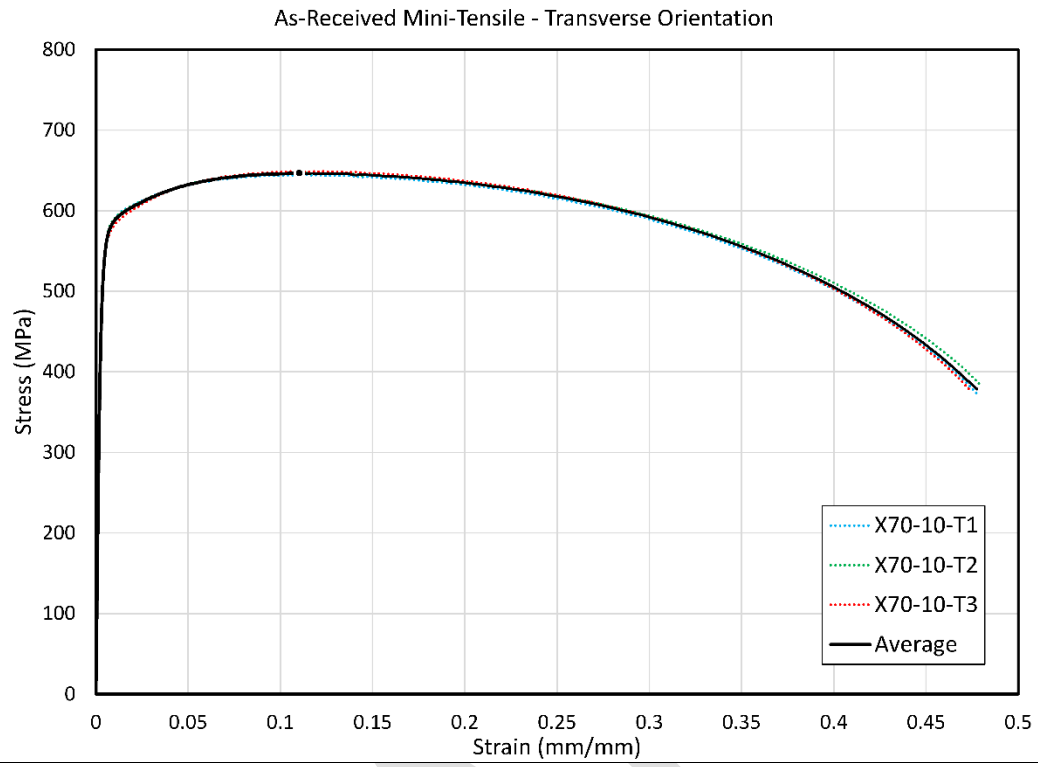

Figure 33. Full stress vs. strain curves from as-received X70 mini-tensile specimens tested in the transverse direction.

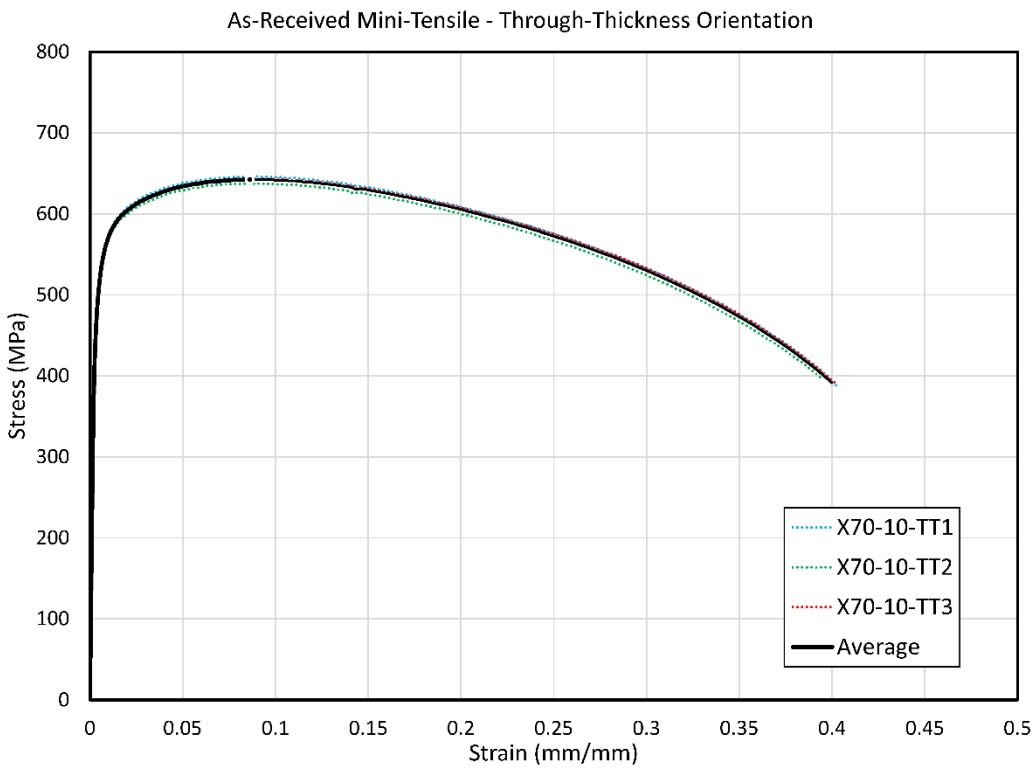

Figure 34. Full stress vs. strain curves from as-received X70 mini-tensile specimens tested in the through-thickness direction.

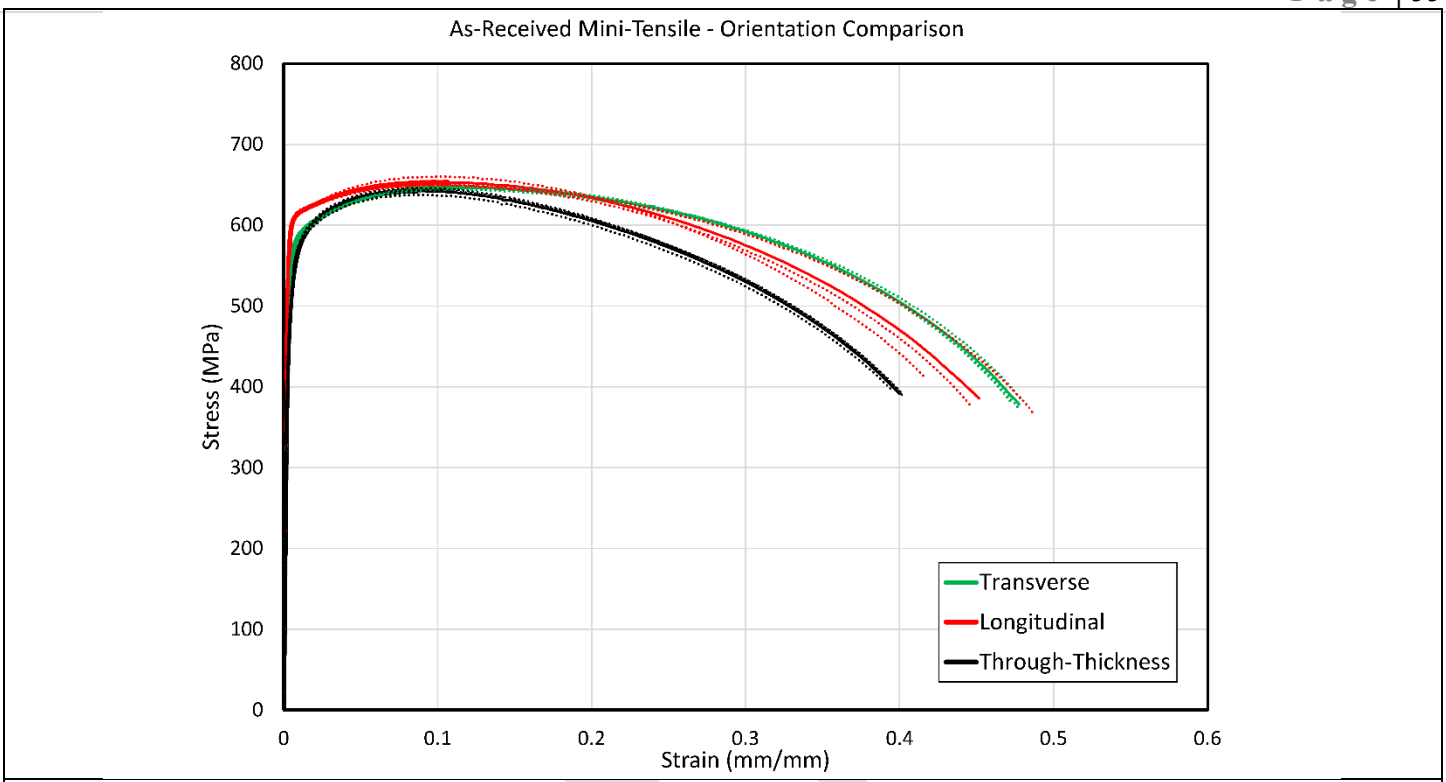

Figure 35. Full stress vs. strain curves from as-received X70 mini-tensile specimens tested in all three orientations.

As stated earlier, separating the intrinsic and geometry sensitive material properties was a goal in examining the round tensile and mini-tensile test results. The first step is to simply examine the full stress-strain curves on the same plot. Figure 36 shows the average stress-strain curves for each specimen geometry and tested orientation. There are two notable data features in Figure 36. Firstly, the average round tensile data from the longitudinal direction had the highest yield and maximum stress while all other geometries and orientations were similar. Secondly the behavior after maximum stress is dominated by geometry and not orientation.

It is expected that obtaining consistent and accurate modulus values from mini-tensile specimens would be more difficult than for round tensile specimens. Two points of emphasis are made here; the instrumentation is more difficult to apply consistently for mini-tensile specimens by virtue of the size of the extensometer, and the extensometer has a lower signal to noise ratio. The result is that larger uncertainties could be expected in strain determined tensile properties.

DRAFT

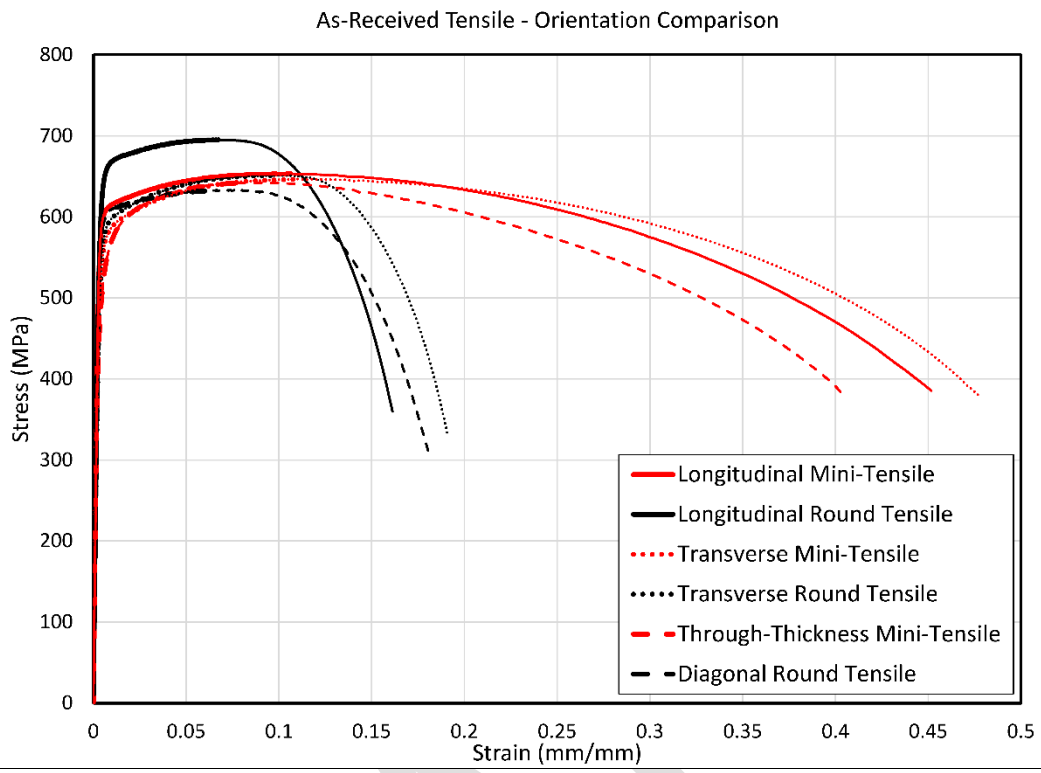

Figure 36. Average full stress vs. strain curves from as-received X70 round and mini-tensile specimens.

Descriptive comparisons of the data shown in Figure 36 is isolated with standard deviations and provided in Figure 37, Figure 38 and Figure 39. While Figure 37 Figure 39 provide readily digestible data, focus here will be applied on Figure 39. Figure 39 shows the strain energy density (in J/m^3) manifesting in the material as a function of material response. The strain energy density to failure, U_f, for the round tensile specimens in the longitudinal orientation, transverse orientation, and diagonal orientation are all within a small range of values. Specifically, the average strain energy density experienced by the round specimens at failure was determined as 107.0 J/m^3 with a standard deviation of 13.6 J/m^3 for all orientations. The strain energy density to failure for the mini-tensile specimens in the longitudinal orientation, transverse orientation, and through-thickness orientation are also all within a small range of values. Specifically, average strain energy density experienced by the mini-tensile specimens at failure was determined as 255.7 J/m^3 with a standard deviation of 23.9 J/m^3 for all orientations.

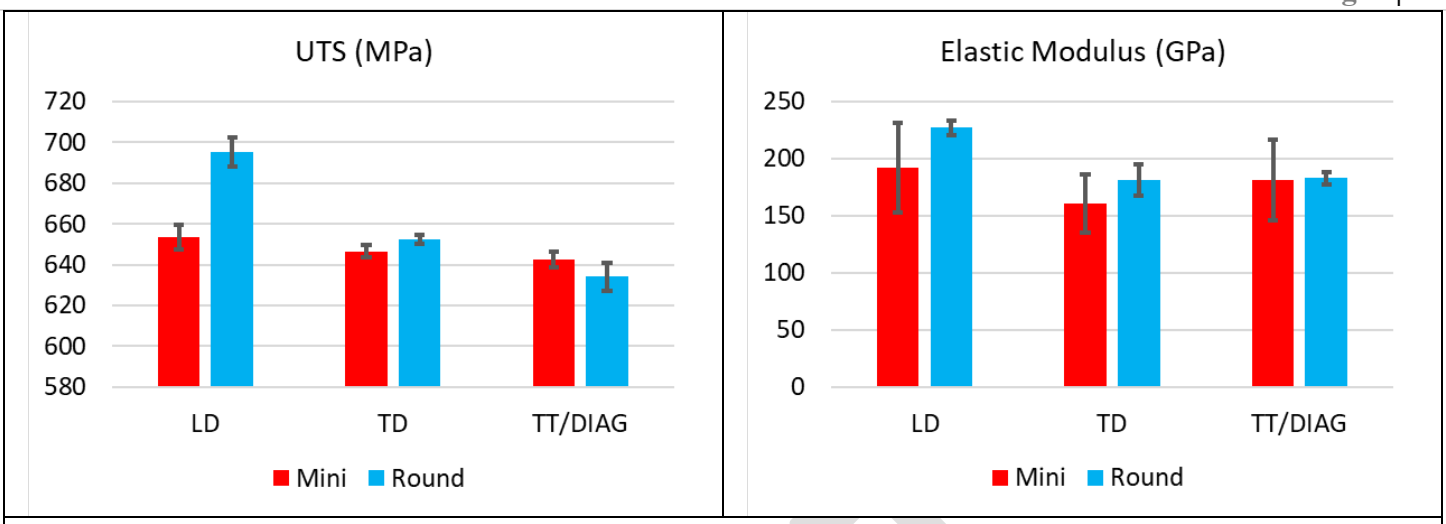

Figure 37. Descriptive ultimate tensile strength (UTS) values (left) and average elastic modulus values (right) for as-received materials tested as both mini-tensile and round tensile specimens.

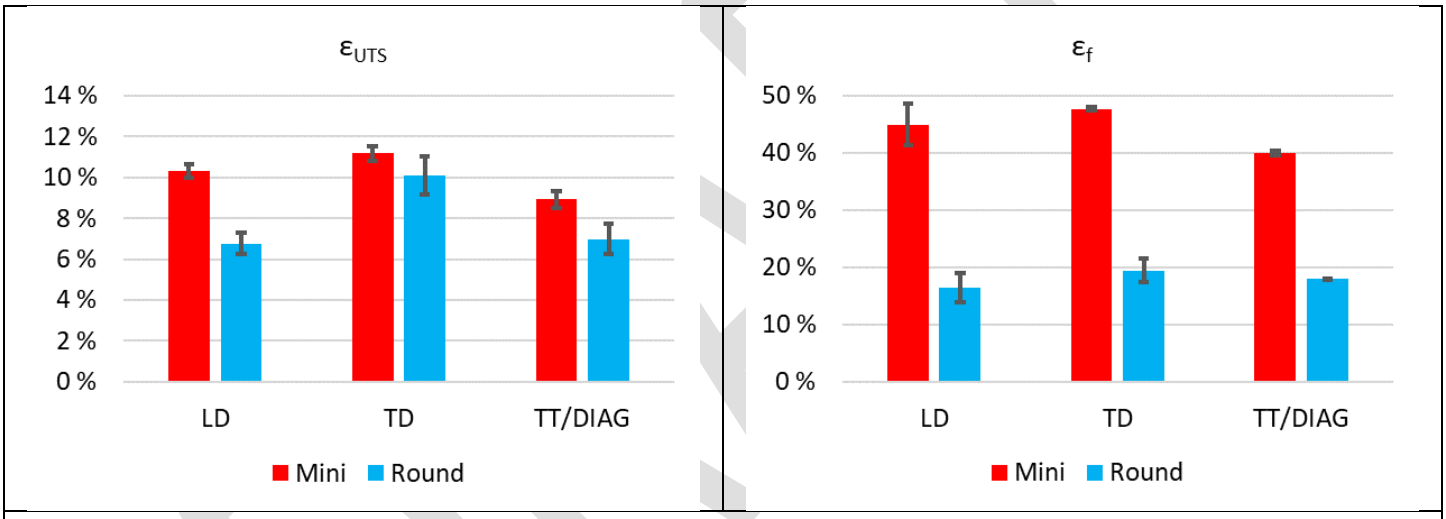

Figure 38. Descriptive average strain to ultimate tensile strength (UTS) values (left) and average strain to failure values (right) for as-received materials tested as both mini-tensile and round tensile specimens.

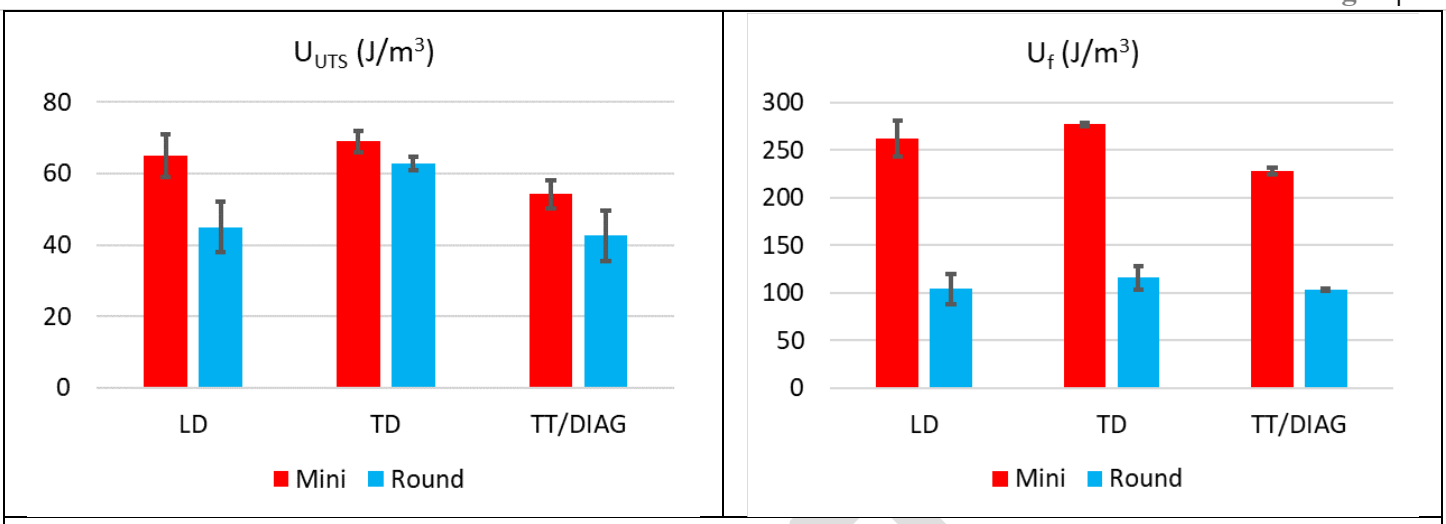

Figure 39. Descriptive average strain energy density to ultimate tensile strength (left) and average strain energy density to failure (right) for as-received materials tested as both mini-tensile and round tensile specimens.

3.3.2.2 Charpy V-Notch Testing – As-Received Material

The Charpy V-Notch results for as-received X70 plate follow in this section. Recall that Charpy V-Notch testing had two objectives; first, determine the ductile-to-brittle transition characteristics of the as-received steel, and second, determine the difference in absorbed energy as a function of the crack path. The results are given numerically in Table 13 and shown graphically in Figure 40. Four specimens were added to the test matrix after the original matrix was tested, these additional specimens are from the same plate as was used for the wide-plate (see Figure 8).

DRAFT

Table 13. As-received X70 Charpy V-Notch Results

Specimen ID	Temperature (˚ C)	Crack Path	Absorbed Energy (J)	Lateral Expansion (mm)	Break Type
X70-6-TT1	21	Through-Thickness*	327.3	2.08	B
X70-6-TT2	-196	Through-Thickness*	3.1	0.02	B
X70-6-TT3	-25	Through-Thickness*	305.2	2.28	B
X70-6-TT4	-50	Through-Thickness*	289.1	2.38	B
X70-6-TT5	-75	Through-Thickness*	265.0	2.39	NB
X70-6-TT6	-100	Through-Thickness*	17.8	0.26	B
X70-6-TT7	-125	Through-Thickness*	9.7	0.10	B
X70-2-L1	20	Longitudinal	440.0	1.96	NB
X70-2-L2	20	Longitudinal	441.7	1.99	NB
X70-2-L3	20	Longitudinal	453.8	2.00	NB
X70-2-L4	20	Longitudinal	444.0	2.05	NB
X70-2-L5	-86	Longitudinal	250.5	2.38	FB
X70-2-L6	-86	Longitudinal	275.3	2.42	B
X70-2-L7	-86	Longitudinal	269.6	2.31	B
X70-7-TT1	22	Through-Thickness*	423.8	1.96	NB
X70-7-TT2	22	Through-Thickness*	430.8	1.99	NB
X70-7-TT3	22	Through-Thickness*	437.7	2.00	NB
X70-7-TT4	22	Through-Thickness*	427.2	2.05	NB
X70-7-TT5	-84	Through-Thickness*	246.1	2.34	NB
X70-7-TT6	-84	Through-Thickness*	246.1	2.34	B
X70-7-TT7	-84	Through-Thickness*	231.0	2.45	B
X70-LD1-1	21	Longitudinal	276.7	1.92	NB
X70-LD1-2	21	Longitudinal	275.1	1.92	NB
X70-LD2-1	21	Longitudinal	217.9	1.56	B
X70-LD2-2	21	Longitudinal	219.1	2.31	B

* Note: The crack path direction was designed to be through-thickness but was verified to be longitudinal.

DRAFT

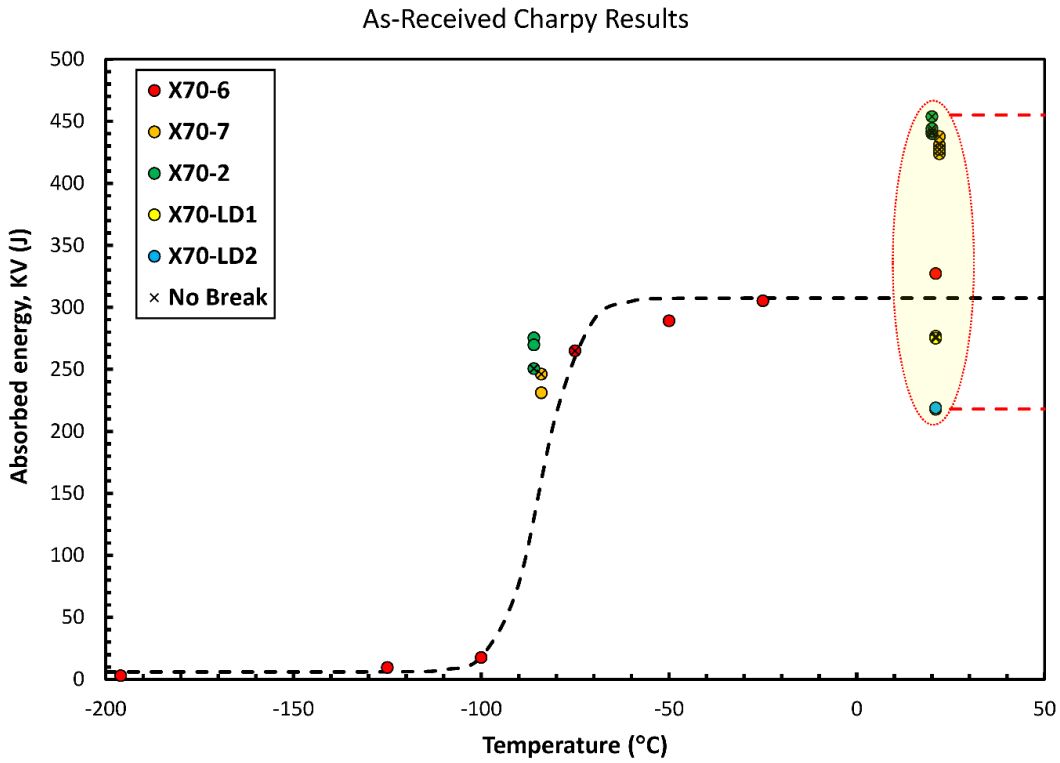

Figure 40. Absorbed Energy vs. Temperature results for as-received X70 plate. The specimens in the X70-6 sample were used to determine the transition curve. Data points from specimens that did not break are noted.

The high percentage of non-broken Charpy specimens is an adequate reason to suspect a problem using as-received Charpy results to predict failure. Another alarming result shown in Figure 40 is the very high absorbed energy at room temperature for samples X70-2 and X70-7. Those samples were supposed to elucidate differences in crack path, yet the differences in absorbed energy are small. It is possible that crack path direction is not a dominant factor in the results however, the large difference between the X70-6 and X70-7 results at room temperature suggest that more investigation is warranted. Referring to Figure 1, the X70-6 and X70-7 blanks are adjacent to each other and oriented the same with respect to the plate rolling direction. The sample and specimen orientations were tracked vary carefully in this project, but the data indicates that an error potentially occurred. To ameliorate the confusion, the suspect specimens were cross-sectioned, and the texture was examined to verify the crack path direction. The texture was examined using electron backscatter diffraction (EBSD) and compared to each other and the original as-received EBSD analysis presented in the physical metallurgy section of the report. There was indeed an error and although it seems unlikely that the machine shop swapped directions on two independent sample sets, the EBSD results suggest that all three sample sets were tested with the crack path aligned with the longitudinal direction. This explains why X70-2 and X70-7 have very similar results but doesn't explain why X70-6 has a significantly lower upper shelf energy. To investigate this further, four additional

specimens were tested. These specimens were taken from the same plate that was machined into the wide-plate. These specimens all had the same crack plane (L-TT) and the same crack path (longitudinal) but resulted in significantly lower absorbed energies at room temperature. While future work will be required to address crack path dependence on absorbed energy, conducting additional Charpy tests on this material is unlikely to bear useful data for modelling, validation or even explanation. The high scatter and inconsistent failure types from Charpy testing on this material is a good justification to look for alternative characterization methods.

3.3.2.3 Tensile Testing – Pre-Strained Material

This section presents the test results on pre-strained material from each of the tests in tabular and graphic formats. Average values and standard deviations are given where appropriate.

The tensile tests were analyzed to obtain the elastic modulus (E), maximum stress (ultimate tensile strength (UTS)) (σ_{UTS}), strain at UTS (ε_{UTS}), strain energy density at UTS (U_{UTS}), stress at failure (σ_f), strain at failure (ε_f), and the strain energy density at failure (U_f). These data are separated into two tables for easier and more focused comparison. Table 14 presents the longitudinal pre-strain values, elastic modulus and stress data while Table 15 presents the longitudinal pre-strain, strain and strain energy density data.

DRAFT

Table 14. Pre-strained X70 Round Tensile Results – Comparative Stress Values

Specimen ID	Pre-Strain (mm/mm)	Elastic Modulus (GPa)	Max Stress (UTS) (MPa)	Failure Stress (MPa)
LD-01	0.0735	199	707	383
LD-03	0.0201	215	696	524
LD-04	0.1093	210	725	379
LD-05	0.1712	171	827	476
LD-07	0.1512	186	817	461
LD-08	0.1227	187	751	387
LD-09	0.1231	175	776	393
LD-11	0.1401	197	793	431
LD-13	0.1595	212	798	403
LD-14	0.0968	199	759	392
LD-15	0.0935	198	764	399
LD-17	0.0974	208	755	476
LD-18	0.1032	209	771	411
LD-19	0.1101	212	772	477
LD-22	0.0669	188	752	421
TD-02	0.0160	241	661	334
TD-04	0.0385	221	680	357
TD-05	0.0848	184	710	362
TD-07	0.1047	240	738	272
TD-08	0.0924	188	730	399
TD-13	0.2088	182	791	396
TD-14	0.1416	215	774	310
TD-15	0.1370	218	766	388
TD-16	0.1140	195	761	398
TD-17	0.1032	198	754	398
TD-19	0.0652	259	723	409
TD-20	0.0600	172	722	377
TD-21	0.0529	190	718	377
TD-25	0.0393	204	701	376

DRAFT

Table 15. Pre-Strained X70 Round Tensile Results – Comparative Strain and Strain Energy Density Values

Specimen ID	Pre-Strain (mm/mm)	Strain at UTS (mm/mm)	Strain at Failure (mm/mm)	*U* at UTS (J/m^3)	*U* at Failure (J/m^3)
LD-01	0.0735	0.0239	0.1821	15.5	110.3
LD-03	0.0201	0.0579	0.1984	38.6	128.9
LD-04	0.1093	0.0140	0.1658	8.7	100.7
LD-05	0.1712	0.0054	0.1244	2.7	79.2
LD-07	0.1512	0.0057	0.1332	2.9	88.7
LD-08	0.1227	0.0052	0.1495	2.4	91.5
LD-09	0.1231	0.0058	0.1867	2.9	120.4
LD-11	0.1401	0.0061	0.1647	3.2	108.4
LD-13	0.1595	0.0060	0.1679	3.1	109.1
LD-14	0.0968	0.0058	0.1715	2.9	108.0
LD-15	0.0935	0.0061	0.1822	3.1	117.0
LD-17	0.0974	0.0054	0.1556	2.6	102.0
LD-18	0.1032	0.0054	0.1609	2.6	102.6
LD-19	0.1101	0.0056	0.1458	2.7	96.1
LD-22	0.0669	0.0054	0.1705	2.6	109.1
TD-02	0.0160	0.0664	0.2647	41.8	155.1
TD-04	0.0385	0.0328	0.2116	20.6	125.0
TD-05	0.0848	0.0165	0.1838	10.1	109.3
TD-07	0.1047	0.0148	0.1751	9.0	105.7
TD-08	0.0924	0.0151	0.1697	9.3	103.9
TD-13	0.2088	0.0145	0.1621	9.5	102.9
TD-14	0.1416	0.0178	0.1726	11.7	110.9
TD-15	0.1370	0.0164	0.1717	10.5	107.3
TD-16	0.1140	0.0173	0.1792	11.3	113.3
TD-17	0.1032	0.0166	0.1789	10.6	112.6
TD-19	0.0652	0.0196	0.1899	12.2	118.6
TD-20	0.0600	0.0197	0.2002	12.6	123.5
TD-21	0.0529	0.0204	0.1904	12.9	116.3
TD-25	0.0393	0.0278	0.1915	17.8	115.6

The full stress-strain curves for each specimen are shown in the following figures; Figure 41 shows the results of tensile tests of round tensile specimens tested in the longitudinal direction, Figure 42 shows the results of tensile tests of round tensile specimens tested in the transverse direction.

DRAFT

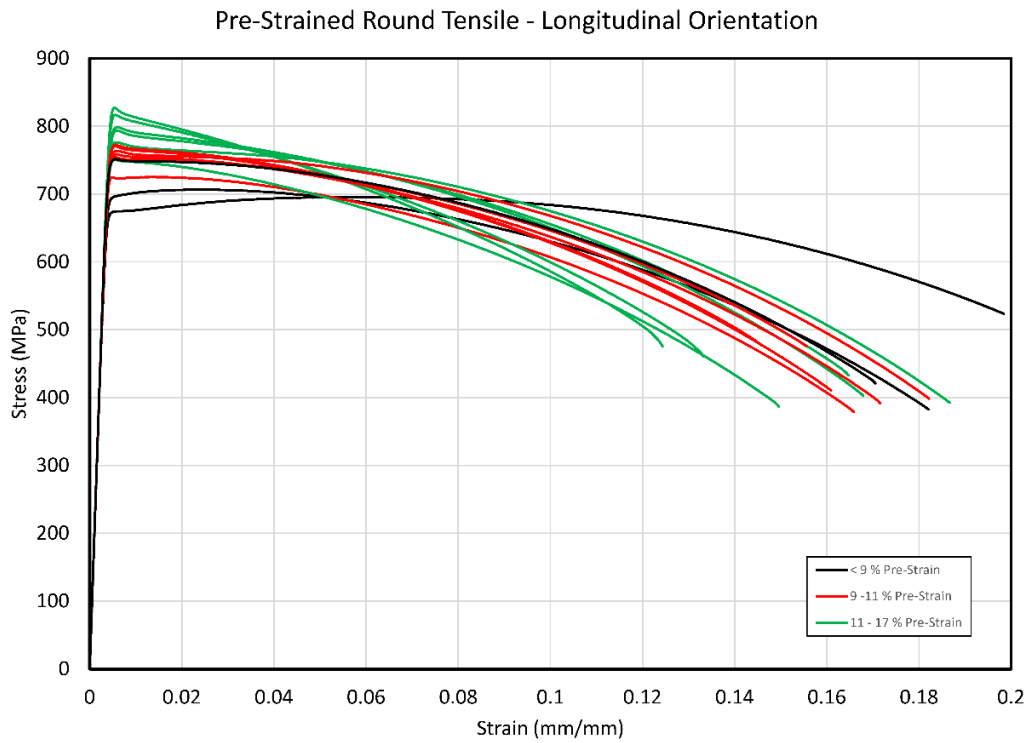

Figure 41. Full stress vs. strain curves from bulk pre-strained X70 round tensile specimens tested in the longitudinal direction.

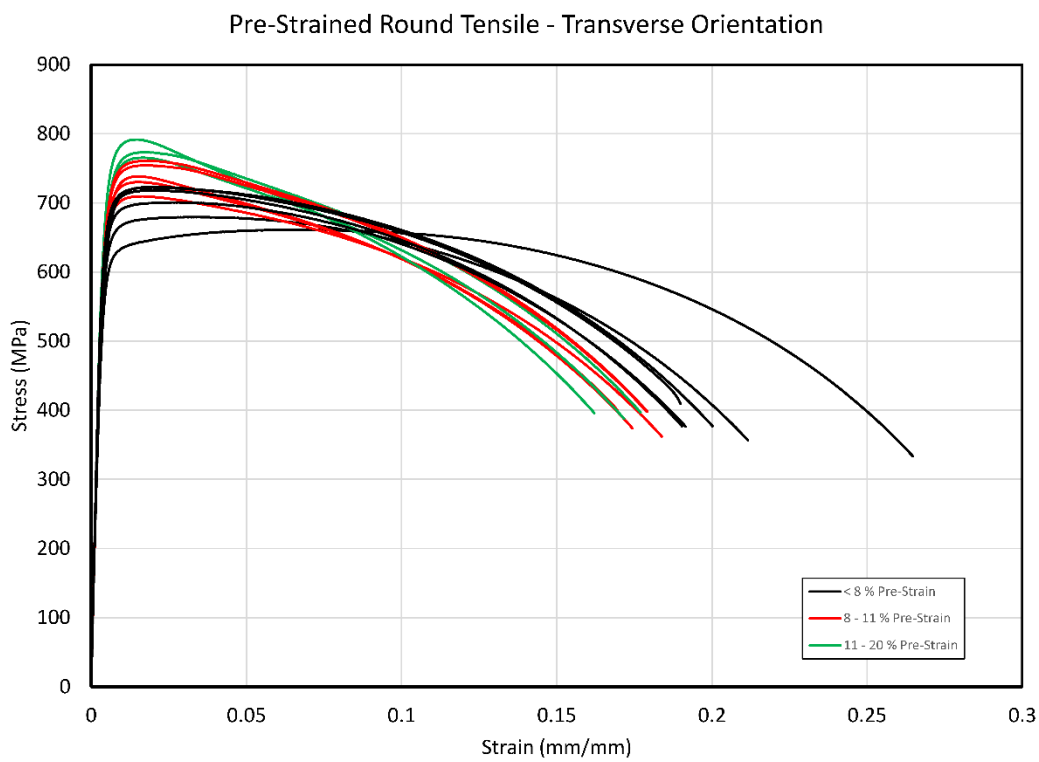

Figure 42. Full stress vs. strain curves from bulk pre-strained X70 round tensile specimens tested in the transverse direction.

There is a significant difference between tensile results obtained from bulk pre-strained material and in-situ specimen pre-straining. Recall that the in-situ pre-straining method showed that increasing pre-strain changed the modulus but did not significantly change the other characteristics of the tensile record (see Figure 29 and Figure 30). This is not the case for bulk pre-strained material where there is a significant increase in the maximum stress with increasing pre-strain, as shown in Figure 43 (see also Figure 41). This comparison illustrates that in-situ pre-straining and bulk pre-straining produce material strain states that cannot be directly compared. This project does not endeavor to determine the best way to compare them, instead the in-situ pre-straining method was done to simply validate the hypothesis that it was not an appropriate method to develop the material strain state that best represents the conditions in a wide-plate, and similarly the strain conditions in an unstable high-rate ductile failure.

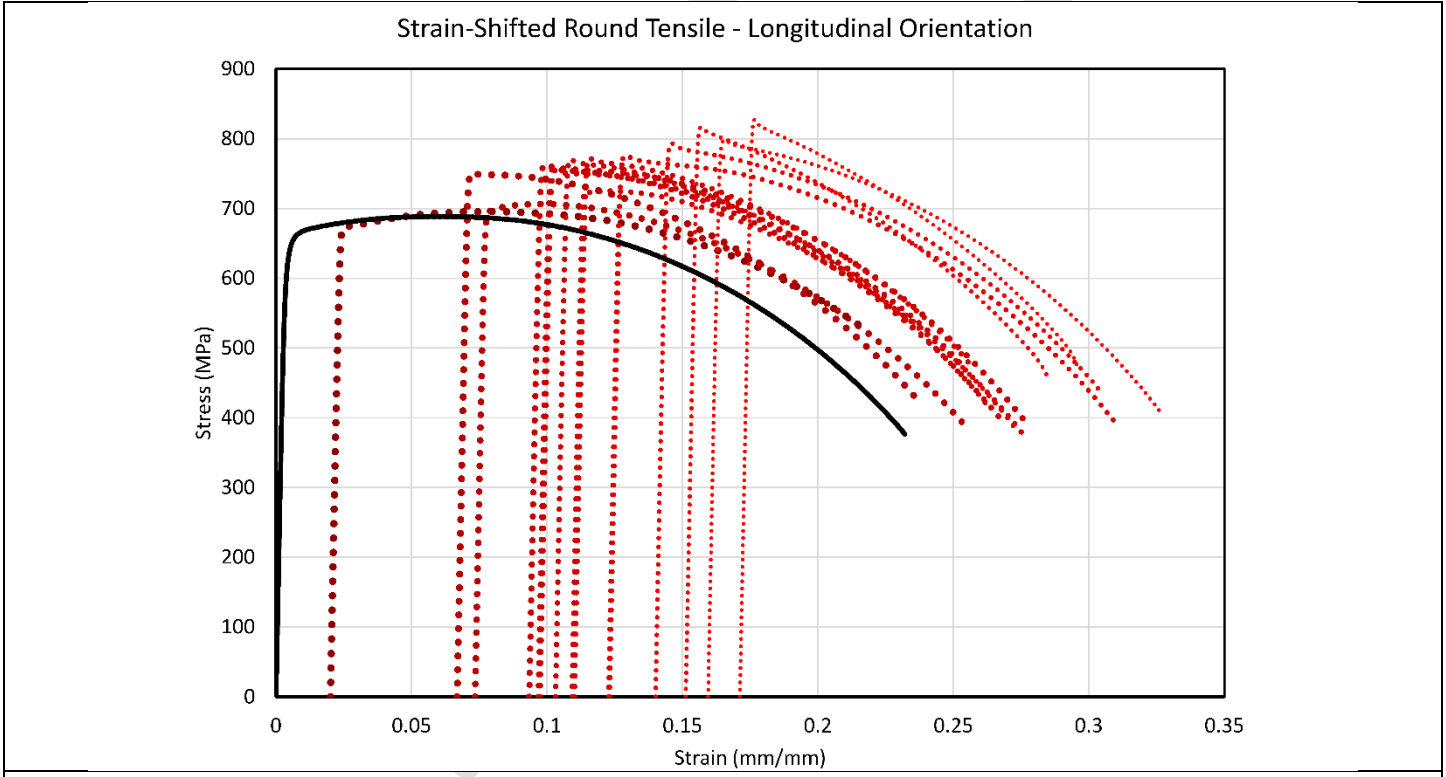

Figure 43. Full stress vs. strain curves from bulk pre-strained X70 round tensile specimens tested in the longitudinal direction – the strain shift corresponds to the bulk pre-strain for the specimen blank. The tensile data for an as-received specimen (X70-18-2) is also shown.

Regardless of pre-straining method, the modulus is expected to change with increasing amounts of pre-strain (see Figure 31 for in-situ pre-straining), however the change in elastic modulus of bulk pre-strained specimens is relatively small comparatively and because of the high scatter it is difficult to define an adequately correlated trend useful for predictions (Figure 44). In contrast, the maximum stress plotted against the longitudinal engineering pre-strain for all bulk pre-strained round tensile specimens is shown in Figure 45 and shows a more distinct and better correlated relationship. The point illustrated here is that, in general, an increase in pre-strain increases the strength of the local material. Furthermore, the "toughness", or the total cumulative strain energy density up to failure also increases with increasing pre-strain.

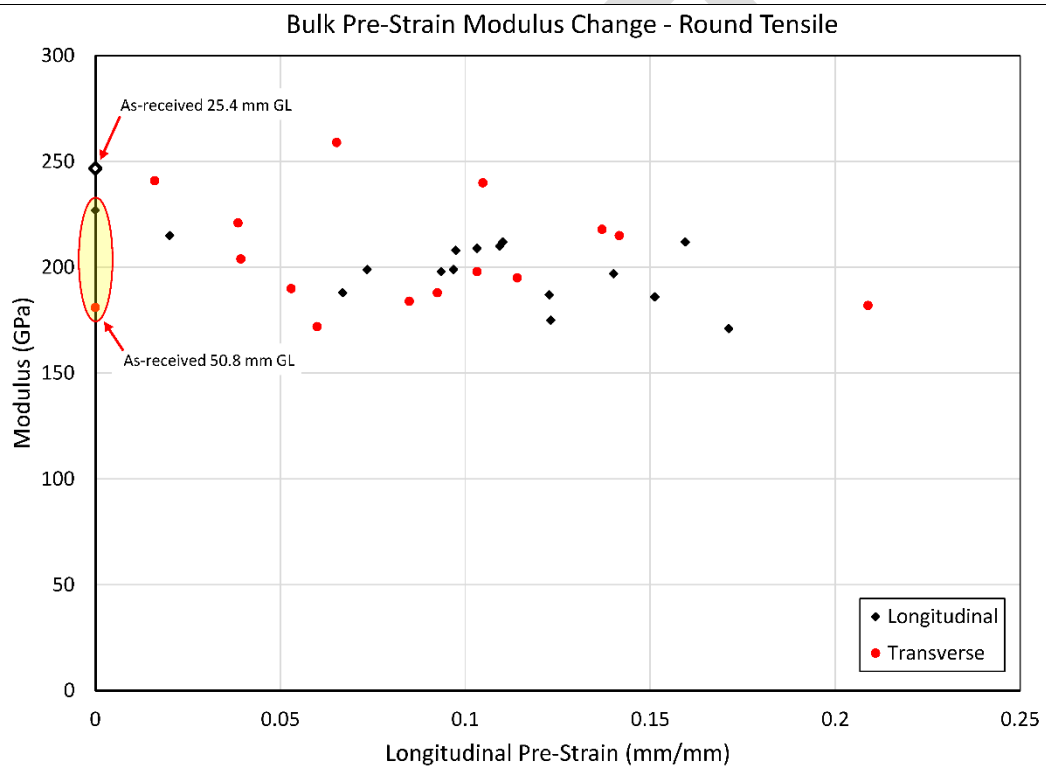

Figure 44. Elastic modulus of bulk pre-strained X70 as a function of the longitudinal engineering pre-strain in the specimen blank taken from the wide-plate.

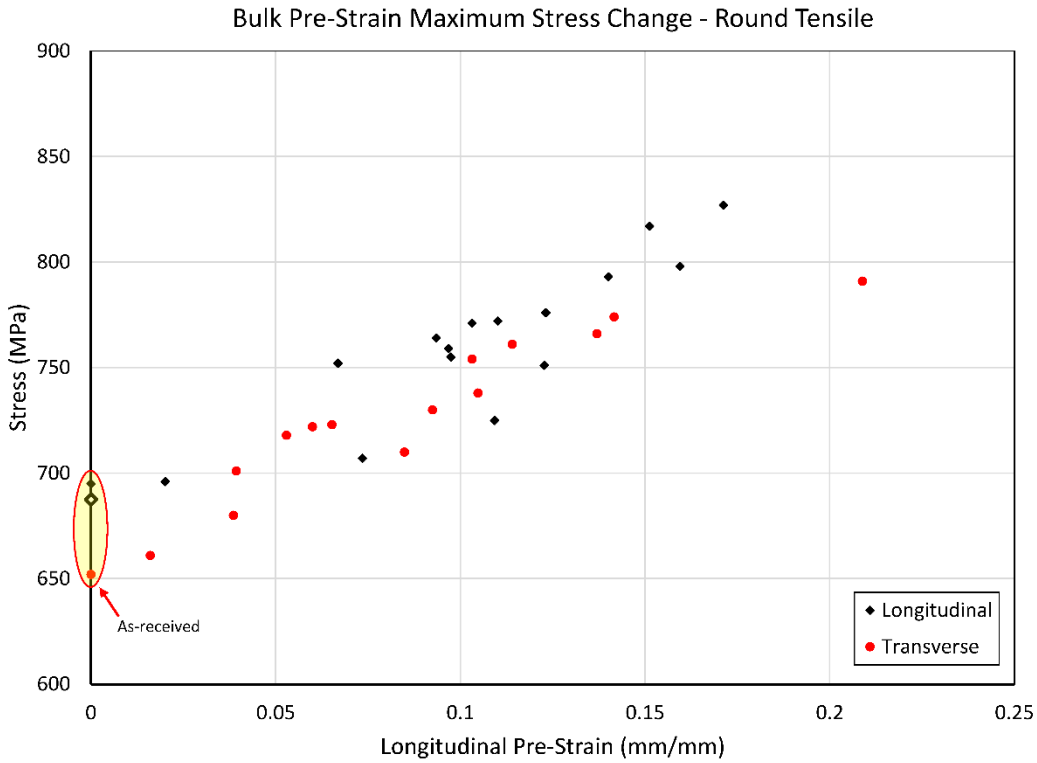

Figure 45. Maximum stress of bulk pre-strained X70 round tensile specimens as a function of the longitudinal engineering pre-strain in the specimen blank taken from the wide-plate. The as-received data shown includes specimens with a 2.5 in (63.5 mm) reduced cross-section length as well as the 1.125 in (28.6 mm) reduced cross-section length (open diamond).

The strain energy density associated with the pre-strain, U_{PS}, experienced by each specimen was calculated. The strain energy density at failure, U_f, of the pre-strained specimens was also calculated independent of that associated with the pre-strain event. The strain energy density is independent of reference frame, therefore the total cumulative strain energy density for pre-strained specimens, U_T, is simply the sum of the strain energy density resulting from the pre-straining event and the strain energy density resulting from the tensile failure, regardless of orientation.

Figure 46 provides the total cumulative strain energy density experienced by each specimen versus the longitudinal pre-strain associated with each specimen. The total cumulative strain energy density for as-received (longitudinal, transverse and diagonal) specimens is shown for reference, where U_{PS} is assumed to be equal to zero for as-received specimens.

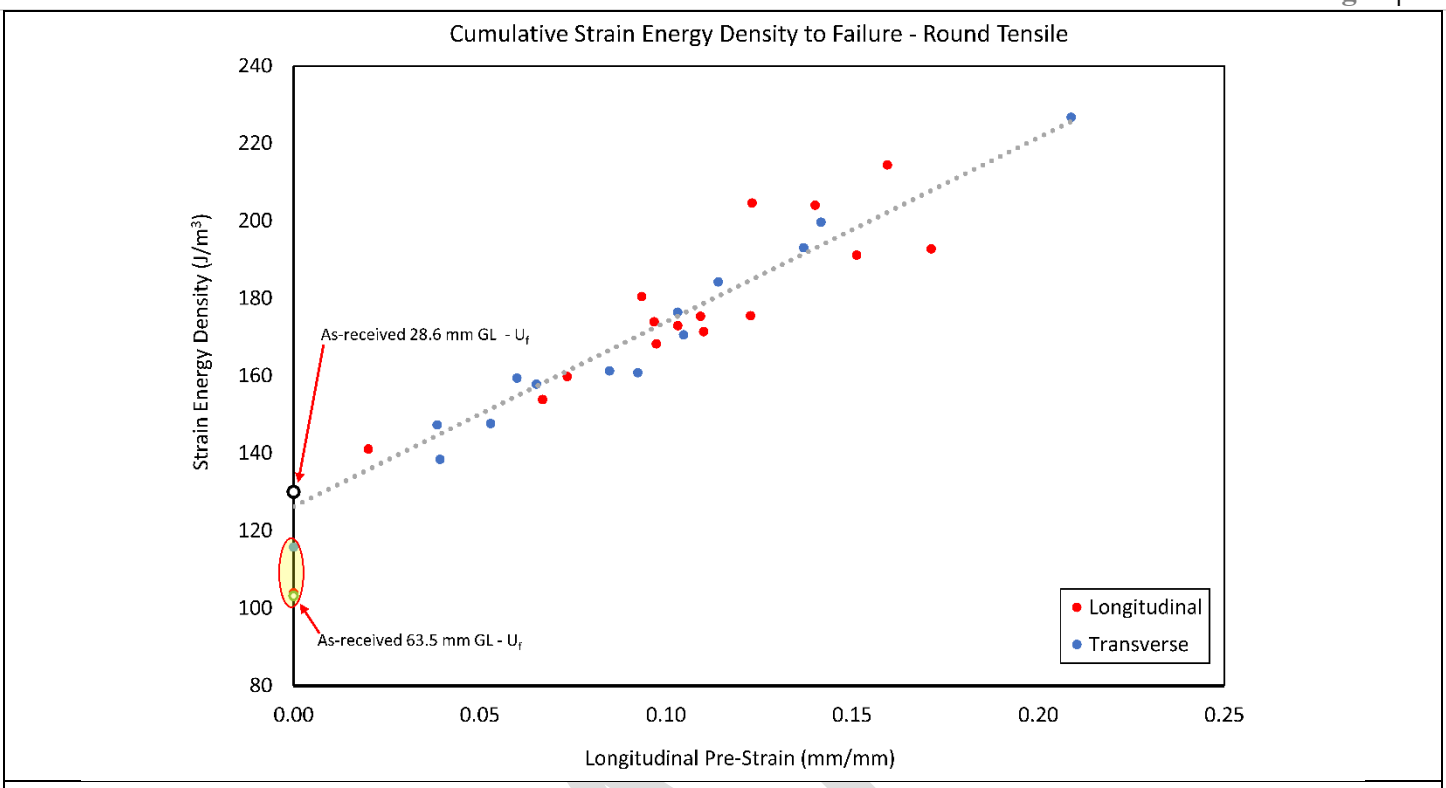

Figure 46. Cumulative strain energy density to failure for pre-strained round tensile specimens tested in longitudinal and transverse orientations.

Note that in Figure 46, that the total cumulative strain energy density to failure for the longitudinally-oriented pre-strained specimens and the transversely-oriented pre-strained specimens all follow a single linear trend with a relatively high correlation coefficient. The trend created by the data indicates that pre-straining a specimen plastically by any amount "toughens" the material and is indicated by an increasing strain energy density required to fail the material. The as-received round tensile specimens with a reduced section length of 63.5 mm (2.5 in) exhibited an average strain energy density to failure of 107.0 J/m^3, while the intercept of the pre-strained data in Figure 46 indicates that the minimum amount of strain energy density required to fail the material is 126.3 J/m^3. This difference is most likely attributed to residual strains in the tensile specimen creating a slight bias.

The strain energy density required to fail a pre-strained, specimen versus the pre-strain magnitude is provided in Figure 47. Once again, the as-received strain energy density at failure is provided as a reference.

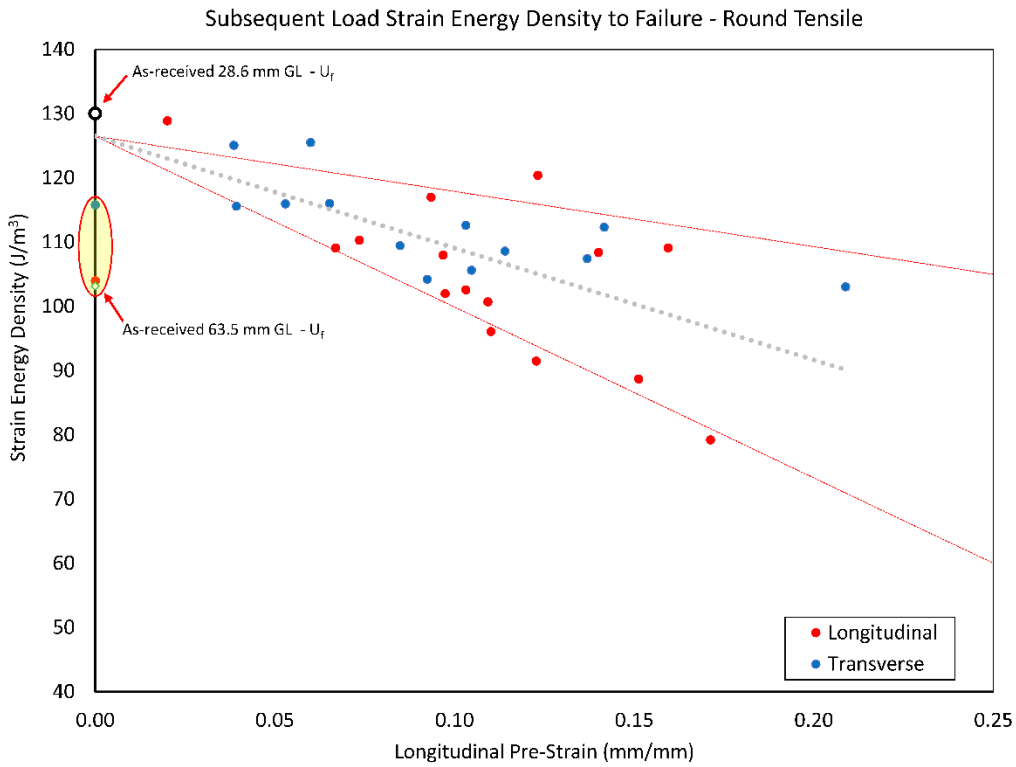

Figure 47. Strain energy density to failure for bulk pre-strained X70 round tensile specimens tested in longitudinal and transverse orientations. Data is provided for final load incursion only and does not include strain energy density accumulated during pre-straining.

The data shown in Figure 47 indicate that the strain energy density required to fail the material once it has been pre-strained decreases as a function of increasing pre-strain magnitude. Fitting a single linear trend to the longitudinal and transverse data indicates that the minimum amount of strain-energy required to fail the material once the material has been pre-strained is 126.5 J/m^3. The strain energy density at failure for as-received (longitudinal, transverse and diagonal) specimens is shown for reference. Given the repeatability of the estimated strain energy density required to fail a pre-strained component, and the fact that this represents a physical manifestation of damage accumulation, it is postulated that the appropriate error bands associated with the statistical nature of crystalline material failure would be represented as non-parallel lines emanating from the estimated minimal value of 126.5 J/m^3.

The mini-tensile tests were analyzed to obtain the elastic modulus (E), yield stress defined at 0.5 % strain ($YS_{0.5\ \%}$), strain energy density at yield (U_{YS}), maximum stress (ultimate tensile strength (UTS)) (σ_{UTS}), strain at UTS (ε_{UTS}), strain energy density at UTS (U_{UTS}), stress at failure (σ_f) , strain at failure (ε_f), and the strain energy density at failure (Uf). These data are separated into two tables for easier and more focused comparison. Table 16 presents the elastic modulus and stress values and Table 17 presents the strain and strain energy density data. The

tables report the average values for each sample (4 specimens), as well as the standard deviations, but are not averaged together as was done for as-received data because the pre-strain values are all different.

Table 16. Pre-strained X70 Mini-Tensile Results – Comparative Average Stress Values

Sample ID	Pre-Strain (mm/mm)	Elastic Modulus (GPa)		Max Stress (UTS) (MPa)		Failure Stress (MPa)	
		AVG	STDEV	**AVG**	STDEV	**AVG**	STDEV
LD-02	0.0703	**199**	42	**732**	4	**440**	12
LD-06	0.0767	**206**	25	**689**	4	**422**	5
LD-16	0.0974	**212**	40	**733**	7	**447**	4
LD-20	0.0971	**186**	28	**748**	3	**446**	12
LD-21	0.0664	**184**	3	**729**	7	**436**	5
LD-23	0.0669	**166**	3	**693**	3	**411**	5
TD-03	0.0570	**177**	8	**669**	5	**390**	5
TD-06	0.0573	**176**	4	**691**	3	**399**	10
TD-10	0.1439	**170**	6	**730**	17	**428**	18
TD-11	0.2052	**167**	18	**775**	7	**440**	16
TD-18	0.0728	**173**	4	**698**	8	**404**	7
TD-22	0.0460	**178**	5	**684**	8	**403**	8
TD-23	0.0415	**166**	20	**676**	3	**405**	6
TD-24	0.0263	**165**	13	**662**	2	**403**	9
TT-02	0.0703	**199**	23	**686**	5	**434**	27
TT-06	0.0767	**198**	13	**675**	4	**401**	7
TT-16	0.0974	**226**	20	**724**	1	**423**	10
TT-20	0.0971	**164**	7	**729**	3	**441**	9
TT-21	0.0664	**169**	5	**702**	3	**418**	5
TT-23	0.0669	**166**	3	**693**	3	**411**	5

DRAFT

Table 17. Pre-strained X70 Mini-Tensile Results – Comparative Average Strain and Average Strain Energy Density Values

Sample ID	Pre-Strain (mm/mm)	Strain at UTS (mm/mm)		Strain at Failure (mm/mm)		U at UTS (J/m3)		U at Failure (J/m3)	
		AVG	STDEV	**AVG**	STDEV	**AVG**	STDEV	**AVG**	STDEV
LD-02	0.0703	**0.0067**	0.0007	**0.3112**	0.0312	**3.2**	0.6	**187.1**	10.5
LD-06	0.0767	**0.0366**	0.0064	**0.3682**	0.0125	**23.6**	4.2	**224.1**	8.6
LD-16	0.0974	**0.0063**	0.0006	**0.3537**	0.0118	**2.8**	0.6	**224.9**	6.3
LD-20	0.0971	**0.0069**	0.0007	**0.343**	0.0221	**3.5**	0.5	**220.3**	13.8
LD-21	0.0664	**0.0064**	0.0007	**0.3644**	0.015	**3.2**	0.5	**231.3**	10.4
LD-23	0.0669	**0.0234**	0.0025	**0.3207**	0.0025	**14.3**	1.8	**191.0**	2.1
TD-03	0.0570	**0.0246**	0.0083	**0.38**	0.0044	**14.9**	5.5	**222.2**	2.4
TD-06	0.0573	**0.0173**	0.0006	**0.3415**	0.0181	**10.3**	0.4	**202.4**	10.7
TD-10	0.1439	**0.0191**	0.0016	**0.3082**	0.0393	**12.1**	1.4	**190.0**	27.1
TD-11	0.2052	**0.0176**	0.0014	**0.3049**	0.0144	**11.6**	1.1	**195.3**	7.9
TD-18	0.0728	**0.0202**	0.0026	**0.3604**	0.007	**12.5**	1.9	**216.5**	2.3
TD-22	0.0460	**0.0278**	0.0105	**0.3862**	0.0073	**17.4**	7.2	**231.9**	2.2
TD-23	0.0415	**0.0538**	0.0060	**0.3981**	0.0085	**34.6**	3.8	**239.3**	5.2
TD-24	0.0263	**0.0834**	0.0307	**0.4259**	0.0079	**53.1**	20.2	**253.7**	4.5
TT-02	0.0703	**0.0232**	0.0012	**0.3187**	0.0144	**14.0**	0.9	**188.0**	9.2
TT-06	0.0767	**0.0267**	0.0017	**0.3556**	0.0024	**16.2**	1.1	**207.4**	2.5
TT-16	0.0974	**0.0227**	0.0013	**0.3277**	0.0117	**14.4**	0.8	**196.2**	15.2
TT-20	0.0971	**0.019**	0.0003	**0.286**	0.0079	**11.9**	0.3	**174.9**	5.2
TT-21	0.0664	**0.0226**	0.0026	**0.342**	0.0048	**14.0**	1.8	**206.5**	3.8
TT-23	0.0669	**0.0234**	0.0025	**0.3207**	0.0025	**14.3**	1.8	**191.0**	2.1

The full average stress-strain curves for each sample are shown in Figure 48. The curves are unremarkable and were expected based on previous testing. A comparison of bulk pre-strained round tensile results and bulk pre-strained mini-tensile results tested in the longitudinal orientation is shown in Figure 49. Similarly, a comparison of bulk pre-strained round tensile results and bulk pre-strained mini-tensile results tested in the transverse orientation is shown in Figure 50.

DRAFT

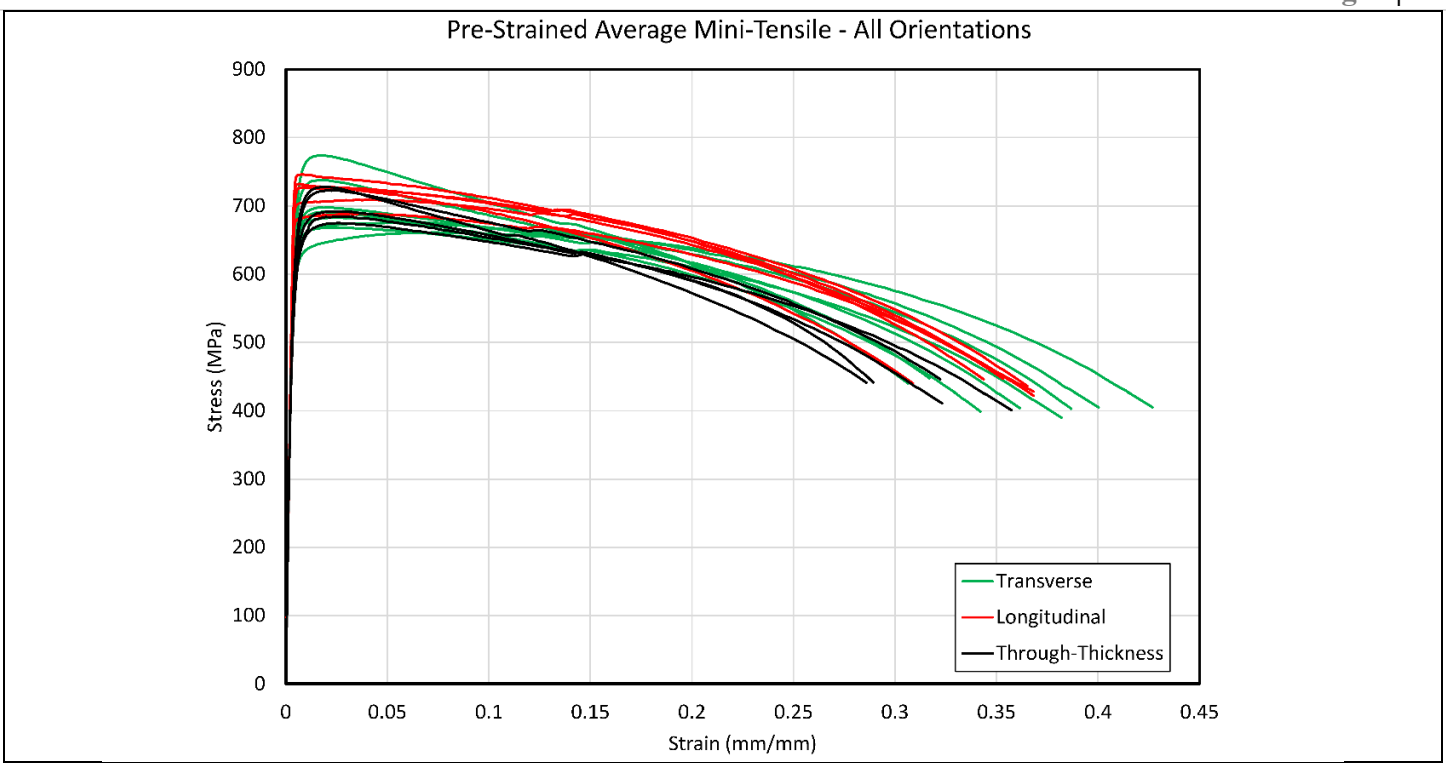

Figure 48. Full average stress vs. strain curves from bulk pre-strained X70 mini-tensile samples tested in the longitudinal, transverse and through-thickness directions.

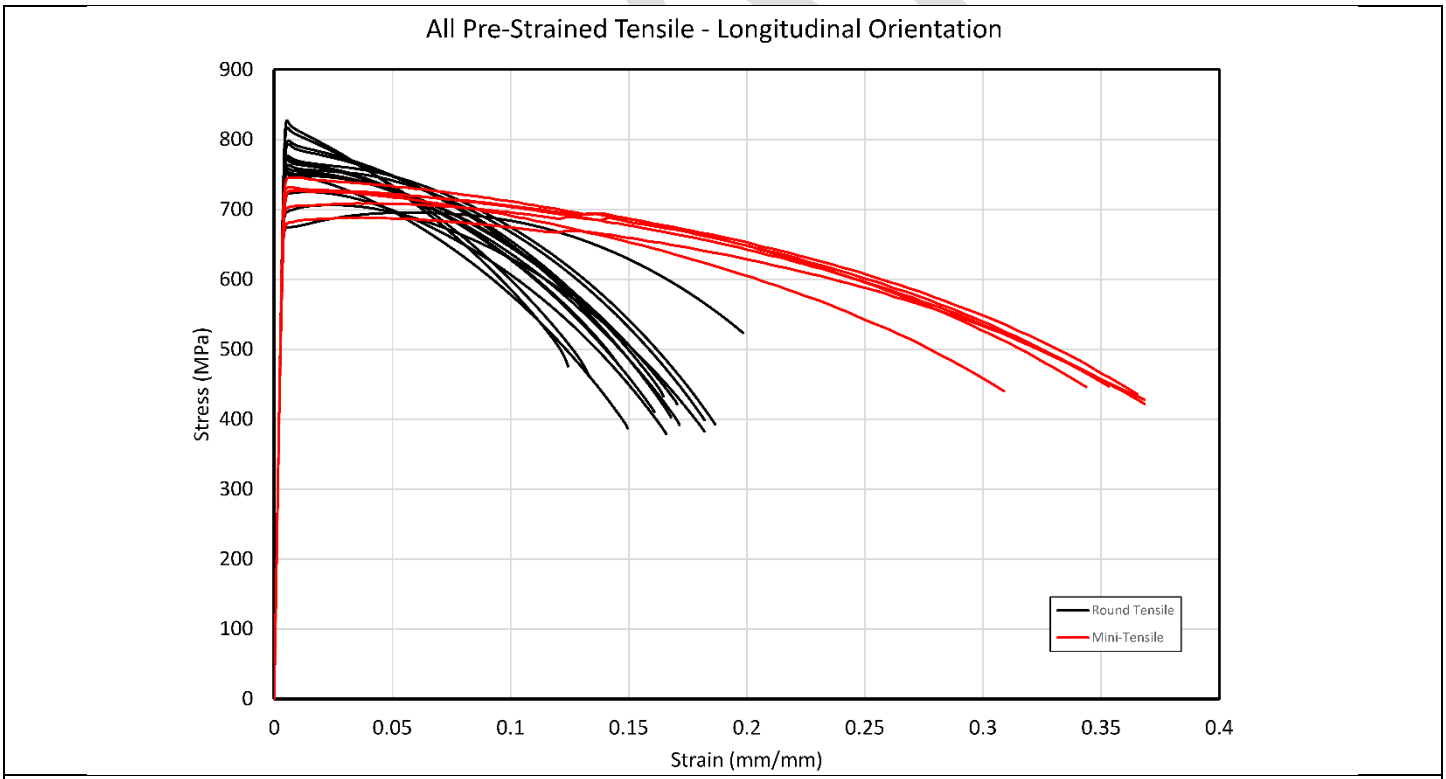

Figure 49. Full stress vs. strain curves from bulk pre-strained X70 round tensile specimens tested in the longitudinal direction compared to the full average stress vs. strain curves from mini-tensile samples.

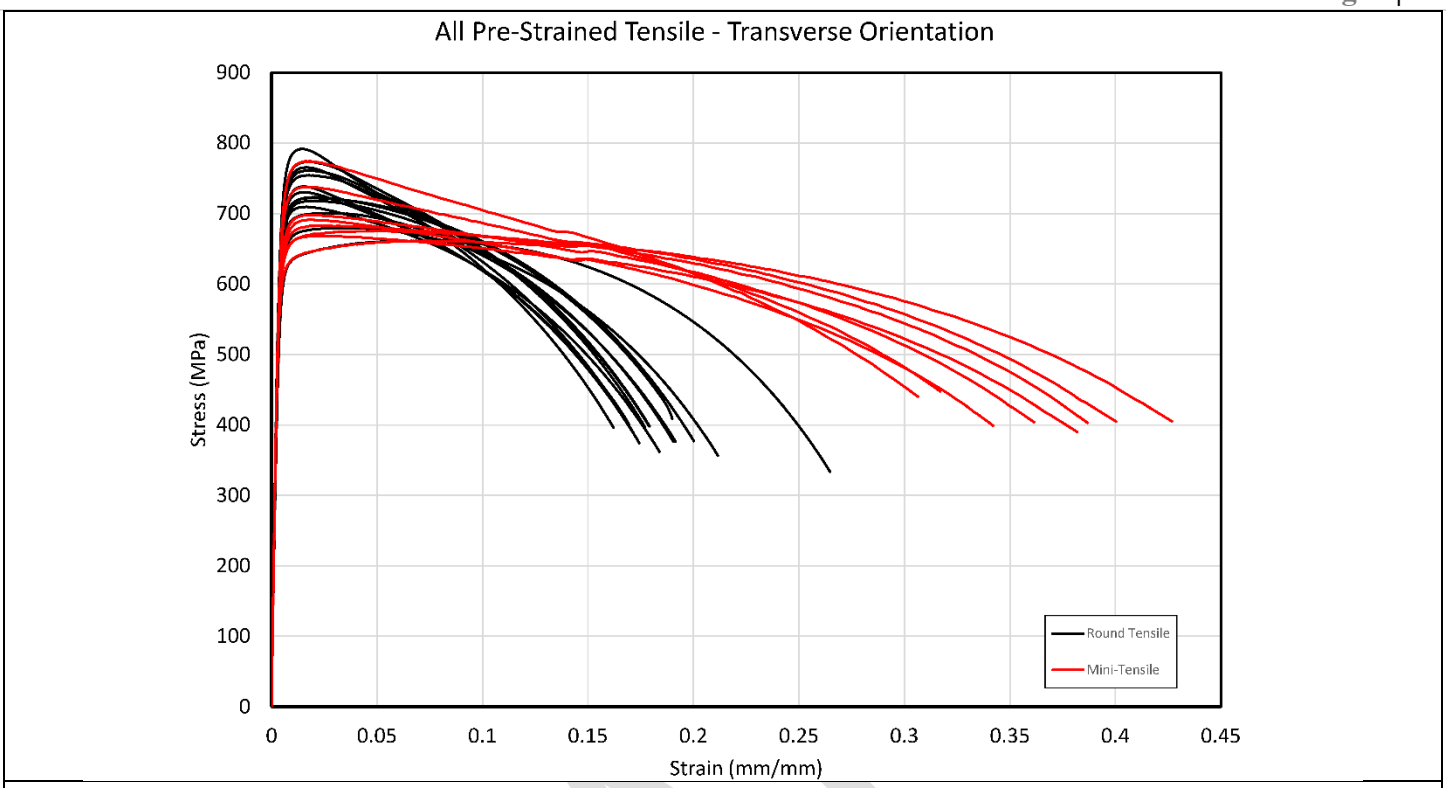

Figure 50. Full stress vs. strain curves from bulk pre-strained X70 round tensile specimens tested in the transverse direction compared to the full average stress vs. strain curves from mini-tensile samples.

Regardless of specimen geometry, the modulus is anticipated to change with increasing amounts of pre-strain. However, similar to the round tensile specimens, the change in modulus for bulk pre-strained mini-tensile specimens is relatively small comparatively and because of the high scatter it is difficult to define an adequately correlated trend useful for predictions (Figure 51). In contrast, the maximum stress plotted against the longitudinal engineering pre-strain for all bulk pre-strained mini-tensile specimens is shown in Figure 52 and shows a more distinct increasing relationship. Like the round tensile results, the point illustrated here is that in general, an increase in pre-strain increases the strength of the local material. Also like the pre-strained round tensile results, the "toughness", or the total strain energy density up to failure also increases with increasing pre-strain.

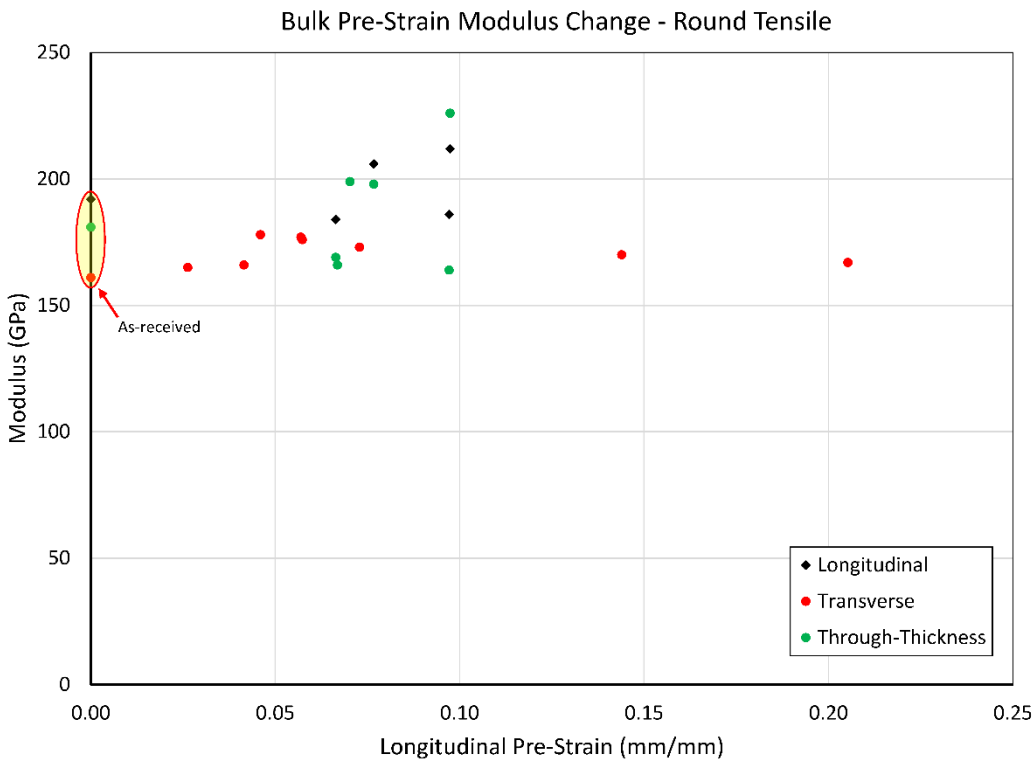

Figure 51. Elastic modulus of mini-tensile samples from bulk pre-strained X70 as a function of the longitudinal engineering pre-strain in the specimen blank taken from the wide-plate.

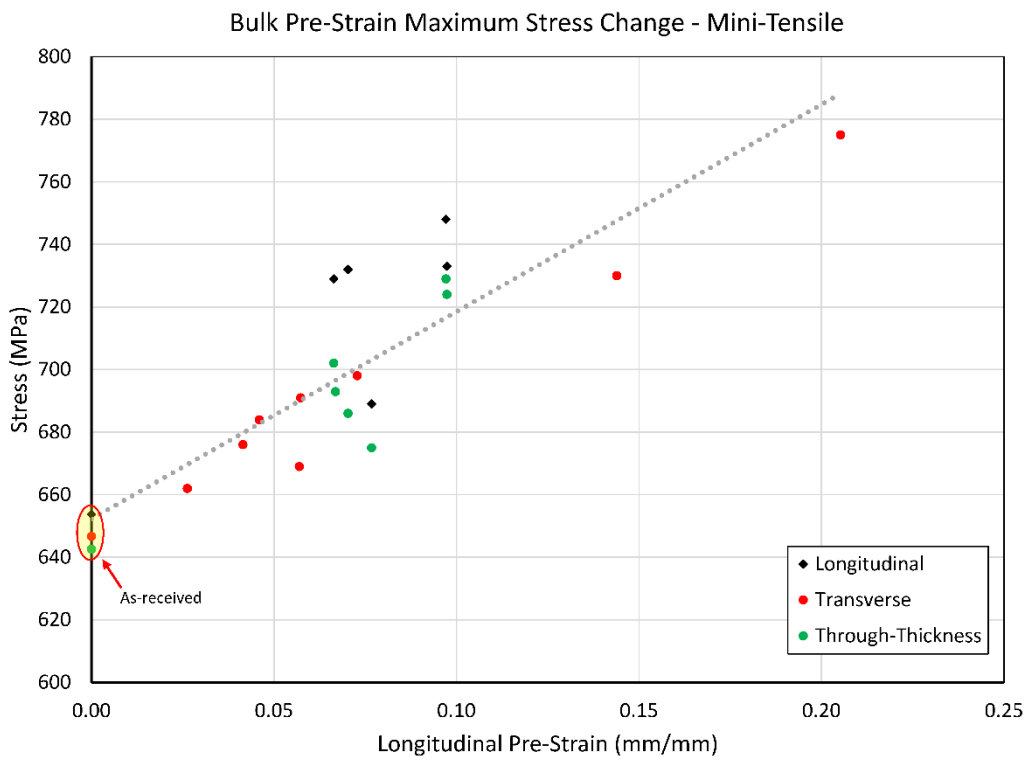

Figure 52. Maximum stress of mini-tensile samples from bulk pre-strained X70 as a function of the longitudinal engineering pre-strain in the specimen blank taken from the wide-plate.

The strain energy density associated with the pre-strain, U_{PS}, experienced by each specimen was calculated. The strain energy density at failure, U_f, of the pre-strained specimens was also calculated independent of that associated with the pre-strain event. Here again, the total cumulative strain energy density, U_T, is simply the sum of the strain energy density resulting from the pre-straining event and the strain energy density resulting from the tensile failure, regardless of orientation.

Figure 53 provides the total cumulative strain energy density experienced by each sample versus the longitudinal pre-strain associated with each specimen. The total cumulative strain energy density for as-received (longitudinal, transverse and through-thickness) samples is shown for reference, where U_{PS} is assumed to be equal to zero for as-received samples. Despite the strain energy density being independent of the reference frame, the data and related trend lines in Figure 53 suggest that the results of the through-thickness direction samples are not well aligned with the longitudinal and transverse direction data. Even with relatively high scatter the slopes of the trends are similar.

Another notable difference between the mini-tensile results and the round tensile results is that the as-received round tensile results are not in alignment with the pre-strain trend, whereas the results of mini-tensile samples are well aligned. This distinction may suggest that mini-tensile specimens sectioned from bulk pre-strained material do not fully retain residual strains that would be present in the bulk material. This is especially relevant in the interest of testing material properties and conditions like those found in the process zone of an unstable high-rate ductile failure.

DRAFT

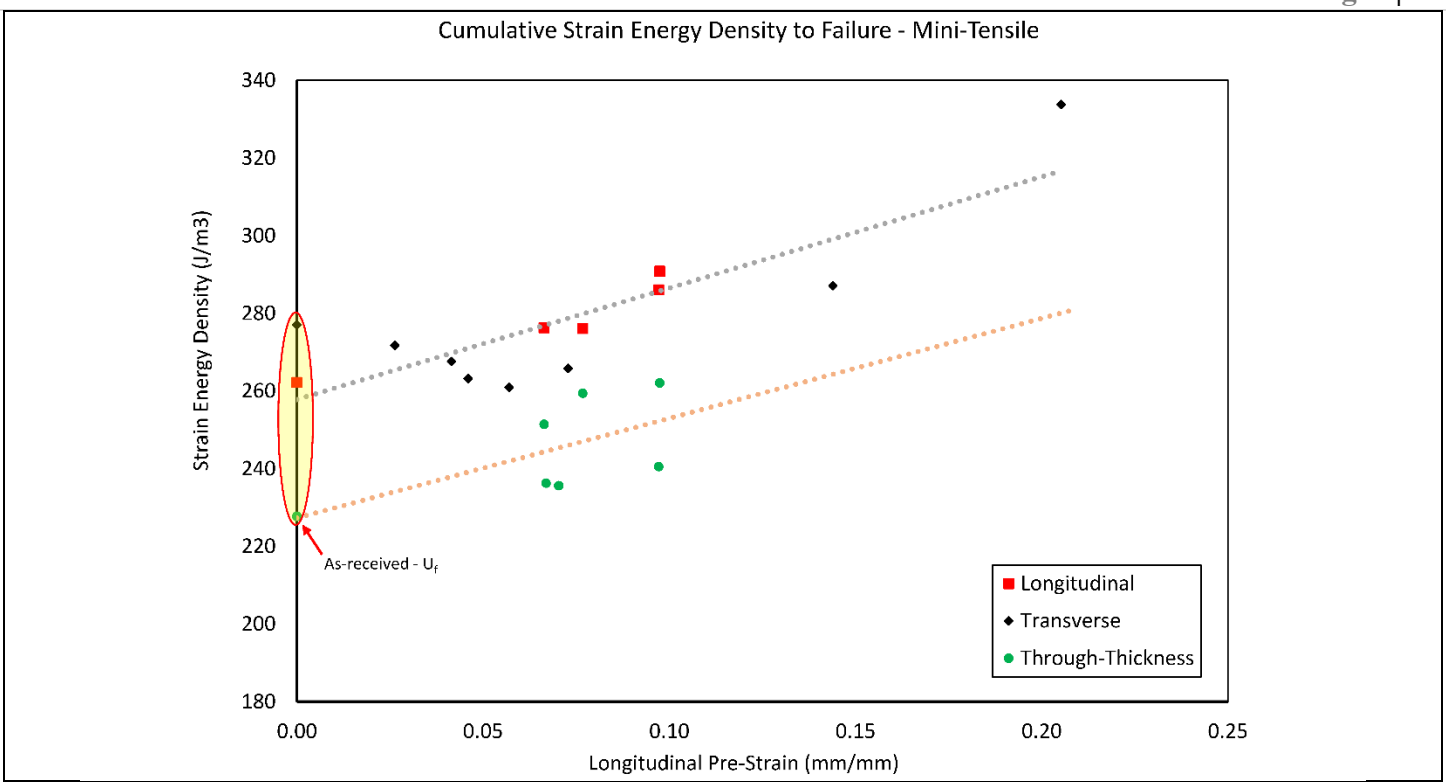

Figure 53. Cumulative strain energy density to failure for bulk pre-strained X70 mini-tensile samples tested in longitudinal, transverse and through-thickness orientations.

Regardless of bias or orientation dependence, the trends created by the data indicate that pre-straining a specimen plastically by any amount effectively "toughens" the material as indicated by an increasing strain energy density required to fail the material. The as-received material (mini-tensile results) exhibited an average strain energy density to failure of 269.6 J/m^3 (for the longitudinal and transverse directions), while the intercept of the pre-strained longitudinal and transverse data in Figure 53 indicates that the minimum amount of strain energy density required to fail the material is 257.8 J/m^3. The as-received through-thickness average strain energy density to failure is 227.7 J/m^3 and the trend shown in Figure 53 for the through thickness data is nearly identical with an intercept value of 227.3 J/m^3.

The strain energy density required to fail a pre-strained mini-tensile sample versus the pre-strain magnitude is provided in Figure 54. Once again, the as-received strain energy density at failure is provided as a reference.

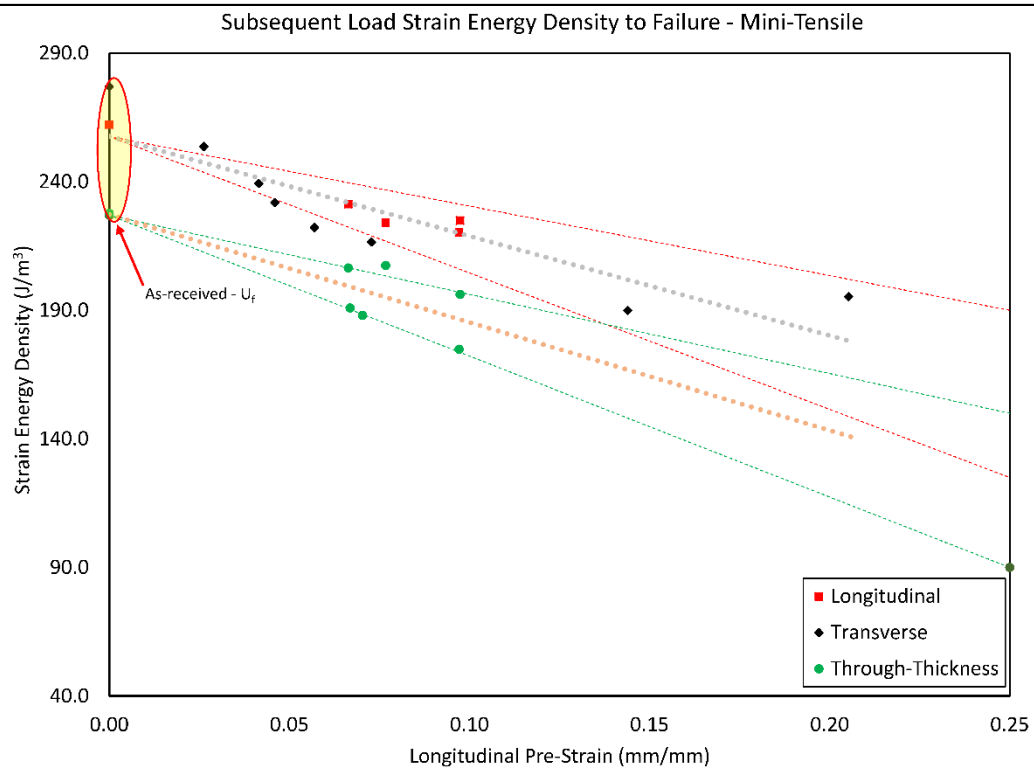

Figure 54. Strain energy density to failure for bulk pre-strained X70 mini-tensile samples tested in longitudinal, transverse and through-thickness orientations. Data is provided for final load incursion only and does not include strain energy density accumulated during pre-straining.

Similar to bulk pre-strained round tensile data, the data shown in Figure 54 indicate that the strain energy density required to fail the material once it has been pre-strained decreases as a function of increasing pre-strain magnitude. Fitting a single linear trend to the longitudinal and transverse data indicates that the minimum amount of strain-energy required to fail the material once the material has been pre-strained is 257.6 J/m^3. The strain energy density at failure for as-received (longitudinal, transverse and through-thickness) specimens is shown for reference. The as-received through-thickness average strain energy density to failure is 227.7 J/m^3 and the trend shown in Figure 54 for the through thickness data is nearly identical with an intercept value of 227.3 J/m^3. Given the repeatability of the estimated strain energy density required to fail a pre-strained component, and the fact that this represents a physical manifestation of damage accumulation, it is postulated that the appropriate error bands associated with the statistical nature of crystalline material failure would be represented as non-parallel lines emanating from the estimated minimal value of 257.6 J/m^3, and 227.3 J/m^3 for combined longitudinal and transverse directions as well as the through-thickness direction respectively.

A validated correlation between round tensile results and mini-tensile results is not presented here, it is interesting however that the strain energy density required for failure of pre-strained mini-tensile specimens is approximately twice that of the round tensile specimens at all pre-strained levels.

3.3.2.4 Charpy V-Notch Testing – Pre-Strained Material

The Charpy V-Notch results for pre-strained X70 plate follow in this section. The results are given numerically in Table 18 and shown graphically in Figure 55. All tests were performed at room temperature.

Table 18. Pre-Strained X70 Charpy V-Notch Results

Specimen ID	Pre-Strain (mm/mm)	Crack Path	Absorbed Energy (J)	Lateral Expansion (mm)	Break Type
C1a	0.0196	Through-Thickness	458.7	1.77	NB
C1b	0.0288	Longitudinal	318.5	1.74	B
C2a	0.0188	Through-Thickness	459.0	1.76	NB
C2b	0.0241	Longitudinal	354.9	1.89	B
C3	0.1535	Longitudinal	226.8	1.88	B
C4	0.0896	Through-Thickness	362.1	1.78	B
C5	0.0928	Longitudinal	189.7	2.02	NB
C6	0.0911	Longitudinal	212.4	2.11	B
C7	0.0756	Through-Thickness	344.7	1.59	B
C8	0.0566	Through-Thickness	429.6	1.63	NB

The data in Figure 55 indicates a trend of decreasing energy required to fail the specimen as a function of increased longitudinal pre-strain. For reference, the average absorbed energy from as-received samples (X70 - 2 and X70 - 7) are also provided, the crack path was verified to be longitudinal in these specimens. Note that the as-received material results provided in Figure 55 show non-broken failures resulting from large-scale plasticity. Only 60 % of the pre-strain results provided in Table 18 and Figure 55 were from "broken" specimens while 40 % of the pre-strained specimens exhibited large-scale plasticity. These differences in failure morphology provide a warning to be wary of applying Charpy results from as-received material to the failure mechanisms manifesting in in-service ductile failure.

DRAFT

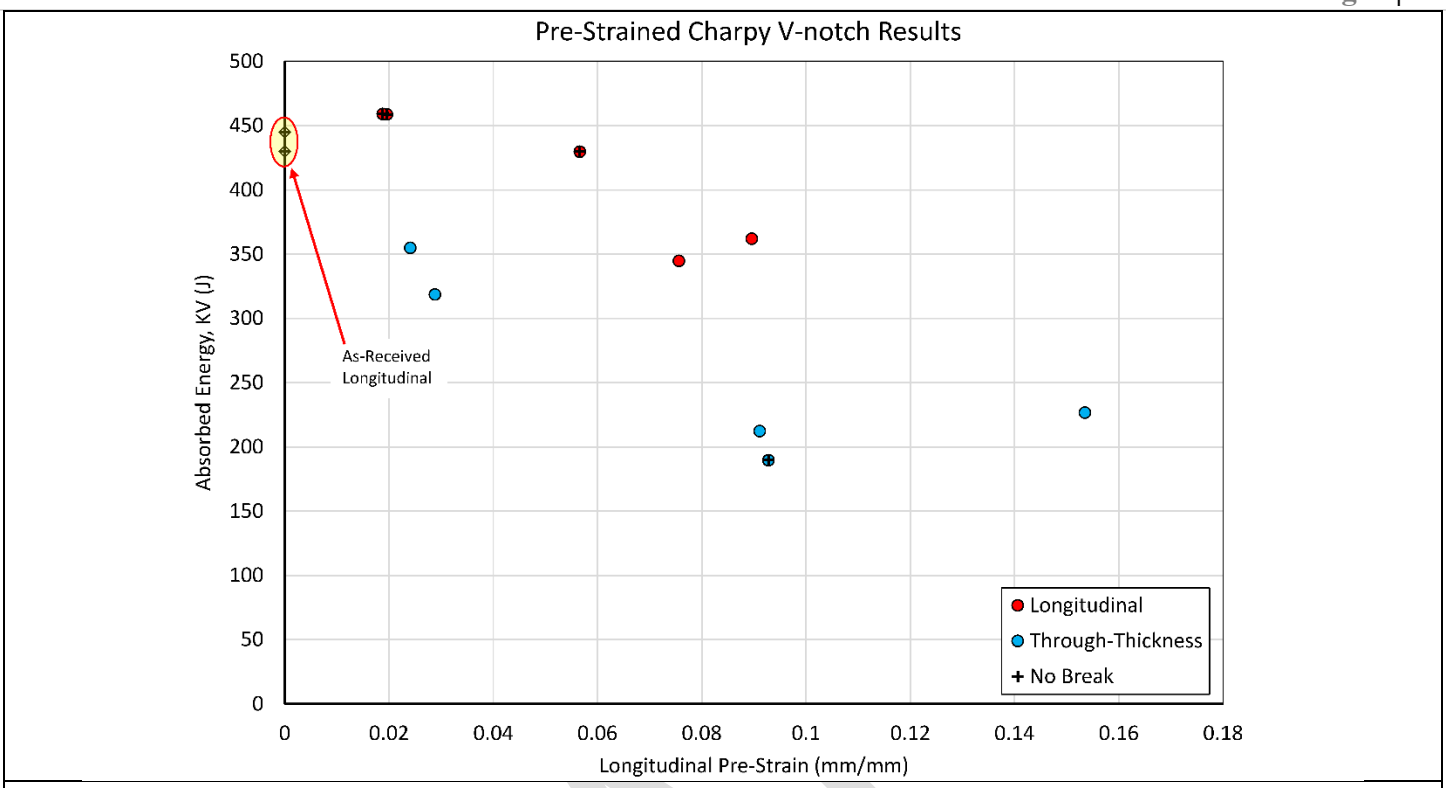

Figure 55. CVN absorbed energy for bulk pre-strained X70 material tested with two crack path orientations at room temperature.

In a similar method of comparison, the bulk pre-strained Charpy results are plotted along with the strain energy density data from pre-strained round tensile specimens (see Figure 47), and is provided in Figure 56. In Figure 56, only the broken Charpy specimens are reported. Here again, it is shown that "toughness" decreases with increasing pre-strain. A distinction of note, the absorbed energy required to break a specimen in dynamic loading decreases at a significantly higher rate than does the strain energy density required to break the specimen in monotonic tensile loading. While not surprising, this must be considered when reviewing in-service ductile failure.

DRAFT

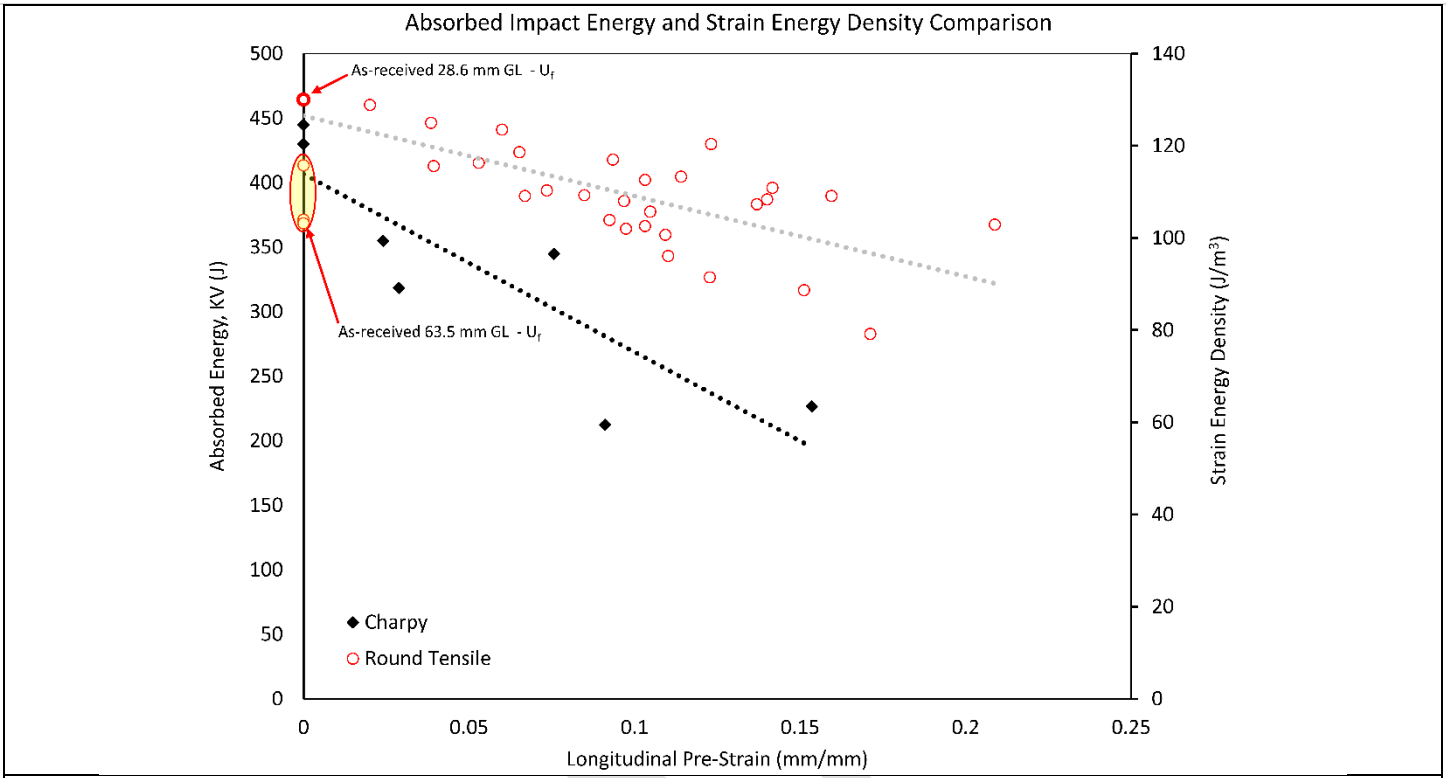

Figure 56. CVN absorbed energy and strain energy density to failure for bulk pre-strained X70 material tested as a function of pre-strain. All results at room temperature.

4 Constitutive Material Modelling

Ductile failure of linepipe steels occurs as a progression of the following events: (1) localized damage is induced in the pipe (*e.g.*, third-party damage) such that the damage behaves as a crack; (2) if the localized damage does not result in a through-wall crack, the crack will propagate to through-wall proportions as a result of intended use; (3) once the crack has penetrated the pipe wall thickness, the pressurized working fluid within the pipe is released, producing a wave propagating in the longitudinal direction of the pipe. This wave is known as a decompression front. The decompression front induces localized through-thickness necking directly in front of the crack tip; (4) the localized necking immediately in front of the crack tip provides a path of least resistance for crack propagation. The driving force for crack propagation is largely the sudden escape of working fluid within the pipe. This depressurization tends to deform the pipe into a U-shape in the crack wake. While the driving force for crack propagation and the energy source of the decompression front are intrinsically linked, the two phenomena produce damage that propagate at speeds independent of one another. For ductile failure to occur, the decompression front must precede the running crack, such that it may produce the required through-thickness plasticity enabling crack propagation. Inversely, if the crack travels faster than the decompression wave, the undamaged material that the crack must propagate through will tend to arrest the crack due to its inherent,

undamaged, fracture toughness. Finally, the crack propagation surface is indicative of traditional ductile features, including manifesting along a plane at approximately 45° to the applied load, *i.e.*, plane of maximum shear.

A failure model which intends to capture the physics of the ductile failure phenomenon must incorporate the following characteristics, at minimum:

- The inelastic deformation response predicted by the materials constitutive model must be rate dependent. Specifically, the plasticity constitutive relations must be calibrated to loading rates on the order of those seen when a ductile failure occurs in a linepipe.
- If the material exhibits anisotropic deformation response, the constitutive model must capture the appropriate anisotropy inherent to the material.
- The state of stress and strain produced by the longitudinal decompression front must be captured and used as initial conditions for crack propagation. Specifically, the constitutive model must be history dependent, such that prior damage may be included. Additionally, the damage accumulation model, or failure model, must also be history dependent.
- Volumetric considerations must be accounted for. Specifically, if an energy criterion is used to predict failure (e.g. ductility exhaustion, energy dissipation, etc.), the failure model must capture the volumetric effects associated with the plastic energy dissipation of metals.

4.1 Current State of the Art

The following theories are commonly used in the constitutive relations for ductile failure:

- Crack driving force primarily due to the opening of the pipe in the crack wake.
- Failure predicted by the dynamic fracture toughness of the material, G_d.
- Failure predicted by crack tip opening angle (CTOA).
- Failure predicted by energy dissipation rate and critical dissipation energy, R.
-

4.2 Gap Analysis

The four most common theories used to predict ductile crack propagation and arrest have been shown to have shortcomings in their implementations. First, the hinging of the material in the crack wake to produce a U-shaped pipe post failure occurs at a time scale that would indicate that it could not precede crack propagation. Furthermore, fracture surface morphologies do not indicate large scale Mode II characteristics, as this phenomenon would tend to produce. Next, predicting failure by use of a material parameter derived from planar

deformation responses, such as G_d and CTOA, does not accurately account for the through-thickness deformation resulting from the propagating decompression front. In this case, the deformation history that enabled the crack propagation is not accounted for. Finally, the use of an energy parameter as a predictor for ductile failure is promising. However, the calibration of an energy parameter incorporating multiple loading rates and multiple length scales has yet to be performed.

4.3 Project Progress

Monotonic testing associated with this work has indicated that the material exhibits anomalous deformation response as a function of orientation and specimen size. Specifically, the inelastic deformation response from the onset of loading to the ultimate tensile strength is relatively consistent for transversely oriented and in-plain diagonally orientated round tensile specimens as well as longitudinally oriented, transversely oriented, and through-thickness oriented mini-tensile specimens (see Figure 36). However, the longitudinally oriented round tensile specimens (both gage lengths) exhibited marked strength increase over all other specimens tested (see Figure 36). Given the anomalous coupled orientation- and size-dependent deformation response, it is unclear at this time how to best proceed with a quasi-static constitutive model.

In addition to the quasi-static monotonic tests conducted at NIST, dynamically loaded direct-tension Split Hopkinson Pressure Bar (SHPB) monotonic tests were performed at the University of Alabama. Miniature specimens, similar in size to the miniature specimens tested at NIST under quasi-static conditions, were manufactured by use of electron discharge machining (EDM) in the longitudinal, transverse, and through-thickness orientations. Specimen geometry for the SHPB specimen is provided in Figure 57.

DRAFT

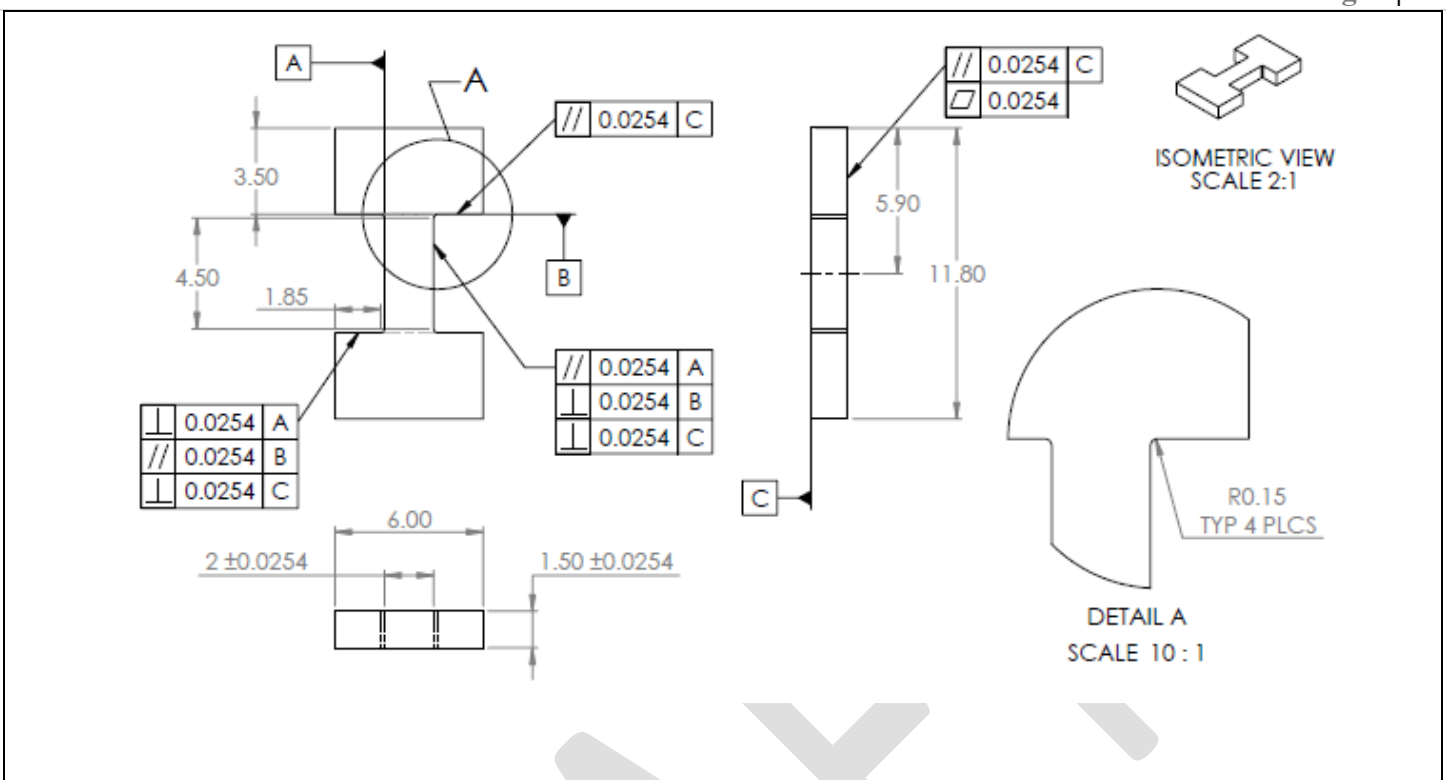

Figure 57. SHPB specimen geometry. Units are in millimeters.

Three material orientations (transverse, longitudinal, and through thickness), were tested in triplicate by use of the SHPB apparatus. Average dynamic plastic tensile results (strain rate of 3000/s) are provided in Figure 58 as a function of specimen orientation. Note that the elastic response captured during dynamic loading of SHPB testing is typically neglected and is therefore absent from the plot.

DRAFT

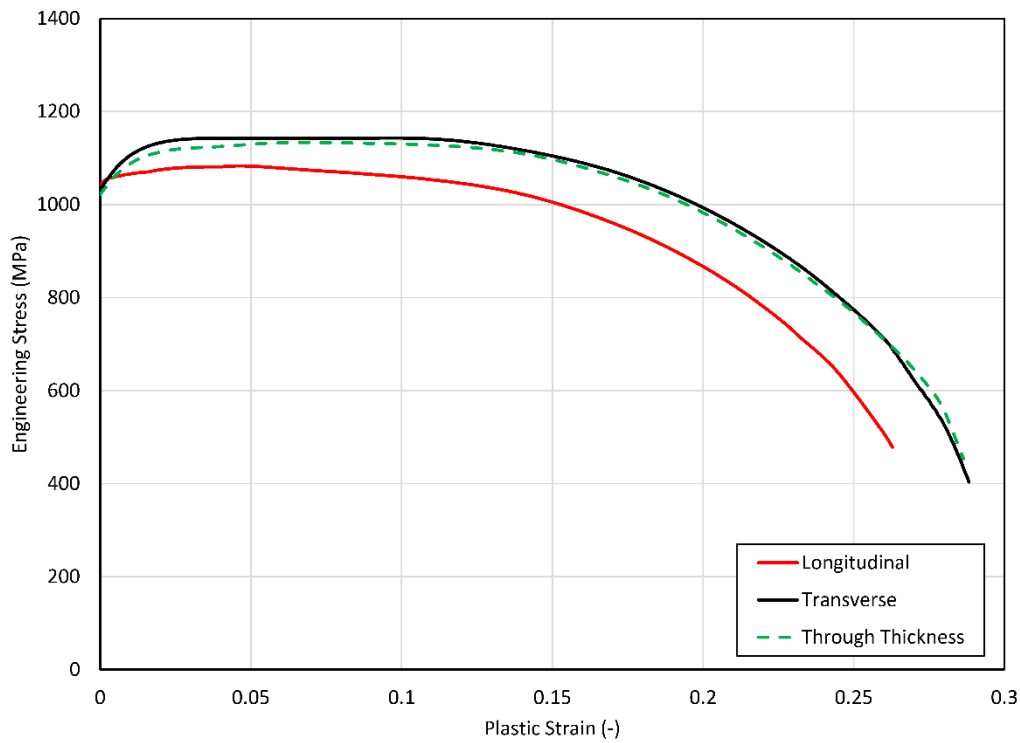

Figure 58. Dynamic SHPB tensile test results, $\dot{\varepsilon}$ = 3000/s.

Unsurprisingly, the material exhibited a marked increase in yield strength and ultimate tensile strength at strain rates of 3000/s, when compared to quasi-static results (compare Figure 35 with Figure 58). Furthermore, the material exhibited a substantial decrease in elongation to failure when loaded at a strain rate of 3000/s compared to quasi-static load rates. Interestingly, the longitudinally-oriented specimens exhibited reduced dynamic yield strength and ultimate tensile strength compared to the transversely-oriented and through-thickness-oriented specimens. The dynamic tensile test results, including the strain energy density to failure is provided in Table 19.

Table 19. Stress and strain energy density to failure for dynamically loaded specimens ($\dot{\varepsilon}$=3000/s)

	Longitudinal	Transverse	Through-Thickness/Diagonal	**Average**	STDEV
Yield Stress (MPa)	1041	1032	1022	**1032**	10
Max Stress (MPa)	1083	1143	1134	**1120**	32
Failure Stress (MPa)	479	403	454	**445**	38
U (J/m3)	251	291	287	**276**	22

In support of future constitutive modelling by others, the Ramberg-Osgood model has been calibrated up to the ultimate tensile strength for all the average tensile curves created as part of this work. The Ramberg-Osgood

constitutive model incorporates the material-specific, rate-specific and environmental-specific constants *k* and *n* to predict strain, ε, given a value of elastic modulus, *E*, and stress, σ, according to Equation 1.

	$\boldsymbol{\varepsilon = \frac{\sigma}{E} + k\left(\frac{\sigma}{E}\right)^{n}}$	**(1)**

Calibrated Ramberg-Osgood parameters are provided in Table 20 for round tensile specimens, the quasi-static mini-tensile specimen results, and high strain rate miniature specimen results.

Table 20. Ramberg-Osgood Parameters for all average tensile curves produced as part of this work

	***E* (GPa)**			***K* (unitless)**			***n* (unitless)**		
	Long	Trans	Diag/TT	Long	Trans	Diag/TT	Long	Trans	Diag/TT
Round	228	181	183	2.45E+130	8.00E+130	1.60E+130	52.3	27	53.4
Mini-	192	161	181	5.60E+96	2.10E+61	5.70E+55	39.6	26	23.2
SHPB	-	-	-	1.30E+273	5.00E+81	9.00E+97	122	38.5	44.9

This work presumes that ductile fracture occurs when the cumulative strain energy density imparted to the material reaches a critical value. Given that strain energy density is independent of reference frame, the quantity may be summed as a result of successive energy event, regardless of material and loading orientation. Table 21 provides the average strain energy density to failure for dynamically loaded miniature specimens ($\dot{\boldsymbol{\varepsilon}}$ = 3000/s), miniature specimens experiencing quasi-static loading ($\dot{\boldsymbol{\varepsilon}}$ = 0.001/s), quasi-statically loaded round tensile specimens (both gage lengths)

Table 21. Strain energy density values for the average test results collected as part of this work

	Longitudinal	Transverse	Through-Thickness/Diagonal	**Average**	STDEV
SHPB	251	291	287	**276**	22
Mini-Tensile	263	277	228	**256**	26
Round Tensile (short)	130	-	-	**130**	-
Round Tensile (long)	102	114	103	**106**	6

Recall that while the stress values resulting from the testing performed here are relatively consistent across orientations and specimen size, the strain to failure values vary drastically as a function of specimen size. Barba's Law provides for the normalization of differences in strain to failure values resulting from different specimen sizes. Barba's Law, (see Equation 2) predicts the elongation to failure, $\boldsymbol{\varepsilon_f}$, as a function of the material-specific parameter, $\boldsymbol{\beta}$, the initial cross-sectional area of the specimen, $\boldsymbol{A_0}$, the initial length of the specimen, $\boldsymbol{l_0}$, and the theoretical volume-independent stain to failure of the material, $\boldsymbol{\varepsilon_0}$.

	$\boldsymbol{\varepsilon_f = \beta \frac{\sqrt{A_0}}{l_0} + \varepsilon_0}$	**(2)**

Barba's Law is applied here to correlate the strain energy density to failure, $\boldsymbol{U = \sigma * \varepsilon}$, for all of the average as-received test results provided in Table 21. The calibration constants for the strain energy density to failure as a function of strain rate and specimen volume are provided in Equation 3 below. The correlation coefficient for the calibrated results is $R^2 = 0.955$.

	$\boldsymbol{U = \beta \frac{{A_0}^{0.5}}{l_0} + U' = 610 \frac{{A_0}^{0.5}}{l_0} + 36}$	**(3)**

The resulting correlation coefficient indicates a very strong correlation between the strain energy density at failure and the volumetric quantity $\boldsymbol{\frac{\sqrt{A_0}}{l_0}}$. While not conclusive, this result indicates that strain-rate plays a minimal role, if any, in the cumulative strain energy density at failure. When calibrating Barba's Law to all the individual quasi-static test results, the resulting calibration constants are given in Equation 4, with a correlation coefficient of $R^2 = 0.903$.

	$\boldsymbol{U = 558 \frac{{A_0}^{0.5}}{l_0} + 51}$	**(4)**

The trends based on geometry become very clear after combining and plotting the cumulative strain energy density to failure for all the quasi-static tensile tests versus the longitudinal pre-strain, which is effectively combining Figure 46 with Figure 53. This combined plot is shown in Figure 59. For reference, the average strain energy density of all SHPB specimens is also shown in Figure 59, where the average value of 276.6 J/m^3 is nearly identical to the average as-received transversely oriented mini-tensile specimens.

DRAFT

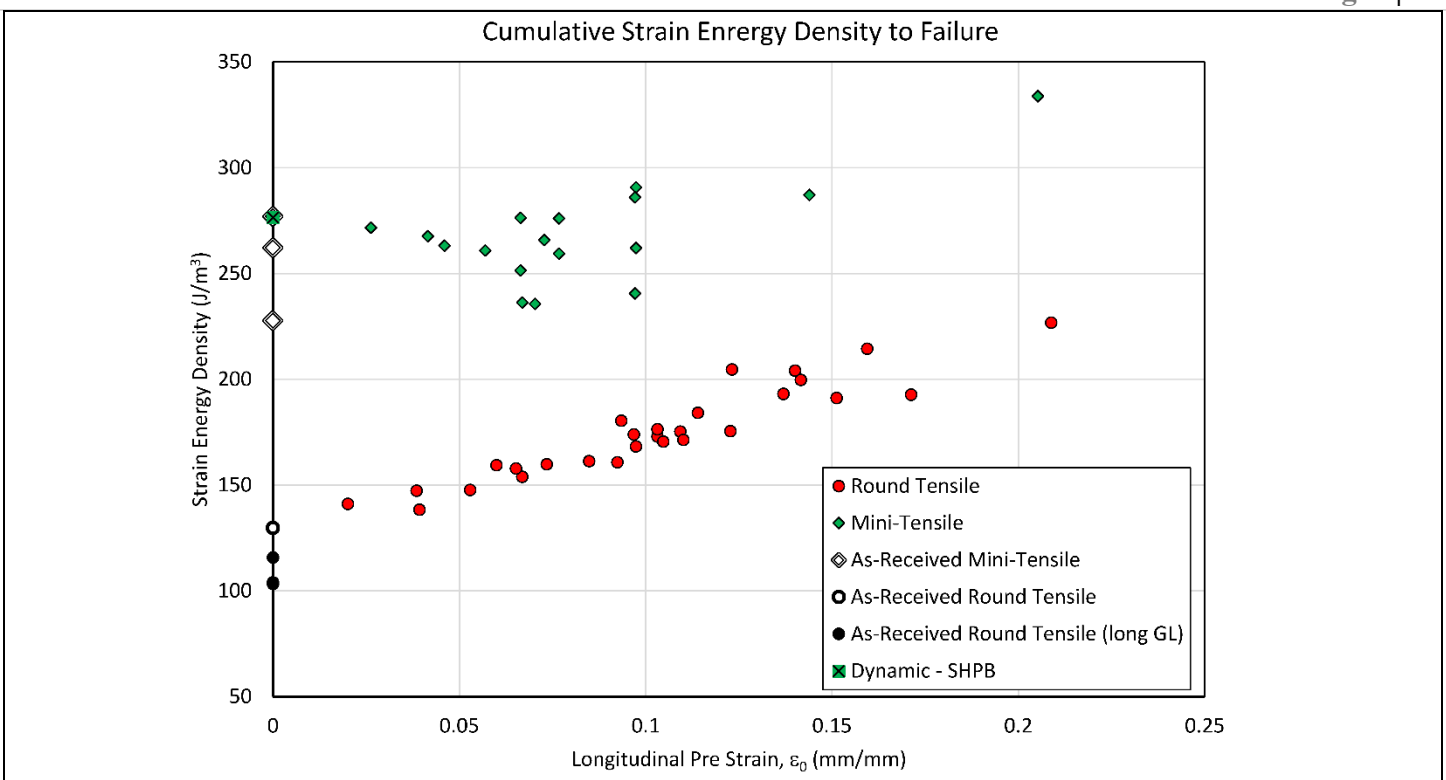

Figure 59. Cumulative strain energy density to failure versus pre-strain for all quasi-static tensile tests.

Based on the results shown in Figure 59, a ductile failure criterion is proposed which predicts the onset of failure as a function of loading history effects (pre-strain) and volumetric effects. Note that the results thus far indicate that strain energy density to failure is insensitive to loading rate. The model predicts the onset of ductile fracture when the strain energy density reaches a critical value, U_{crit}, according to the generic form provided in Equation 5.

$$U_{crit} = U_0 + \frac{dU_f}{d\varepsilon_0}\varepsilon_0 \quad (5)$$

The critical strain energy density is defined as a function of the volume-dependent as-received material strain energy density, $\boldsymbol{U_0}$, the historical strain, $\boldsymbol{\varepsilon_0}$, and the change in strain energy density to failure per change in historical strain, $\frac{dU_f}{d\varepsilon_0}$. Note that the volume-dependent as-received material strain energy density is defined in Equations 3 and 4 . The full ductile failure predictive equation is therefore provided in Equation 6.

$$U_{crit} = \frac{{A_0}^{0.5}}{l_0} + U' + \frac{dU_f}{d\varepsilon_0}\varepsilon_0 \quad (6)$$

Calibration of the ductile failure predictive model yields the following values for the calibration constants: $\boldsymbol{\beta}$ = 610, $\boldsymbol{U'}$ = 36 J/m^3, and $\frac{dU_f}{d\varepsilon_0}$ = 484 J/m^3. Calibrated correlations for all the data collected in this work are provided in Figure 60.

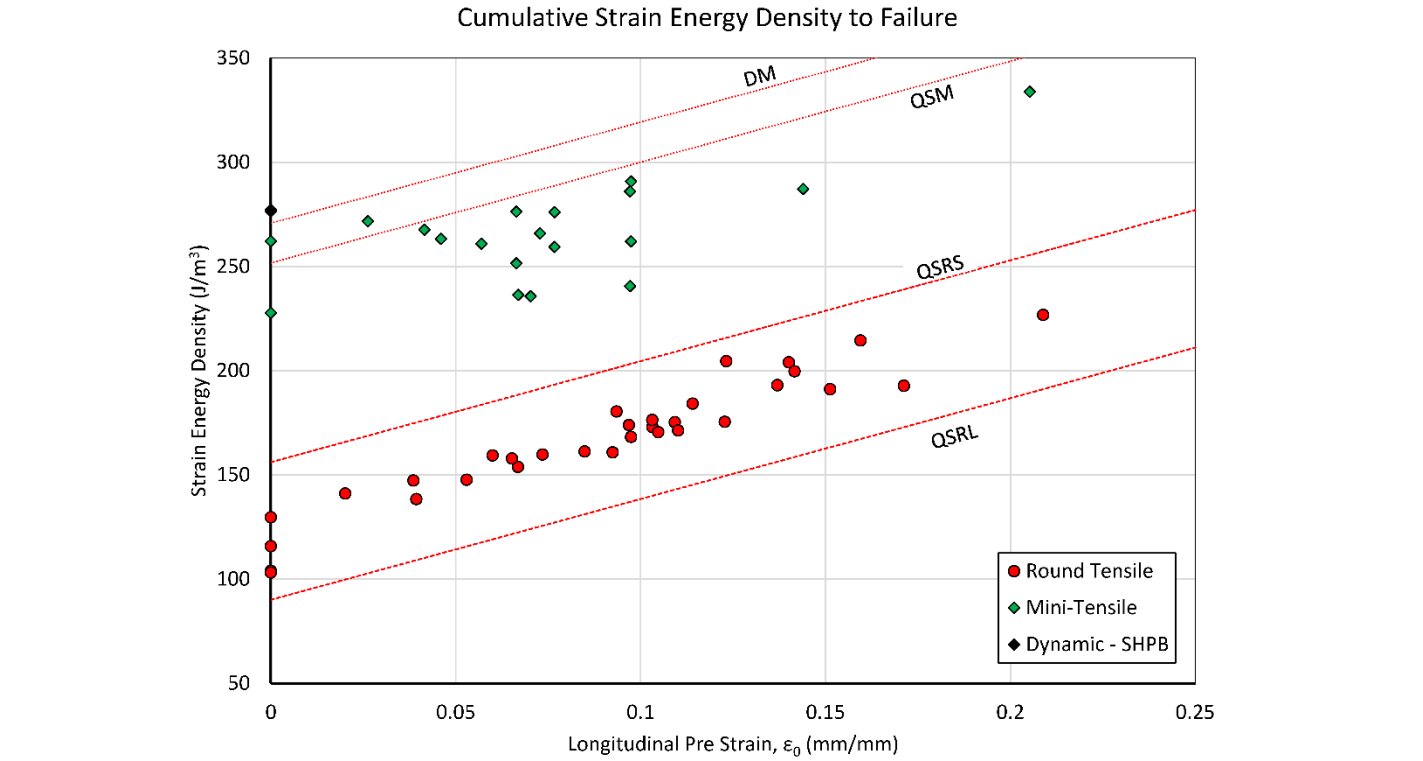

Figure 60. Model correlations compared to all the data collected as part of this work. Barba's Law exponent = 0.5, the trend labels DM, QSM, QSRS and QSRL correspond to Dynamic Mini, Quasi-Static Mini, Quasi-Static Round Short and Quasi-Static Round Long.

Note that while the model trends well with the experimental data as calibrated, it is insufficient for life modelling purposes. It is therefore proposed that the square-root in Barba's Law be modified to better fit the data, within reasonable bounds. The modified predictive equation is provided in Equation 7.

$$U_{crit} = \beta \frac{A_0^{0.3}}{l_0} + U' + \frac{dU_f}{d\varepsilon_0}\varepsilon_0 \quad (7)$$

Calibration of the modified ductile failure predictive model yields the following values for the calibration constants: $\boldsymbol{\beta}$ = 40, $\boldsymbol{U'}$ = 76 J/m^3, and $\frac{dU_f}{d\varepsilon_0}$ = 484 J/m^3. Calibrated correlations for all the data collected in this work are provided in Figure 61.

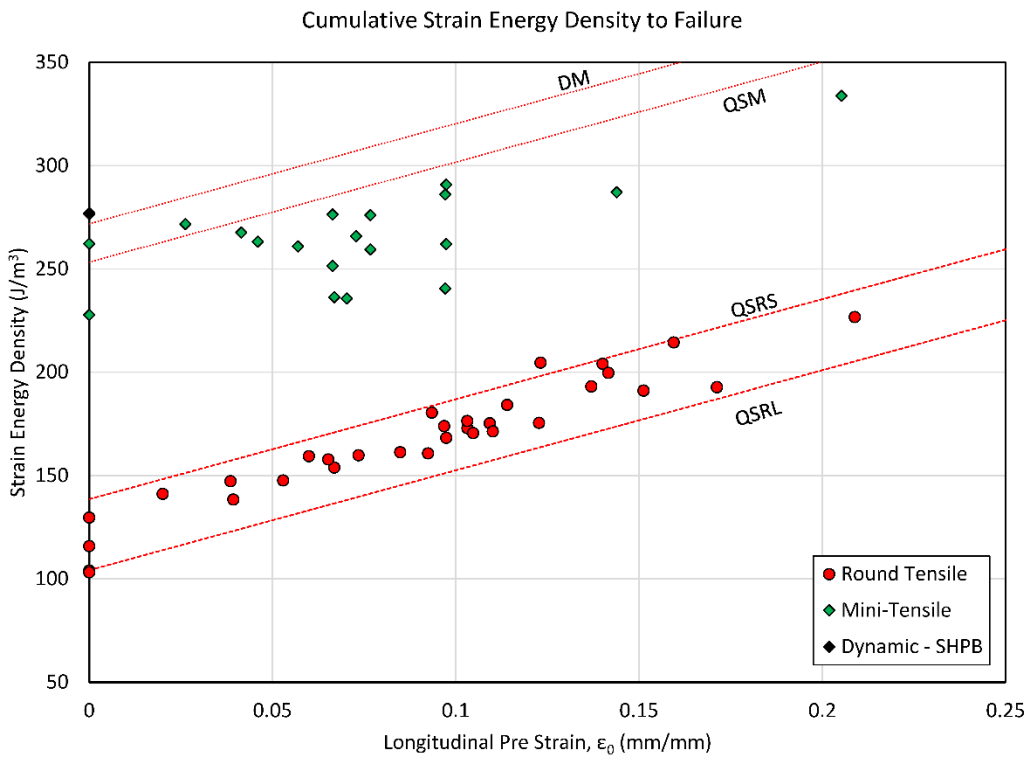

Figure 61. Model correlations compared to all the data collected as part of this work. Barba's Law exponent = 0.3, the trend labels DM, QSM, QSRS and QSRL correspond to Dynamic Mini, Quasi-Static Mini, Quasi-Static Round Short and Quasi-Static Round Long.

The calibrated failure model does a good job of correlating the cumulative strain energy density at failure as a function of specimen size and load history. Ultimately, it is believed that the model may be used to rank the material resistance to the onset of ductile fracture, relative to one another. Specifically, the term $\frac{dU_f}{d\varepsilon_0}\boldsymbol{\varepsilon_0}$ provides insight to the relative amount of damage a material may accumulate prior to failure. That is, a material with a lower value of $\frac{dU_f}{d\varepsilon_0}\boldsymbol{\varepsilon_0}$ will be more likely to sustain a running ductile crack due to the damage caused by the decompression front.

5 Structural Modelling

Structural modelling as part of this project includes both medium scale and large-scale modelling of realistic geometries, loading conditions, and boundary conditions. Specifically, medium and small-scale test specimens must be modeled to match all laboratory conditions of interest. Furthermore, the operational pipe geometry, loading conditions, and boundary conditions must also be modeled to provide support for similitude between the laboratory test results and predicted field results.

5.1 Current State of the Art

The current state of the art to perform structural modelling is implemented in any number of commercial finite element packages (e.g. ABAQUS, SolidWorks, COMSOL, etc.).

5.2 Gap Analysis

To the best of our knowledge, there is not a commercially available finite element package that can perform anisotropic inelastic deformation. This is the purview of research scientists and scientific laboratories focusing wholly on anisotropic plastic deformation behavior.

5.3 Project Progress

The structural modelling effort in Phase II of the project was meant to be a continuing effort beginning with the medium-scale test conceptual design. To date, the structural modelling for this project has included finite element modelling of all test geometries as well as calibration of a transversely isotropic constitutive model coupled to the finite element models.

6 Conclusions

This phase of the project focused on as-received and pre-strained material characterization of API 5L-X70 pipeline steel. The as-received steel used in all experiments was in the form of a flat plate taken from production prior to being formed and welded into a linepipe section. The test matrix for characterization included differences in geometry, orientation and pre-strain levels. The metallurgical characterization included physical metallurgy and mechanical metallurgy. The physical metallurgy was comprised of optical metallographic examination, crystallographic orientation, grain size measurements, and the chemical composition was documented. The mechanical metallurgy was comprised of wide-plate pre-straining, tensile testing and Charpy V-Notch impact testing.

The experimental work focused on a method of developing a pre-strain in bulk material that could provide a large range of pre-strain levels for subsequent small-scale testing. Strain histories developed with the wide-plate ranged from 2 % to 21 %. Small-scale tensile geometries included standard round dog-bone shaped specimens

as well as miniature flat dog-bone shaped specimens. It was shown that in-situ pre-straining of a round dog-bone tensile specimen cannot replicate the strain and strain history of a bulk pre-strained wide-plate.

Standard round tensile results of as-received steel indicated a strong orientation effect orthogonal to the rolling direction of the plate, corresponding to a strong <101> crystallographic orientation. The microstructural banding, grain size, phases, and phase distribution were not adequate indicators for such a dominant response. Standard round tensile results of as-received steel in the rolling direction and diagonal (45 degrees) to the rolling direction are very similar and the average data fall well within the uncertainties of the data from either direction. Changes due to pre-straining manifest in a reduction of grain sizes and changes in crystallographic orientation.

Miniature scale tensile dog-bones were designed with appropriate machine fixtures and instrumentation to determine the in-plane and out-of-plane (through-thickness) tensile properties. Differences due to scale and geometry were anticipated. Direct fundamental correlations between standard round tensile and mini-tensile specimens were not be made in this phase and as such future work toward this correlation is suggested. The through-thickness tensile properties are sufficiently different and lower than the longitudinal and transverse orientations. It is also indicated that the changes in through-thickness tensile properties as a function of bulk pre-strain have the same rate of decrease as do the longitudinal and transverse tensile properties. Incongruent with the dominant as-received longitudinal data in round tensile specimens, the orientation dominance was not observed in the as-received mini-tensile results.

While changes in elastic modulus have been documented in the literature and associated with damage accumulation, the scatter in the data reported herein is high with little correlated change as a function of bulk longitudinal pre-strain. The bulk pre-straining of the wide-plate resulted in a significant amount of cold work affecting an increase in maximum stress. The cumulative strain energy density also increased as a function of pre-straining acting to toughen the steel. However, the strain energy density to failure for each specimen as a function of pre-strain decreased. This indicates that once the material is pre-strained the amount of energy to cause a failure decreases with increasing pre-strain.

Charpy V-Notch testing of as-received and pre-strained material indicates a significant decrease in absorbed energy necessary for failure as a function of increasing bulk pre-strain. Charpy results however have a great deal of scatter and some tests reported here did not result in broken specimens. Absorbed energy in this study by way of notched bar impact testing does not produce results that are reliable enough for predictive needs. However,

the test was useful to illustrate and validate that the toughness is compromised with increasing pre-strain, ultimately suggesting that not only is the Charpy test not well suited to predicting full scale behavior but that as-received material properties should not be used to predict or model full-scale crack propagation or arrest behavior.

A failure model has been proposed which, when calibrated, can predict the onset of ductile failure for a given material as a function of loading history and component volumetric considerations. Specifically, the model predicts the onset of ductile failure as a function of critical accumulation of energy density within the component. The research to date suggests that the model is applicable for quasi-static loading as well as dynamic loading ($\dot{\boldsymbol{\varepsilon}}$=3000/s). Implementation of the model may be performed in several ways. First, the model may be used to rank a materials' ability to resist ductile fracture relative to other materials. In this case, one could simply calibrate the parameter describing the materials' ability to accumulate strain energy density prior to failure as a function of changing load history, $\frac{dU_f}{d\varepsilon_0}$, for several materials, and rank the materials numerically (a higher value of the parameter would indicate a greater ability to withstand damage prior to the onset of failure). Secondly, the calibrated model may be employed within a finite element package to predict the onset of failure given known loading conditions and boundary conditions. The primary impact of this work is to expand upon the tools available to ultimately mitigate ductile failure of linepipe steels.

7 Phase III – Future Work

DRAFT

8 Bibliography

[1] Anderson TL (1990) Elastic-Plastic Fracture Mechanics - A Critical Review. (Ship Structure Committee, U.S. Coast Guard, Report No. SSC-345 Part 1).

[2] Andrews RM, Batte, A. D. (2003) Developments in Fracture Control Technology for Gas Pipelines Utilising High Strength Steels. *22nd World Gas Conference*, (International Gas Union, Tokyo, Japan).

[3] Andrews RM, Millwood NA, Batte AD, Lowesmith BJ (2004) The fracture arrest behaviour of 914 mm diameter X100 grade steel pipelines. *2004 International Pipeline Conference*, (American Society of Mechanical Engineers), pp 1693-1701.

[4] Asahi H, Hara, T., Tsuru, E., Morimoto, H. (2009) Development and Commercialization of High-Strength Linepipe. *Pipeline Technology Conference*, (Pipelines International).

[5] Asahi H, Tsuru, E., Ohkita, S., Maruyama, N., Koyama, K., Akasaki, K., Murata, M., Miyazaki, H., Hara, T., Morimoto, T., Sugiyama, M., Shinada, K., Terada, Y., Ayukawa, N., Doi, N., Yoshida, T. (July 2004) Development of Ultra-High-Strength Linepipe, X120. (Nippon Steel Technical Report No. 90).

[6] ASTM E- (2018) Standard Test Methods for Notched Bar Impact Testing of Metallic Materials. *Annual book of ASTM standards ASTM*.

[7] ASTM E (2019) Standard test methods of compression testing of metallic materials at room temperature. *West Conshohocken, PA: ASTM International*.

[8] ASTM E-a (2016) Standard test methods for tension testing of metallic materials. *Annual book of ASTM standards ASTM*.

[9] Besson J, McCowan, C. N., Drexler, E. S. (2013) Modeling flat to slant fracture transition using the computational cell methodology. *Engineering Fracture Mechanics* 104(0):80-95. https://doi.org/http://dx.doi.org/10.1016/j.engfracmech.2013.02.032

[10] Botros KK, Studzinski, W., Geerligs, J., Glover, A. (2004) Determination of Decompression Wave Speed in Rich Gas Mixtures. *The Canadian Journal of Chemical Engineering* 82(5):880-891. https://doi.org/10.1002/cjce.5450820503

[11] Brocks W, Schwalbe, K. H., Zerbst, U. (2006) Structural Integrity Assessment of Thin-Walled Structures. *Advanced Engineering Materials* 8(5):319-327. https://doi.org/10.1002/adem.200600120

[12] Bruschi R, Marchesani, F., Vitali, L., Battistini, A. (2009) Do High Y/T and/or Low UE Impact on Limit State Design of High Grade Linepipes? *Pipeline Technology Conference*, (Pipelines International).

[13] Bruschi R, Biery, N. E., Marchesani, F., Weir, M. S., Macia, M. L. (2009) Long Distance Gas Pipelines: Adopting High Grade Line Pipe, Cost Benefit Versus Reliability. *Pipeline Technology Conference*, (Pipelines International).

[14] Chao TW (2004) Gaseous Detonation-Driven Fracture of Tubes, Ph.D. (California Institute of Technology, Pasadena, CA, U.S.A.). Available at

[15] Chen C, Kolednik O, Scheider I, Siegmund T, Tatschl A, Fischer F (2003) On the determination of the cohesive zone parameters for the modeling of micro-ductile crack growth in thick specimens. *International journal of fracture* 120(3):517-536.

[16] Chon S-H, Yoo, J-Y, Seo, D-H. (2009) Microstructure and Mechanical Properties of Heavy Gauge X70 Offshore Pipeline Steels. *Pipeline Technology Conference*, (Pipelines International).

[17] Cosham A, Jones, D. G., Eiber, R., Hopkins, P. (2009) Don't Drop the Drop Weight Tear Test. *Pipeline Technology Conference*, (Pipelines International).

[18] Cravero S, Bravo, R. E., Ernst, H. A. (2009) Fracture Evaluation of Cracked Pipelines Subjected to Combined Loading. *Pipeline Technology Conference*, (Pipelines International).

[19] Dawicke DS, Newman, J. C. Jr., Bigelow, C. A. (1995) Three-Dimensional CTOA and Constraint Effects During Stable Tearing in a Thin-Sheet Material. (National Aeronautics and Space Administration, NASA Technical Memorandum 109183).

DRAFT

[20] Dawicke DS, Newman, J. C. Jr. (1998) *Residual Strength Predictions for Multiple Site Damage Cracking Using a Three-Dimensional Finite Element Analysis and a CTOA Criterion* (American Society for Testing and Materials).

[21] Demofonti G, Maresca A, Buzzichelli G (1988) Ductile fracture propagation and arrest in offshore pipelines. *Applied Mechanics Reviews* 41(2):85-95.

[22] Denys R, Hertelé, S., De Waele, W., Lefevre, A. (2009) Estimate of Y/T ratio and uniform elongation capacity of pipeline steels from yield strength. *Pipeline Technology 2009*.

[23] Dunbar A, Wang X, Tyson BW, Xu S (2012) Simulation of ductile crack propagation in pipeline steels using cohesive zone modeling. *ASME 2012 Pressure Vessels and Piping Conference*, (American Society of Mechanical Engineers), pp 917-926.

[24] Emery A, Love W, Kobayashi A (1976) Elastic crack propagation along a pressurized pipe. *Journal of Pressure Vessel Technology* 98(1):2-7.

[25] Erdelen-Peppler M, Hillenbrand, H-G., Knauf, G. (2009) Limits of Existing Crack Arrest Models. *Pipeline Technology Conference*, (Pipelines International).

[26] Fearnehough GD (1974) Fracture propagation control in gas pipelines: A survey of relevant studies. *International Journal of Pressure Vessels and Piping* 2(4):257-282. https://doi.org/http://dx.doi.org/10.1016/0308-0161(74)90007-6

[27] Fonzo A, Meleddu A, Demofonti G, Tavassi M, Rothwell B (2006) Ductile Fracture Control for High Strength Steel Pipelines. *2006 International Pipeline Conference*, (American Society of Mechanical Engineers), pp 349-358.

[28] Gadamchetty G, Pandey A, Gawture M (2016) On Practical Implementation of the Ramberg-Osgood Model for FE Simulation. *SAE International Journal of Materials and Manufacturing* 9(1):200-205. https://doi.org/10.4271/2015-01-9086

[29] Glover AG, Horsley DJ, Dorling DV (1998) Pipeline design and construction using higher strength steels. *1998 2nd International Pipeline Conference*, (American Society of Mechanical Engineers Digital Collection), pp 659-664.

[30] Gray JM, Siciliano, F. (2009) High Strength Microalloyed Linepipe: Half a Century of Evolution. *Pipeline Technology Conference*, (Pipelines International).

[31] Gurson AL (1977) Continuum theory of ductile rupture by void nucleation and growth: Part I—Yield criteria and flow rules for porous ductile media.

[32] Hara T, Shinohara, Y., Terada, Y., Asahi, H., Doi, N. (2009) Development of High-Deformable High-Strength Line Pipe Suitable for Strain-Based Design. *Pipeline Technology Conference*, (Pipelines International).

[33] Hara T , Fujishiro T (2010) Effect of Separation on Ductile Crack Propagation Behavior During Drop Weight Tear Test. *2010 8th International Pipeline Conference*, (American Society of Mechanical Engineers), pp 321-327.

[34] Hashemi S, Gay R, Howard I, Andrews R, Yates J (2013) Development of a laboratory test technique for direct estimate of crack tip opening angle. *ECF15, Stockolm 2004*.

[35] Hashemi SH (2008) Apportion of Charpy energy in API 5L grade X70 pipeline steel. *International Journal of Pressure Vessels and Piping* 85(12):879-884.

[36] Herterle S, Denys, R., Waele, W. D. (2009) Full Range Stress-Strain Relation Modeling of Pipeline Steels. *Pipeline Technology Conference*, (Pipelines International).

[37] Holmes B, Priest A, Walker E (1983) Prediction of linepipe fracture behaviour from laboratory tests. *International Journal of Pressure Vessels and Piping* 12(1):1-27.

[38] Horsley DJ (2003) Background to the use of CTOA for prediction of dynamic ductile fracture arrest in pipelines. *Engineering Fracture Mechanics* 70(3–4):547-552. https://doi.org/http://dx.doi.org/10.1016/S0013-7944(02)00136-4

DRAFT

[39] Huo CY, Yang, X. B., Zhuang, Z., Maitirouzi, J., Feng, Y. R., Zhuang, C. J. (2006) The FEM Simulation and Full-Scale Blast Tests for Crack Deceleration in Gase Pipeline. *Key Engineering Materials* 306-308:85-90.

[40] Ives K, Shoemaker A, McCartney R (1974) Pipe deformation during a running shear fracture in line pipe. *Journal of Engineering Materials and Technology* 96(4):309-317.

[41] Kanninen M, Hudak Jr S, Couque H, Dexter R, O'donoghue P (1990) Viscoplastic-dynamic crack propagation: Experimental and analysis research for crack arrest applications in engineering structures. *Non-Linear Fracture,* (Springer), pp 239-260.

[42] KAWAGUCHI Y, TSUKAMOTO M, SUMITOMO Y, TAKEUCHI I, YAMASHITA A, NARA Y (1982) Study on the Propagating Shear Fracture of Line Pipes by the Partial-gas Burst Test. *Transactions of the Iron and Steel Institute of Japan* 22(8):617-623.

[43] Lam P-H, Kim, Y., Chao, Y. J. (2005) Crack Tip Opening Displacement and Angle for a Growing Crack in Carbon Steel. *ASME Pressure Vessels and Piping Conference*, ed Engineers ASoM.

[44] Leis B , Brust F (1992) Hydrotest strategies for gas transmission pipelines based on ductile-flaw-growth considerations. (American Gas Association, Inc., New York, NY (United States); American Gas …).

[45] Leis BN, Zhu, X-K., Forte, T. P., Clark, E. B. (2005) Modeling running Fracture in Pipelines- Past, Present, and Plausible Future Directions. *11th International Conference on Fracture*, (Curran Associates).

[46] Leis BN, Zhu, X-K., Forte, T. P. (2009) New Approach to Assess Running Fracture Arrest in Pipelelines. *Pipeline Technology Conference*, (Pipelines International).

[47] Leis BN (2015) Arresting propagating shear in pipelines. *Steel in Translation* 45(1):1-17.

[48] Lgi S, Kawaguchi, S., Suzuki, N. (2009) Running Ductile Fracture Analysis for X80 Pipeline in JGA Burst Tests. *Pipeline Technology Conference*, (Pipelines International).

[49] Link RE, Joyce, J. A. Roe, C. (2009) Crack arrest testing of high strength structural steels for naval applications. *Engineering Fracture Mechanics* 76(3):402-418. https://doi.org/http://dx.doi.org/10.1016/j.engfracmech.2008.11.006

[50] Lloyd WR (2003) Microtopography for ductile fracture process characterization: Part 1: Theory and methodology. *Engineering Fracture Mechanics* 70(3–4):387-401. https://doi.org/http://dx.doi.org/10.1016/S0013-7944(02)00126-1

[51] Lloyd WR, McClintock, F. A. (2003) Microtopography for ductile fracture process characterization Part 2: application for CTOA analysis. *Engineering Fracture Mechanics* 70(3–4):403-415. https://doi.org/http://dx.doi.org/10.1016/S0013-7944(02)00127-3

[52] Makino H, Inoue, T., Endo, S., Kubo, T., Matsumoto, T. (2004) Simulation Method for Shear Fracture Propagation in Natural Gas Transmission Pipelines. *International Journal of Offshore and Polar Engineering* 14(1):60-68.

[53] Makino H, Takeuchi, I., Higuchi, R. (2009) Fracture Arrestability of High Pressure Gas Transmission Pipelines by High Strength Linepipes. *Pipeline Technology Conference*, (Pipelines International).

[54] Manahan MPS (2013) Constraint-modified Charpy-Sized Fracture toughness Soecimen for Line Pipe Testing. *AISTech*, (Association for Iron & Steel Technology).

[55] Mannucci G, Demofonti, G. (2009) Control of Ductile Fracture Propagation in X80 Gas Linepipe. *Pipeline Technology Conference*, (Pipelines International).

[56] Misawa K, Imai, Y., Aihara, S. (2009) Coupled Numerical Model of Gas-Decompression and Unstable Ductile Crack Propagation in High-Pressure Gas Pipelines. *Pipeline Technology Conference*, (Pipelines International).

[57] Murtagian GR, Johnson, D. H., Ernst, H. A. (2005) Dynamic crack propagation in steel line pipes. Part I: Experimental investigation. *Engineering Fracture Mechanics* 72(16):2519-2534. https://doi.org/http://dx.doi.org/10.1016/j.engfracmech.2005.03.003

DRAFT

[58] Murtagian GR, Ernst, H. A. (2005) Dynamic axial crack propagation in steel line pipes. Part II: Theoretical developments. *Engineering Fracture Mechanics* 72(16):2535-2548. https://doi.org/http://dx.doi.org/10.1016/j.engfracmech.2005.03.004

[59] O'Donoghue PE, Kanninen, M. F., Leung, C. P., Demofonti, G., Venzi, S. (1997) The development and validation of a dynamic fracture propagation model for gas transmission pipelines. *International Journal of Pressure Vessels and Piping* 70(1):11-25. https://doi.org/http://dx.doi.org/10.1016/S0308-0161(96)00012-9

[60] Oldfield W (1979) Fitting curves to toughness data. *Journal of testing and evaluation* 7(6):326-333.

[61] Papka SD, Stevens, J. H., Marcia, M. L., Faichild, D. P., Peterson, C. W. (2003) Full-Size Testing and Analysis of X120 Linepipe. *Thirteenth International Offshore and Polar Engineering Conference*, (The International Society of Offshore and Polar Engineers).

[62] Popelar C, Rosenfield A, Kanninen M (1977) Steady-state crack propagation in pressurized pipelines. *Journal of Pressure Vessel Technology* 99(1):112-121.

[63] Pyshmintsev IY, Lobanova, T. P., Arabey, A. B., Sozonov, P. M., Struin, A. O. (2009) Crack Arrestability and Mechanical Properties of I 420mm X80 Grade Pipes Designed for 11.8 MPa Operation Pressure. *Pipeline Technology Conference*, (Pipelines International).

[64] Pyshmintsev IY, Arabey, A. B., Gervasyev, A. M., Boryakova, A. N. (2009) Effects of Microstructure and Texture on Shear Fracture in X80 Linepipes Designed for 11.8 MPa Gas Pressure. *Pipeline Technology Conference*, (Pipelines International).

[65] Rivalin F, Pineau, A., Di Fant, M., Besson, J. (2000) Ductile tearing of pipeline-steel wide plates: I. Dynamic and quasi-static experiments. *Engineering Fracture Mechanics* 68(3):329-345. https://doi.org/http://dx.doi.org/10.1016/S0013-7944(00)00107-7

[66] Rivalin F, Besson, J., Pineau, A., Di Fant, M. (2000) Ductile tearing of pipeline-steel wide plates: II. Modeling of in-plane crack propagation. *Engineering Fracture Mechanics* 68(3):347-364. https://doi.org/http://dx.doi.org/10.1016/S0013-7944(00)00108-9

[67] Roos E, Seidenfuss M, Kraaemer D, Krolop S, Eisele U, Hindenlang U (1991) Application and evaluation of different numerical methods for determining crack resistance curves. *Nuclear engineering and design* 130(3):297-308.

[68] Rousselier G (1987) Ductile fracture models and their potential in local approach of fracture. *Nuclear engineering and design* 105(1):97-111.

[69] Rudland DL, Wang Y-Y, Wilkowski G, Horsley DJ (2004) Characterizing dynamic fracture toughness of linepipe steels using the pressed-notch drop-weight-tear test specimen. *Engineering fracture mechanics* 71(16-17):2533-2549.

[70] Scheider I , Brocks W (2003) Simulation of cup–cone fracture using the cohesive model. *Engineering Fracture Mechanics* 70(14):1943-1961.

[71] Schindler HJ (2010) Prediction of Rapid Ductile Crack Extension and Arrest by an Analytical Approach. *9th International Pipeline conference*, (American Society of Mechanical Engineers).

[72] Shinohara Y, Besson, J, Madi, Y. (2009) Pre-Strain Effect on Ductility of High Strength Line Pipe Steels. *Pipeline Technology Conference*, (Pipelines International).

[73] Shterenlikht A, Hashemi, S. H., Howard, I. C., Yates, J. R., Andrews, R. M. (2004) A specimen for studying the resistance to ductile crack propagation in pipes. *Engineering Fracture Mechanics* 71(13–14):1997-2013. https://doi.org/http://dx.doi.org/10.1016/j.engfracmech.2003.10.001

[74] Sugie E, Kaji H, Taira T, Ohashi M, Sumitomo Y (1984) Shear fracture arrestability of controlled rolled steel X70 line pipe by full-scale burst test. *Journal of energy resources technology* 106(1):55-62.

[75] Sumpter JDG (2007) Size effects in tearing instability: An analysis based on energy dissipation rate. *Engineering Fracture Mechanics* 74(15):2352-2374. https://doi.org/http://dx.doi.org/10.1016/j.engfracmech.2006.11.009

DRAFT

[76] Tagawa T, Lgi, S., Kawaguchi, S. (2009) Fractography of Pipeline Burst Tests. *Pipeline Technology Conference*, (Pipelines International).

[77] Tagawa T, Lgi, S., Kawaguchi, S. Ohata, M., Minami, F. (2012) Fractography of burst-tested linepipe. *International Journal of Pressure Vessels and Piping* 89(0):33-41. https://doi.org/http://dx.doi.org/10.1016/j.ijpvp.2011.09.009

[78] Takahashi N, Makino, H., Higuchi, R., Takeuchi, I. (2009) Toughness of High Strength Line Pipe for Fracture Arrest Assessment. *Pipeline Technology Conference*, (Pipelines International).

[79] Takeuchi I, Makino, H., Okaguchi, S., Takahashi, N., Yamamoto, A. (2006) Crack Arrestability of High-Pressure Gas Pipelines by X100 or X120. *23rd World Gas Conference*, (International Gas Union).

[80] Tanguy B, Luu, T. T., Perrin, G., Pineau, A., Besson, J. (2008) Plastic and damage behaviour of a high strength X100 pipeline steel: Experiments and modelling. *International Journal of Pressure Vessels and Piping* 85(5):322-335. https://doi.org/http://dx.doi.org/10.1016/j.ijpvp.2007.11.001

[81] Terada Y, Tamehiro, H., Yamashita, M., Ayukawa, N., Hara, T. (January 1997) Development of API X100 UOE Line Pipe. (Nippon Steel Technical Report No. 72).

[82] Tvergaard V (1981) Influence of voids on shear band instabilities under plane strain conditions. *International Journal of fracture* 17(4):389-407.

[83] Tvergaard V , Hutchinson JW (1992) The relation between crack growth resistance and fracture process parameters in elastic-plastic solids. *Journal of the Mechanics and Physics of Solids* 40(6):1377-1397.

[84] Wilkowski G, Shim, D. J., Brust, F. W., Rudland, D. L., Duan, D-M. (2009) Evaluation of Fracture Speed on Ductile Fracture Resistance. *Pipeline Technology Conference*, (Pipelines International).

[85] Xue L, Wierzbicki, T. (2009) Numerical simulation of fracture mode transition in ductile plates. *International Journal of Solids and Structures* 46(6):1423-1435. https://doi.org/http://dx.doi.org/10.1016/j.ijsolstr.2008.11.009

[86] Zhuang Z, O'Donoghue, P. E. (2000) The recent development of analysis methodology for rapid crack propagation and arrest in gas pipelines. *International Journal of Fracture* 101(3):269-290. https://doi.org/10.1023/a:1007614308834

DRAFT